UNIVERSITY OF OKLAHOMA

GRADUATE COLLEGE

APPLICATIONS OF THE GOES-R GEOSTATIONARY LIGHTNING MAPPER FOR SEVERE AND LOCAL STORMS.

A DISSERTATION

SUBMITTED TO THE GRADUATE FACULTY

in partial fulfillment of the requirements for the

degree of

Doctor of Philosophy

By

KEVIN CHARLES THIEL
Norman, Oklahoma
2025

APPLICATIONS OF THE GOES-R GEOSTATIONARY LIGHTNING MAPPER
FOR SEVERE AND LOCAL STORMS.

A DISSERTATION APPROVED FOR THE
SCHOOL OF METEOROLOGY

BY THE COMMITTEE CONSISTING OF

Dr. Cameron Homeyer (Chair)

Dr. Kristin Calhoun

Dr. Feng Xu

Dr. Michael Biggerstaff

Dr. Xin Feng

Acknowledgments

I was told pursuing a PhD can feel like a lonely endeavor, but having a supportive community helps. This was proven many times over with the blessing of so many people who made invaluable academic, professional, and personal contributions to help get me to this point. My name may be the one on this dissertation, but it was not done alone. To my advisor Dr. Kristin Calhoun. I cannot thank you enough for your support and challenging me to grow into the scientist I always wanted to become. Every academic success I have in the future will be shaped in some way because of the lessons you taught me. I'd also like to thank my committee chair Dr. Cameron Homeyer and committee members Dr. Feng Xu, Dr. Michael Biggerstaff, and Dr. Selena Feng for supporting my progress to make this dream a reality.

The Storm Prediction Center became an unexpected but invaluable ally along the way, and I am indebted to Dr. Patrick Marsh, Dr. Burkely Gallo, Dr. Israel Jirak, Dr. David Harrison, and Dr. David Jahn within SPC and CIWRO for supporting my growth at each step. Accepting a job one year into a PhD felt like a huge gamble at the time, but in hindsight it was exactly what I needed. I'm excited to continue building my career with the people who helped launch it, and supporting the high-impact mission of CIWRO and SPC. I've been fortunate to collaborate with such incredibly kind and talented people as part of this dissertation, and I'd like to thank Dr. Anthony Reinhart, Dr. Michael Stock, Dr. Sarah Stough, Dr. Jacquelyn Ringhausen, and Dr. Vanna Chmielewski for all their scientific contributions to this work. Your willingness to collaborate, ask the questions that didn't have easy answers, and solve problems head on every day set an example that I hope to emulate.

To my fiancée Madeline. Your unwavering support on this voyage has been an anchor of grace on the hardest of days, and the sail that pushed me faster upon each victory. Thank you for always believing in me, even when I struggled to believe in myself. I'm eager to return this love and grace to you as you continue your own PhD voyage and beyond. To the many friends I made in the School of Meteorology. Thank you for always making me feel like I belonged here. Whether it's camping, hiking, Flapjack Fridays, bible study, climbing, running, or volleyball, you all have been the definition of community and I wish you all the best. To my parents and family. Thank you for encouraging me to pursue my dream even when it led me away from home to places like Athens, Ohio; Miami, Florida; or Norman, Oklahoma. I wouldn't be half the person I am today without you all.

This dissertation was prepared by Kevin Thiel with funding provided by NOAA/ Office of Oceanic and Atmospheric Research under NOAA-University of Oklahoma Cooperative Agreement #NA21OAR4320204, U.S. Department of Commerce. The statements, findings, conclusions, and recommendations are those of the author and do not necessarily reflect the views of NOAA or the U.S. Department of Commerce.

Table of Contents

List Of Tables

List Of Figures

Abstract

The recently deployed GOES-R series Geostationary Lightning Mapper (GLM) provides forecasters with a new, rapidly-updating lightning data source to diagnose, forecast, and monitor atmospheric convection. Illuminated pixels (events) from the GLM in each 2 ms frame are joined into groups, and these groups are then clustered spatially and temporally into flashes. Lightning observations from the GOES-East and GOES-West GLMs cover a majority of the western hemisphere, with a considerable region of sensor overlap across the United States. Coincident lightning observations from both GLM sensors have revealed variations in flash detection efficiency and their observed characteristics within the region of sensor overlap. Additional studies leveraging dual-GLM observations of individual lightning flashes, combined with information from available ground-based lightning location systems, are needed to further validate and apply these data within the operational and severe storms research communities.

Gridded GLM products have been developed to improve operational forecast applications, with variables including Flash Extent Density (FED), Minimum Flash Area (MFA), and Total Optical Energy (TOE). While these gridded products have been demonstrated and are now used by the U.S. National Weather Service, there is a continual need to integrate these products with other datasets available to forecasters such as radar, satellite imagery, and ground-based lightning networks. Data from the Advanced Baseline Imager (ABI), Multi-Radar Multi-Sensor (MRMS) system, and one ground-based lightning network were compared against gridded GLM imagery from GOES-East and GOES-West in case studies of two supercell thunderstorms, along with a bulk study from 13 April through 31 May 2019, to provide further validation and applications of gridded GLM products from a data fusion perspective. Increasing FED and decreasing MFA corresponded with increasing thunderstorm intensity from the perspective of ABI infrared imagery and MRMS vertically integrated reflectivity products, and was apparent for more robust and severe convection. Flash areas were

also observed to maximize between clean-IR brightness temperatures of 210 to 230 K, and isothermal reflectivity at -10 °C of 20 to 30 dBZ. TOE observations from both GLMs provided additional context of local GLM flash rates in each case study, due to their differing perspectives of convective updrafts.

One of the most notable flashes within the life cycle of a thunderstorm is the appearance of its first lightning flash (i.e. 'first flash'), which can indicate that deep, moist convection with a substantial updraft has initiated. Additionally, the first lightning flash can be the most hazardous to the public due to the limited time to take protective action. GOES-East/-West GLM first flashes were identified and investigated over the continental United States in 2022 for comparison with ground-based lightning location systems, radar data, and satellite imagery. First, individual first flashes from the GLM were manually identified and studied from multiple lightning location systems. Over three-thousand candidate first flashes from seven cases of semi-discrete convection were then manually analyzed to select an objective identification criteria for first flashes. Over 170-thousand first flashes from both GLMs were then collected across the CONUS for all of 2022, and studied by region to provide insight into the factors that influence thunderstorm development and storm electrification. First flashes most frequently coincided with periods of peak convective instability daily and seasonally, and occurred in regions with -10°C isothermal reflectivity values between 35 and 45 dBZ, and ABI clean-IR brightness temperatures between 220 and 240 K. When matched with lightning flashes from a ground based lightning network and verified using a machine learning model, most first flashes were found to be intra-cloud flashes with exception to the southwestern United States.

Machine learning methods have become more widely adopted when diagnosing lightning activity and thunderstorm intensity, with operational and research applications. Based on coinciding satellite and radar observations from the two previously described studies, a two-tired machine learning problem was posed to identify (TRF1) and then classify convection (TRF2) using GLM observations as its truth. Two random forests were trained on four radar and satellite variables from seven cases of convection. Between the satellite and radar variables, isothermal reflectivity at -10°C demonstrated the greatest importance for both models. When identifying convection clean-IR brightness temperatures less than 220 K and -10°C reflectivity greater than 23 dBZ were frequently associated with lightning activity, even at low probabilistic thresholds from the first tier random forest model. When identifying convection capable of producing robust flash rates, the second tier random forest model demonstrated that -10°C reflectivity greater than 30 dBZ were frequently associated with more intense convection. Lastly, a case study from 14 May 2022 demonstrated the capability of both tiers of the model to provide diagnostic information for thunderstorm activity and intensity.

Chapter 1

Introduction

Lightning data can provide a wealth of information for the operational and severe storms research communities related to thunderstorm microphysics, convective morphology, severity potential, and the hazard of lightning itself to the public. The formation of oppositely charged regions within convective clouds - which creates the necessary conditions for lightning flashes to initiate - is driven by the ambient thermodynamic, kinematic, and microphysical properties imparted on hydrometeors within an updraft.

Charge separation between hydrometeors within convective clouds frequently occurs in the mixed phase region between the -10 and -40 °C isotherms, as collisions between ice and graupel particles in the presence of supercooled liquid water impart opposing charges on the hydrometeors (Takahashi 1978; Emersic and Saunders 2010). Lightning flashes initiate between oppositely charged regions (MacGorman et al. 1981; Williams 1985), and the organization of the electrical potential controls the frequency and propagation of the flash (Bruning and MacGorman 2013). The presence of mixed-phase hydrometeors for thunderstorm electrification can be inferred from radar reflectivity at various altitudes (Hondl and Eilts 1994; Wolf 2006; Mosier et al. 2011) or dual-polarization radar variables (Woodard et al. 2012; Stolzenburg et al. 2015). Additionally, hydrometeor glaciation driven by convective updrafts create cooling cloud tops observed from visible, near-infrared, and infrared satellite imagery (Roberts and Rutledge 2003; Elsenheimer and Gravelle 2019).

When a convective updraft first develops, hydrometeors lofted deep into the mixed phase region and the resulting first lightning flash is one indicator for the initiation of deep convection (Stolzenburg et al. 2015; Manzato et al. 2022). As a thunderstorm intensifies, lightning information can provide insight into key processes related to its increasing severity potential. Growth of the updraft volume and increasing graupel mass coincide with rapid increases in lightning production, which can be a useful signal of impending hazards such as large hail, damaging winds, and tornadoes (Williams et al. 1999; Schultz et al. 2009, 2017; Sandmæl et al. 2019). Additionally, trends in local flash rates are inversely related to the areal extent of lightning flashes (Bruning and MacGorman 2013; Calhoun et al. 2014), and an increasing frequency of spatially smaller flashes can also signal the growing severity potential of a thunderstorm (Schultz et al. 2015; Thiel et al. 2020).

Features from radar and satellite imagery can also be used to identify intensifying thunderstorms. Intense convective updrafts are frequently depicted from satellite imagery as decreasing local minima in infrared brightness temperatures (Roberts and Rutledge 2003), increasing isothermal areas of anvil shields (Makowski et al. 2013), overshooting tops (Adler et al. 1983; Bedka et al. 2010), and above anvil cirrus plumes (Bedka et al. 2018). The lofting of larger hydrometeors above the freezing level by the updraft can also be observed from increasing radar reflectivity at key isothermal levels, and used to identify hail formation and precipitation loading as precursors to severe weather occurrence. Lastly, vertically integrated reflectivity products provide insight into the strength and severity potential of convective updrafts, along with their potential to produce lightning (Greene and Clark 1972; Witt et al. 1998; Carey and Rutledge 2000). These products are generated in three dimensional rapidly updating reflectivity fields for operational and severe storms research applications (Smith et al. 2016).

1.1 The GOES-R Geostationary Lightning Mapper

Remotely sensed observations of lightning from ground-based networks have previously been leveraged by both the forecasting and severe storms research communities (Rison et al. 1999; Cummins and Murphy 2009). Launch of the first Geostationary Operational Environmental Satellites (GOES)-R series Geostationary Lightning Mapper (GLM) (Goodman et al. 2013) in 2016 provided a new perspective of total lightning observations across the Continental United States (CONUS) from GOES-East and GOES-West at 75 °W and 137 °W respectively. The GLM was designed with an average flash detection efficiency (DE) over the entire field of view of 70% and a false alarm rate of 5%. Several data validation efforts have attempted to describe and quantify the relative quality of GLM data over the CONUS region (Murphy and Said 2020; Zhang and Cummins 2020; Bateman et al. 2021), along with providing caveats when applying these data (Calhoun et al. 2018; Rutledge et al. 2020; Peterson 2021). Overall the GLM exceeds the required 70% average DE during both the day and night (Bateman et al. 2021), with lower detection efficiencies within 2000 km of the edge of the field of view (Murphy and Said 2020).

Gridded GLM imagery have been developed for research and operational applications, and take advantage of the spatial footprint of each lightning flash observed from the GLM (Bruning 2019; Bruning et al. 2019). These products were evaluated in NOAA's Hazardous Weather Testbed (HWT) from 2018 to 2022, and provided insights into the operational value of products related to flash density, area, and optical energy (Calhoun 2019; Thiel and Calhoun 2021; Thiel 2022). Additional machine-learning based products, which leverage GLM gridded and flash level data as an input variable or established truth data, have also been developed within the past five years (Cintineo et al. 2020b; Hilburn et al. 2021; Ringhausen et al. 2021; Cintineo et al. 2022) and demonstrated within the HWT (Thiel 2024).

1.2 Research Questions Addressed

The validation studies and demonstrations of the GLM previously described show the potential of the GLM as a research and operational tool for lightning observational studies, public safety, and studying deep convection. Further validation and integration of GLM data – as gridded imagery and at the individual flash level – with respect to other observational sources such as satellite imagery, radar data, and ground-based lightning location systems (LLSs) are necessary to expand the operational and scientific applications of these data. This dissertation aims to expand the research and operational applications of the GOES-R GLM with respect to satellite imagery, radar data, and other ground-based lightning networks for severe and local storms. First, gridded GLM imagery will be evaluated in two case studies of supercells and a larger seven-week study across the central and eastern United States with respect to deep convection and reports of severe weather occurrence. Next, developing convection will be studied from the perspective of a thunderstorm's first GLM-detected lightning flash across the CONUS. Lastly, the information from these studies will be used to explore their applications in identifying and classifying convection through machine learning techniques. Each study will be leveraged to answer the following research questions.

1.2.1 How can gridded imagery from the GLM be applied to severe and local storms?

In 2023 gridded GLM imagery became operational for the U.S. National Weather Service (NWS) after several years of development and demonstration in NOAA's Hazardous Weather Testbed (Bruning et al. 2019; Calhoun 2019; Thiel and Calhoun 2021; Thiel 2022). By using the spatial footprint of lightning flashes observed by the GLM, lightning information such as local flash density, area, and optical energy accumulation from thunderstorms can be used in short-term convective forecasting (Rudlosky et al. 2020), also referred to as 'nowcasting'. Much of the data collected from these testbeds were qualitative and sourced directly from NWS forecasters within a simulated operational environment. While qualitative feedback is valuable in the research-to-operations process, additional quantitative verification of observed GLM characteristics are needed to complete the iterative cycle between research and operations. The following subquestions will contribute answers to this broad question posed.

1.2.1.1 How can GLM gridded imagery be leveraged with existing satellite imagery and radar datasets to support convective forecasting?

Previous work from Thiel et al. (2020) demonstrated how GLM gridded imagery differs when sampled near reports of severe weather, however this study only considered satellite imagery as its reference. When these data were applied in the HWT's simulated operations, participants recommended that they be combined with ground-based lightning networks, satellite imagery, and radar observations to improve confidence in nowcasting applications such as situational awareness and warning decisions (Calhoun 2019; Thiel and Calhoun 2021). In this dissertation, radar data, satellite imagery, and information from ground-based lightning networks will be included to expand upon the initial seven-week study by Thiel et al. (2020). Additionally, case studies of supercell thunderstorms will be leveraged to evaluate the diagnostic performance of GLM imagery with respect to thunderstorm morphology and severe weather occurrence.

1.2.1.2 Can GLM gridded imagery from the GOES-East and GOES-West satellites provide additional insight for diagnosing convection?

With two GLMs in geostationary orbit, there is a large region of sensor overlap from approximately 80 °W to 130 °W. This provides the opportunity for GLM-to-GLM comparisons of the same thunderstorms. When comparing GLM data in these overlap regions, Rudlosky and Virts (2021) found spatial trends in relative DE and flash characteristics between the GOES-16 and GOES-17 GLMs. The GOES-16 GLM (hereafter GLM16) observes more flashes that are on average larger and less luminous when compared to the GOES-17 GLM (hereafter GLM17) east of 103 °W, and vice versa west of 103 °W. Further comparisons between the GOES-East and GOES-West GLMs may provide additional insights into the variations of GLM data characteristics, their quality, and their operational forecast applications, especially when combined with radar and satellite observations.

1.2.1.3 How does the optical energy from lightning flashes observed from the GLM vary relative to the intensity and severity of convection?

Three gridded products were made operational by the NWS, related to the local extent-density of flashes, their areas, and the accumulation of optical energy. Feedback regarding the extent-density and area-based products within the HWT were frequently well received in terms of confidence and utility (Thiel and Calhoun 2021). These align with the expectation that local flash rates will increase as local flash area decreases in intensifying updrafts (Bruning and MacGorman 2013; Calhoun et al. 2014; Thiel et al.

2020). When presented with the optical energy product however, forecasters felt less confident in its utility and applications for severe convective nowcasting (Thiel 2022). It is hypothesized that nonlinear aspects in the optical emission of lightning flashes, such as variations in cloud optical properties (Thomson and Krider 1982; Light et al. 2001; Brunner and Bitzer 2020) or the geometric emission path of light relative to the GLM sensor (Peterson et al. 2020), make the interpretation of severe and local storms from the perspective of lightning optical emissions more difficult. For these reasons, the GLM flash optical energy product will be included in the expanded study from Thiel et al. (2020). It is expected that the combination of GLM gridded imagery from the GOES-East and GOES-West positions will also provide the opportunity to assess the relative propagation paths and accumulated optical energy signatures from individual thunderstorms.

1.2.2 How can the GOES-R GLM be used to study developing convection?

Radar data and satellite imagery have been frequently leveraged to study developing convection regionally in the Continental United States (Banta and Schaaf 1987; Reif and Bluestein 2017; Shield and Houston 2024), however the spatial and temporal limitations of these observing platforms also limit their ability to uniformly study convection across the Continental United States. One distinct marker for deep convection in the developing stage is its first lightning flash, which signals the presence of a deep updraft, sufficient glaciation, and its ability to loft hydrometeors into the mixed phase region for ample charge separation (Emersic and Saunders 2010; Stolzenburg et al. 2015; Elsenheimer and Gravelle 2019). Lightning information has been leveraged objectively to study the development of deep convection in the Alpine region of Europe

(Manzato et al. 2022), and the large spatial domains covered by the GLM provide the opportunity to replicate this study across the CONUS. This study will attempt to study the first lightning flash produced by a thunderstorm - hereafter known as a first flash - from the perspective of the GLM. Subsequent questions below will contribute to an objective and manual analysis of these flashes, along with their scientific and operational applications.

1.2.2.1 What are the physical characteristics of first flashes observed by the GLM? How does this reflect the nature of the developing convection?

Flash characteristics from the GOES-East and GOES-West GLMs, such as duration, area, and optical energy, were quantified across their respective field of views by Rudlosky and Virts (2021). Variations in GLM flash characteristics were uncovered in continental and maritime convection, along with regional topography and meteorological influences. Locally, the propagation of a lightning flash is limited by the regions of charged hydrometeors and the available electrical potential (Bruning and MacGorman 2013). As an updraft intensifies, the rate of charge separation increases and charged hydrometeors are organized into smaller regions, resulting in frequent flashes but shorter in their extent (Calhoun et al. 2013; Schultz et al. 2015). By studying the first lightning flash from the GLM, it is expected that variations in flash area and duration will demonstrate variations in the strength of developing convection and their ability to organize regions of opposing charge. Additionally, the ability for a first lightning flash to transfer charge solely within a convective cloud, resulting in intra-cloud (IC) or cloud-to-ground (CG) lightning flashes, can be leveraged to diagnose the structure of charged hydrometeor regions within a convective cloud (Boccippio et al. 2001; Fuchs et al. 2015). First flashes will also be classified as IC or CG by matching flashes against a ground-based lightning network and a machine-learning based approach. It is expected that regions of the CONUS more likely to observe CG or IC flashes may also be more likely to observe first flashes of the same classification. This may have impacts on the structure of developing convection, along with operational utility to quantify their potential as a public hazard.

1.2.2.2 Can first flashes observed by the GLM be identified objectively?

Manzato et al. (2022) objectively identified first flashes in the Alpine region of Europe with cloud-to-ground lightning data. The definition used by Manzato et al. (2022) was at least two, and no more than thirty, cloud-to-ground lightning flashes in a 10.1 by 10.7 km area with no other flashes in a 50 km radius, and lightning activity remains for at least 90 minutes. The GLM detects both CG and IC lightning flashes, and from the GOES-East and GOES-West perspectives cover the Continental United States with a detection efficiency exceeding 50% (Bateman et al. 2021). If first flashes can be identified objectively, then they can be collected over large spatial and temporal domains to create a more complete picture of initiating convection and its corresponding signals from radar and satellite data. To create objective GLM-based criteria, over three-thousand candidate first flashes will be manually classified with respect to their association with developing convection. This baseline dataset will be compared with other thresholds to select an optimal criteria for the purposes of this study.

1.2.2.3 What signals from satellite and radar imagery accompany GLM first flashes?

Rapid cloud-top cooling can be observed from multiple spectral bands in geostationary imagery, driven by an updraft lofting liquid hydrometeors above the freezing level where ice nucleation and robust glaciation occur (Elsenheimer and Gravelle 2019). These signals from visible, near-infrared, and longwave infrared bands have been leveraged to anticipate the development of convection and subsequent onset of lightning activity in a thunderstorm (Elsenheimer and Gravelle 2019; Cintineo et al. 2022). Similarly hydrometeors lofted into the mixed phase region of an updraft - a sign of non-inductive charge imparted on graupel and ice particles - can be observed by radar. Reflectivity thresholds at or above the -10 °C isotherm (Hondl and Eilts 1994; Gremillion and Orville 1999; Wolf 2006), along with vertically integrated reflectivity values weighted to represent the amount of ice present (Carey and Rutledge 2000; Mosier et al. 2011), have been studied for their ability to also predict the onset of lightning activity. Geostationary satellite imagery at higher spatial and temporal resolutions have recently been made available from the GOES-R Advanced Baseline Imager (ABI) (Schmit et al. 2017). Meanwhile integrated, three dimensional multi-radar datasets have been developed to study convection (Smith et al. 2016; Murphy et al. 2023). By collecting the associated satellite and radar signals associated with first flashes, it is expected that previously-studied thresholds and signals can be validated across the Continental United States and better characterize the associated signals of first flashes.

1.2.3 Using results from Chapters 2 and 3, how can machine learning methods be leveraged to identify areas with lightning potential and classify convection?

After studying GLM flash characteristics with respect to severe and developing convection in Chapters 2 and 3, along with their correspondence with satellite imagery and radar data, one way to cross-validate these results is through supervised machine learning techniques (Géron 2019). More recently, observation-based machine learning approaches have been leveraged to diagnose lightning activity and thunderstorm intensity (Cintineo et al. 2020b; Lagerquist et al. 2021; Cintineo et al. 2022; Ortland et al. 2023), which have an array of severe storms research and operational applications (Thiel 2024). By leveraging the same GLM flash observations, satellite imagery, and radar data as the previous two studies, it is expected that similar results may be observed when attempting to identify developing convection and classify convection based upon its lightning activity.

Chapter 2

Validation and Data Fusion Applications of GLM Gridded Imagery

2.1 Motivation

The launch of the GOES-R GLM in 2017, followed by gridded GLM imagery being made available starting in 2018 and operational in 2023, provides the opportunity to study convection across a majority of the western hemisphere. With GLMs available on the GOES-East and GOES-West perspective, the large region of sensor overlap and availability of radar and satellite observations provide the opportunity to validate these imagery and identify additional applications when interrogating severe and local storms. This study will examine convection from the perspective of the GOES-East and GOES-West GLMs, with respect to merged reflectivity and satellite imagery datasets, in an attempt to identify key applications and caveats when using these datasets for severe thunderstorm identification and monitoring. Intercomparisons between datasets were examined through two case studies of discrete supercells in Kansas (24 May 2019) and Alabama (25 March 2021), along with a bulk 7-week study over the central and eastern United States in April and May of 2019.

2.2 Data and Methods

2.2.1 Satellite Data

The GLM provides continuous lightning observations over most of the western hemisphere between the +/- 54° latitudes (Rudlosky et al. 2019). Gridded GLM data from GOES-16 and GOES-17, the operational instruments during the period of study, were generated using glmtools (Bruning 2019; Bruning et al. 2019) and include Flash Extent Density (FED), Minimum Flash Area (MFA), and Total Optical Energy (TOE). Increasing FED and decreasing MFA values have been identified in thunderstorms with increasing updraft strength and severity potential (Thiel et al. 2020), similar to the relationships identified in recent numerical and observational studies (Calhoun et al. 2013, 2014; Schultz et al. 2015). Gridded data were accumulated over a 5-minute interval, updating every minute, based upon repeated recommendations from the HWT to quickly diagnose convective trends (Calhoun 2018, 2019).

Infrared brightness temperatures from cloud-top were collected from the Advanced Baseline Imager (Schmit et al. 2017), a 16-band radiometer on GOES-16 and GOES-17 (hereafter ABI16 and ABI17). Radiance measurements across the CONUS scene, which updates every five minutes in Mode 6 (Super Flex), were used for the bulk study, and from the Mesoscale and Full Disk scenes from ABI16 and ABI17 respectively for the two case studies. Cloud-top infrared data are used in operational and scientific applications to interrogate convection initiation, updraft strength, and the potential to produce severe weather (Reynolds 1980; Roberts and Rutledge 2003; Thiel et al. 2020), along with GLM data quality (Peterson 2021). Imagery from the ABI16 10.3 μm 'Clean-IR' band (Schmit et al. 2012) were used to manually identify overshooting tops in the supercell case studies using signatures consistent with Adler et al. (1985) and Bedka et al. (2010), along with using the approximate tropopause level from adjacent rawinsonde observations. In the bulk study, IR data from ABI16 were collected at cloud-top by administering the ABI clear-sky mask (ACM) (Heidinger and Straka 2013) product on the IR data to remove the pixels classified as clear-sky. Lastly, data from from the ABI Cloud Top Height Algorithm (Heidinger 2013) were collected in the bulk study to improve data quality as described later.

2.2.2 Ground-Based Data

Select products from the Multi-Radar Multi-Sensor (MRMS) System (Smith et al. 2016) were recorded for their ability to infer thunderstorm morphology, electrification processes, and variations in optical depth through layered and vertically integrated reflectivity and velocity products. MRMS provides reflectivity data from multiple Weather Surveillance Radar - 1988 Doppler (WSR-88D) network on a 0.01° horizontal grid with 33 vertical levels, and new data are made available operationally every two minutes. Isothermal reflectivity at -10 °C and Vertically Integrated Ice (VII) (Mosier et al. 2011; Carey and Rutledge 2000) were selected for their ability to represent the amount of graupel within the convective updraft and therefore provide context to a thunderstorm's total lightning production (Schultz et al. 2015; Carey et al. 2019). Additionally changes in VII may be used to infer the local scattering environment within the mixed phase region of the convective cloud which, along with source height, has been shown in simulations to impact the amount of light emitted from cloud top (Brunner and Bitzer 2020). Data from the Maximum Expected Size of Hail (MESH) (Witt et al. 1998) product were also recorded to infer cloud optical depths of the convective updraft, which in case studies have inversely corresponded with GLM optical energy measurements in severe thunderstorms (Calhoun et al. 2018). Lastly, the MRMS 0-2 km Azimuthal Shear product (Lakshmanan et al. 2006; Mahalik et al. 2019) (hereafter AzShear) was collected for each supercell case study. Azimuthal shear has been used to diagnose low level mesocyclones and tornadoes (Cintineo et al. 2020a; Sandmæl et al. 2023) with values ranging from the 98th percentile to the maximum value within a storm. In this study, the 99th percentile and maximum values were sampled from each supercell.

Ground-based total lightning data (intra-cloud and cloud-to-ground flashes) from the Earth Networks Total Lightning Network (ENTLN) (Zhu et al. 2022) were compared against GLM storm-total flash rates. The ENTLN contains over 900 sensors across the CONUS (Zhu et al. 2017), with a reported DE of total lightning over the southern CONUS exceeding 70% (Rudlosky 2015) and exceeding 90% in areas with increased sensor density (Zhu et al. 2017). A 2021 processing upgrade to the network increased pulse detection across North America by 45%, with the largest observed improvements made over the oceans (Zhu et al. 2022).

Severe weather events from NOAA's Storm Data archive (Strassberg and Sowko 2021) were also included to provide verification of hazardous weather events associated with the ABI, GLM, and MRMS datasets. While reports of severe weather provide a number of caveats related to reporting biases, detection rates, and miscellaneous human factors (Kelly et al. 1985; Potvin et al. 2019; Trapp et al. 2006), their spatial and temporal references to severe weather occurrences were leveraged for this study with regards to severe hail ($\geq$ 1 in.), wind ($\geq$ 58 mph), and tornadoes.

2.2.3 Data Processing

Data were collected for two case studies along with a bulk data study which expands upon the dataset created by Thiel et al. (2020). The two case studies featured discrete supercell thunderstorms from 24 May 2019 (southeastern Kansas) and 25 March 2021 (central Alabama) to provide a variety of supercell types, associated environments, hazards, and satellite viewing angles. Discrete supercells were selected for their ability to produce severe and high-impact phenomena such as large hail, damaging winds, and tornadoes, along with producing a quasi-steady updraft that could be studied with respect to its lightning, radar, and satellite signatures. The approximate GLM16 and GLM17 viewing angles of the 24 May 2019 supercell (from zenith) were 50° and 60° respectively. In comparison, GLM16 and GLM17 viewing angles of the 25 March 2021 supercell (from zenith) were approximately 40° and 65° respectively. One minute data from both GLM instruments were directly compared for the case studies, with MRMS data recorded every two minutes. Storm-total flash rates from both GLMs and the ENTLN were also accumulated over five minutes and updated every one minute. Time series data were generated by manually tracking the supercell of interest and selecting the maximum GLM and MRMS values from the supercell.

ABI16, GLM16, and Storm Data information for the bulk study were collected using the same time period (13 April - 31 May 2019) and 20 km target grid based on the GOES-16 CONUS sector as Thiel et al. (2020). Additionally, ABI16 and GLM16 data were collected using the same KD-tree method to find the desired maximum or minimum value near each grid point. While Thiel et al. (2020) uses preliminary local storm reports from the National Weather Service, quality controlled events from Storm Data can combine multiple reports into one event with additional time and path information. Therefore, Storm Data events were linearly interpolated in space and time to improve their coverage in the bulk study. The number of marked samples when using the interpolated Storm Data events were nearly identical when compared against the preliminary local storm reports, which displayed the robust nature of a 15 km radius of influence and 10 minute temporal window used by Thiel et al. (2020). The GLM and ABI data filters cited in Thiel et al. (2020) were also used in the current study, as adjustments in the GLM ground processing to remove false flashes in certain regions of the CONUS scene had not been made yet. These filters removed all data with cloud top heights below 1 km as well as pixels that met all of the following conditions: 1) ABI cloud-top brightness temperatures greater than 270 K, 2) FED values greater than 10 flashes per 5 minutes, and 3) ABI cloud-top heights less than 4 km. The bulk dataset does keep flashes that have been artificially split in the GLM Lightning Cluster Filter Algorithm (Goodman et al. 2012), which impacts approximately 3% of all recorded GLM flashes (Peterson 2019). However, these effects are minimal when interpreting a storm's maximum FED and minimum MFA, or assessing the bulk distributions of FED and MFA.

MRMS data from the original 0.01° grid were resampled using the bulk dataset's 20 km target grid through a modified KD-tree method (Maneewongvatana and Mount 1999). All MRMS points from the most recent available time step and within a 15 km radius of influence were selected from each point in the 20 km target grid, with the maximum value from each MRMS variable then assigned to the grid point. The 15 km radius of influence was selected due to the decreasing resolution of the ABI CONUS scene from nadir, along with to mitigate horizontal displacement of satellite features due to parallax. A 10 km radius of influence would result in a substantial undersampling of values over a majority of the CONUS domain, while radius of influence of 15 km created more normally distributed sampling errors when testing the KD-tree method. Additionally, the median parallax corrected distance across the central and eastern CONUS from the bulk dataset was approximately 12 km. To further increase the quality of MRMS observations with respect to the current density of the WSR-88D network across the CONUS, only MRMS values located east of 105 °W were leveraged within the bulk dataset.

2.3 Supercell Thunderstorm Case Studies

2.3.1 24 May 2019

On 24 May 2019 a stationary, longwave, upper-level trough extended across the western United States, with downstream ridging over the Ohio River Valley. A stationary front was positioned between the ridge and trough axes over western Texas and central Kansas. Persistent moisture advection below the 850 hPa level from the Gulf of Mexico increased surface dew points to exceed 21 °C across northern Oklahoma and 18 °C in central and eastern Kansas at 1800 UTC. The 1800 UTC rawinsonde from Lamont, OK highlighted increased convective instability with a mixed layer convective available potential energy (ML-CAPE) value of 2005 J kg^{-1}, mixed layer convective inhibition (ML-CIN) of -10.1 J kg^{-1}, and precipitable water (PWAT) of 49.24 mm (1.94 in). Widespread instability, minimal inhibition, and 0-6 km bulk wind shear values exceeding 50 kts provided a suitable environment for widespread convection and the potential for supercell thunderstorms. Convection initiated along the stationary front in southern Kansas by 1600 UTC with thunderstorms becoming more widespread over the following six hours. A discrete thunderstorm initiated around 2000 UTC in Sumner County, Kansas, and continued to intensify into a supercell over the next 80 minutes until its first tornado report at 2119 UTC (Figures 2.1 and 2.2).

Genesis of the updraft was identified at 2000 UTC, near Sumner County, in a region with adjacent convection ongoing to its north and larger GLM flashes propagating between these two regions. Local minima in MFA values at 2001 UTC exceeded 1200 km^2 and 2000 km^2 from GLM16 and GLM17 respectively, with maximum FED values of 18 flashes per five minutes from both sensors while storm-total flash rates were exceptionally low. The maximum MRMS -10 °C reflectivity value was greater than 40

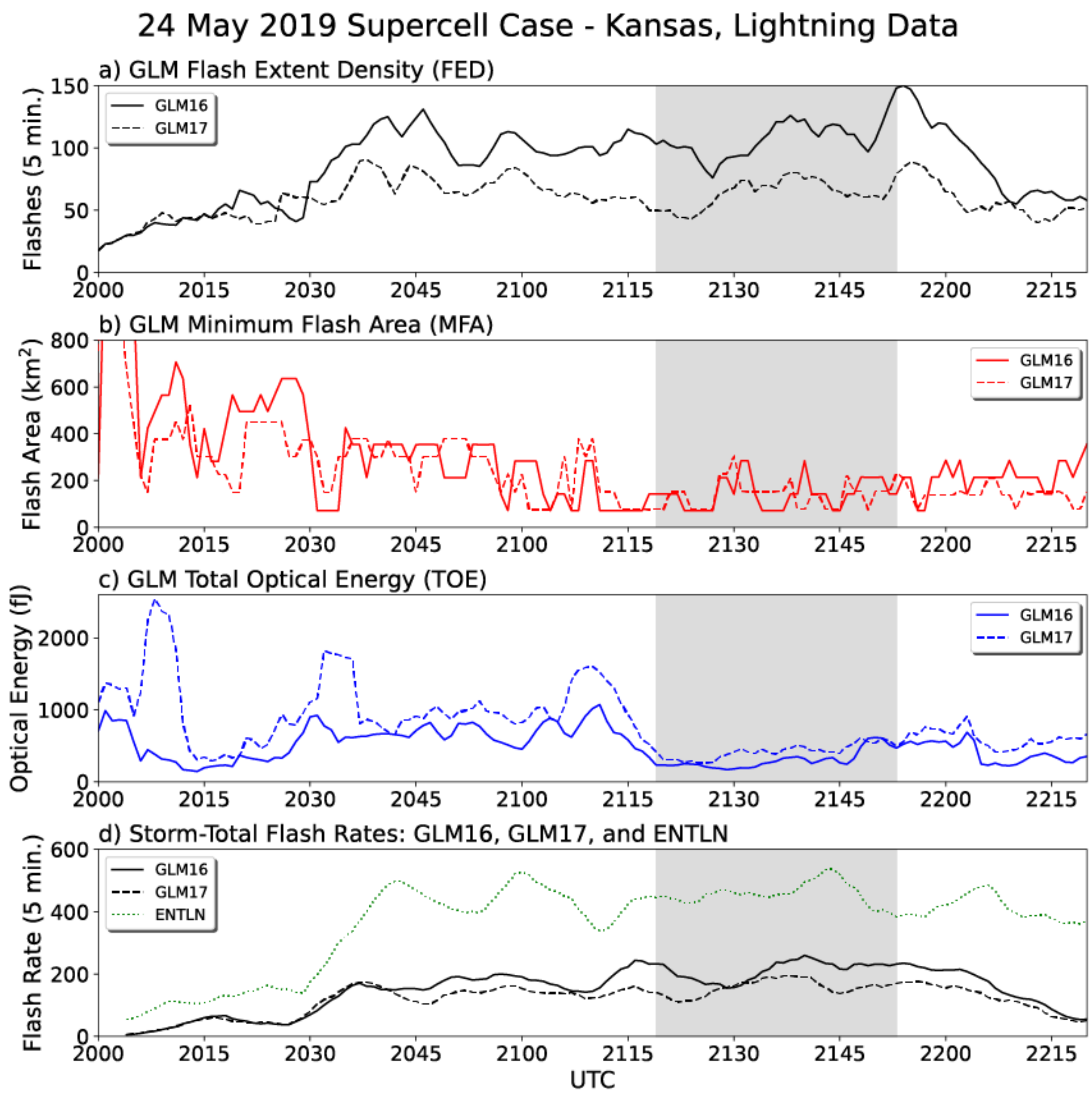

Figure 2.1: Time series plots from the 24 May 2019 Supercell Case in Kansas, including the gridded GOES-16 and -17 GLM (GLM16 and GLM17) variables, Flash Extent Density (a), Minimum Flash Area (b), and Total Optical Energy (c), and five-minute flash rates from the GLM16, GLM17, and ENTLN (d). The gray bar in each panel represents the time between the first and last storm report associated with the supercell.

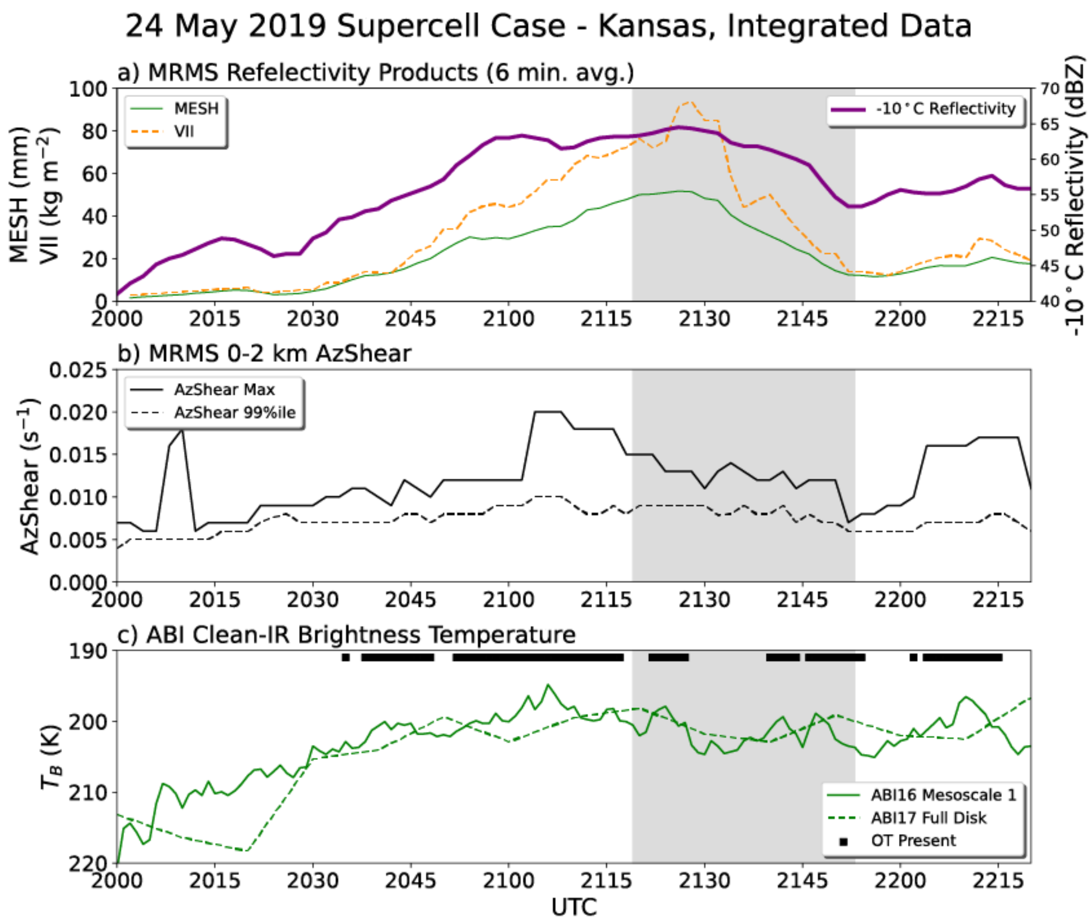

Figure 2.2: Same case as Figure 2.1, with MRMS reflectivity products (a), MRMS 0-2 km Azimuthal Shear (b), and ABI Clean-IR brightness temperatures from the available ABI16 and ABI17 scenes along with overshooting top (OT) identification (c).

dBZ at 2000 UTC and steadily increased over the proceeding 15 minutes to 49 dBZ, indicating a persistent updraft able to lift hydrometeors into the mixed phase region. During this time, maximum values from the vertically integrated variables, MESH and VII, remained below 5 mm and 6 kg m^{-2} respectively and FED increased to 47 flashes per 5 minutes for both GLMs. The local MFA minima decreased to 422 km^2 from GLM16 and 301 km^2 from GLM17 between 2001 and 2015 UTC. Maximum observed TOE values from GLM16 during this time decreased from 988 to 195 fJ, however GLM17-TOE observed a prominent spike at 2008 UTC of 2545 fJ before decreasing to 341 fJ at 2015 UTC.

At 2030 UTC GLM16-FED increased rapidly from 44 to 73 flashes within one minute, and was matched by a decrease in the MFA from 636 to 71 km^2. However, GLM17-FED remained constant during this period and corresponding MFA values decreased from 302 km^2 to 150 km^2. TOE values from both GLMs also increased but with different magnitudes. From GLM16, TOE values increased from 562 to 923 fJ between 2028 and 2031 UTC, while TOE from GLM17 increased from 794 to 1822 fJ between 2028 and 2032 UTC. The increased intensity across all three recorded GLM gridded variables around 2030 UTC coincided with the onset of rising values across all four MRMS variables, and preceded an increase in ENTLN flash rates at 2040 UTC. Around 2040 UTC, the storm of interest also deviated right of the mean storm motion and developed forward and rear flank downdrafts along with a consistent overshooting top signature, indicative of a maturing supercell thunderstorm.

During the next 20 minutes, from 2040 to 2100 UTC, the gridded GLM values remained steady while the MRMS variables steadily increased. MRMS MESH, VII, and -10 °C reflectivity during this 20 minute period increased from 12 to 29 mm, 13 to 40 kg m^{-2}, and 53 to 63 dBZ respectively, indicating an increasing number of large hydrometeors were lofted by the supercell's updraft to higher altitudes, including the mixed phase region. Maximum AzShear values suddenly increased between 2102 and 2014 UTC from 0.012 to 0.020 s^{-1}, the largest value of the entire case. Also during this period, GLM16 consistently recorded greater maximum FED values and total flash rates by approximately 25 flashes than GLM17, while maximum TOE values from GLM17 were approximately 200 fJ brighter than those from GLM16. Over the proceeding 15 minutes from 2100 UTC to 2115 UTC, maximum FED values remained elevated from both GLMs, while minimum MFA values decreased from 283 to 71 km^2 from GLM16, and from 226 to 76 km^2 from GLM17. At this time both local minima in MFA values were at their smallest possible areas from their respective sensor at their current viewing angles. Maximum TOE values from both sensors increased during this time, with GLM16-TOE increasing from 455 fJ at 2100 UTC to 1073 fJ at 2111 UTC, and GLM17-TOE increasing from 828 fJ to 1520 fJ.

The maximum values of MESH, VII and -10 °C reflectivity increased to exceed 40 mm, 60 kg m^{-2}, and 60 dBZ respectively between 2100 and 2120 UTC. At 2119 UTC a tornado was spotted south of Douglass, Kansas, and two instances of wind damage in Douglass were reported. FED and MFA values remained consistent during the onset of the severe weather, while TOE values from both GLMs fell below 500 fJ. Conversely, all three MRMS reflectivity products continued to increase, achieving their maximum values in the case between 2125 and 2130 UTC. Hail of 1 inch was reported at 2140 UTC west of Leon, Kansas, and another tornado report was received at 2153 UTC as maximum FED values from GLM16 and GLM17 reached 150 and 89 flashes shortly thereafter. After the second tornado report, total flash rates from both GLMs decreased as the supercell weakened and merged with nearby convection. Through the entire 140-minute lifespan of the storm, GLM16 observed 26% more flashes than GLM17. Conversely GLM17 observed 57% more optical energy than GLM16, resulting in GLM17 observing almost twice as much optical energy per flash when compared to GLM16.

2.3.2 25 March 2021

A mid-level, shortwave trough crossed from the southern Plains to the Great Lakes region on 25 March 2021 and coincided with a deepening mid-latitude cyclone across Arkansas and western Tennessee. At 1200 UTC, a 50 kt lower tropospheric jet at 850 hPa across Mississippi and Alabama advected lower tropospheric moisture from the Gulf of Mexico into the region. Surface dew points across central Mississippi and southern Alabama exceeded 18 °C behind a diffuse surface warm front, with a cold front positioned across western Texas and a broad stationary front extended from northern Louisiana through the Ohio River Valley region. Rawinsonde observations at 1500 UTC from the Jackson, MS upper air site, within the warm sector of the cyclone, continued to show a lower tropospheric jet up to 55 kts centered at 750 hPa. ML-CAPE, ML-CIN, and PWAT values of 2184 J kg^{-1}, -2.91 J kg^{-1}, and 35.75 mm (1.41 in.) respectively were observed, and 0-6 km bulk shear exceeded 60 knots with strong lower tropospheric shear. This created an environment conducive to semi-discrete supercells capable of producing tornadoes spanning from central Mississippi and Alabama to southern Tennessee. At 1500 UTC, a line of semi-discrete convection initiated along a pre-frontal band stretched from southeast Mississippi to northwest Alabama, moving northeast into a region with increasingly-backed surface winds. Convection along this line became more discrete over the proceeding hour, with one discrete thunderstorm of note east of Meridian, MS along the Alabama-Mississippi border at 1600 UTC. This thunderstorm continued to intensify and develop into a supercell thunderstorm by 1630

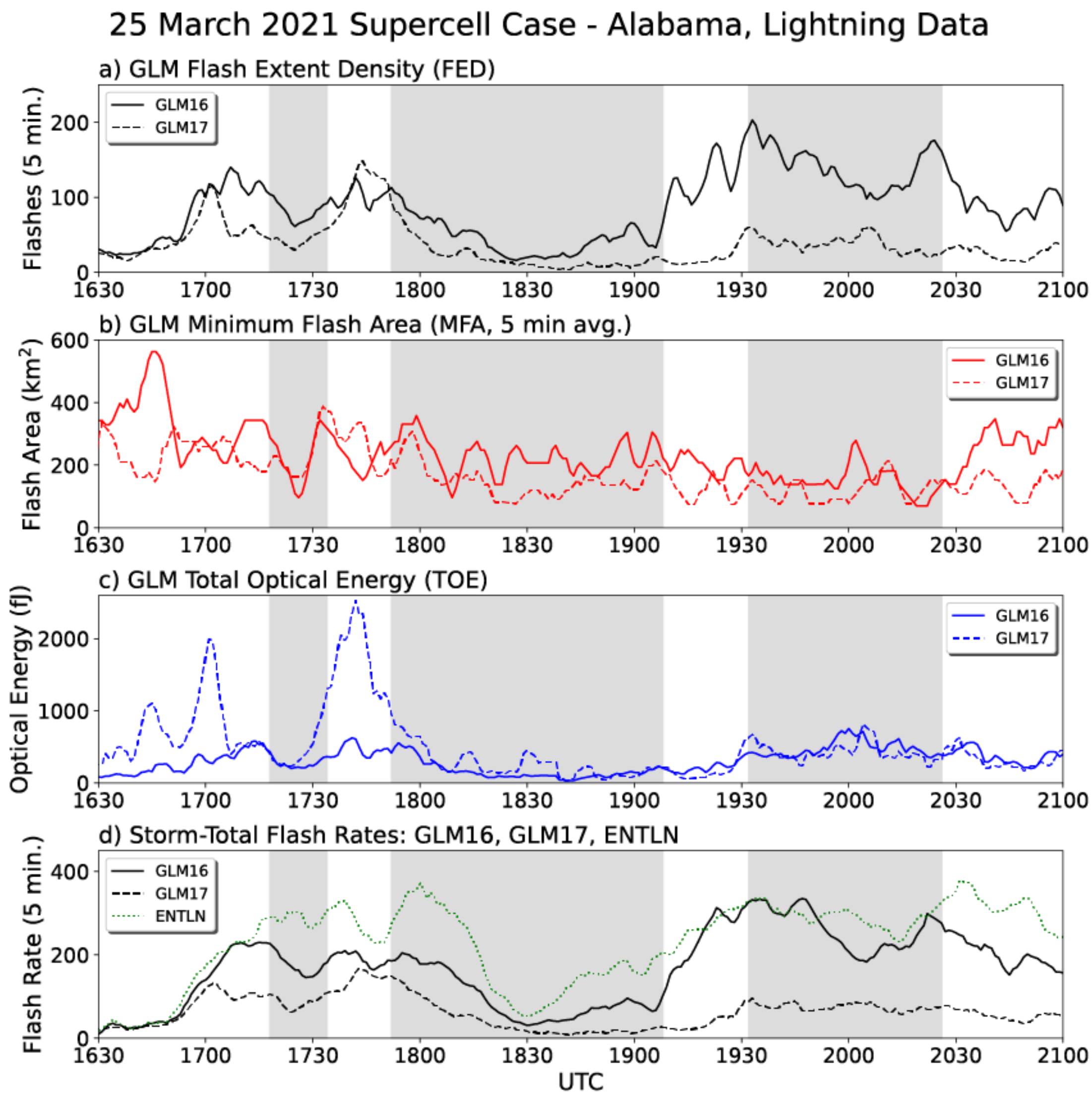

Figure 2.3: Time series plots from the 25 March 2021 Supercell Case in Alabama, including the gridded GOES-16 and -17 GLM (GLM16 and GLM17) variables, Flash Extent Density (a), Minimum Flash Area (b), and Total Optical Energy (c), and five-minute flash rates from the GLM16, GLM17, and ENTLN (d). The gray bars in each panel represent the estimated time periods that the supercell was producing a tornado (estimated from NWS surveys and MRMS data).

UTC in Sumter County, Alabama, which produced three tornadoes across Alabama over the proceeding four hours (Figures 2.3 and 2.4).

At 1630 UTC, the supercell had maximum FED values of 31 flashes from GLM16 and 26 flashes from GLM17. Isothermal reflectivity values at -10 °C exceeded 50 dBZ, with MESH and VII values at 7 mm and 18 kg m^{-2} respectively. Maximum TOE values from GLM17 (259 fJ) were initially three times greater than the maximum recorded by GLM16 (80 fJ). TOE from GLM17 increased between 1639 and 1645 UTC from 300 to 1110 fJ, while TOE from GLM16 only increased from 100 to 158 fJ. Fifteen minutes later at 1701 UTC, the maximum TOE from GLM17 rapidly increased again to 1997 fJ while the maximum TOE from GLM16 was only 284 fJ. The second increase in GLM17-TOE at 1653 UTC coincided with increased FED values, along with increased total flash counts from both GLMs and the ENTLN. A few minutes later around 1700 UTC MESH, VII, and maximum AzShear began to steadily increase with the emergence of an overshooting top signature, indicating a strengthening updraft capable of lofting larger hydrometeors into the mixed phase region with an organized low-level mesocyclone. Storm total flash rates from GLM16 continued to increase after 1700 UTC, while flash rates from GLM17 slowly decreased with a reduced optical signal to the sensor as observed in lower TOE values. Consequently, GLM16-FED remained over 100 flashes while GLM17-FED decreased to approximately 50 flashes by 1710 UTC.

At approximately 1718 UTC, the supercell produced its first tornado in northern Hale County as the maximum AzShear exceeded 0.03 s^{-1}, and achived it peak value for the case of 0.036 s^{-1} at 1722 UTC. While the tornado was on the ground for approximately 16 minutes, FED from GLM16 and GLM17 initially decreased until 1725 UTC. After 1725 UTC, GLM16-FED increased from 61 flashes to 126 flashes at 1742 UTC, while GLM17-FED increased from 30 to 131 flashes. During the same

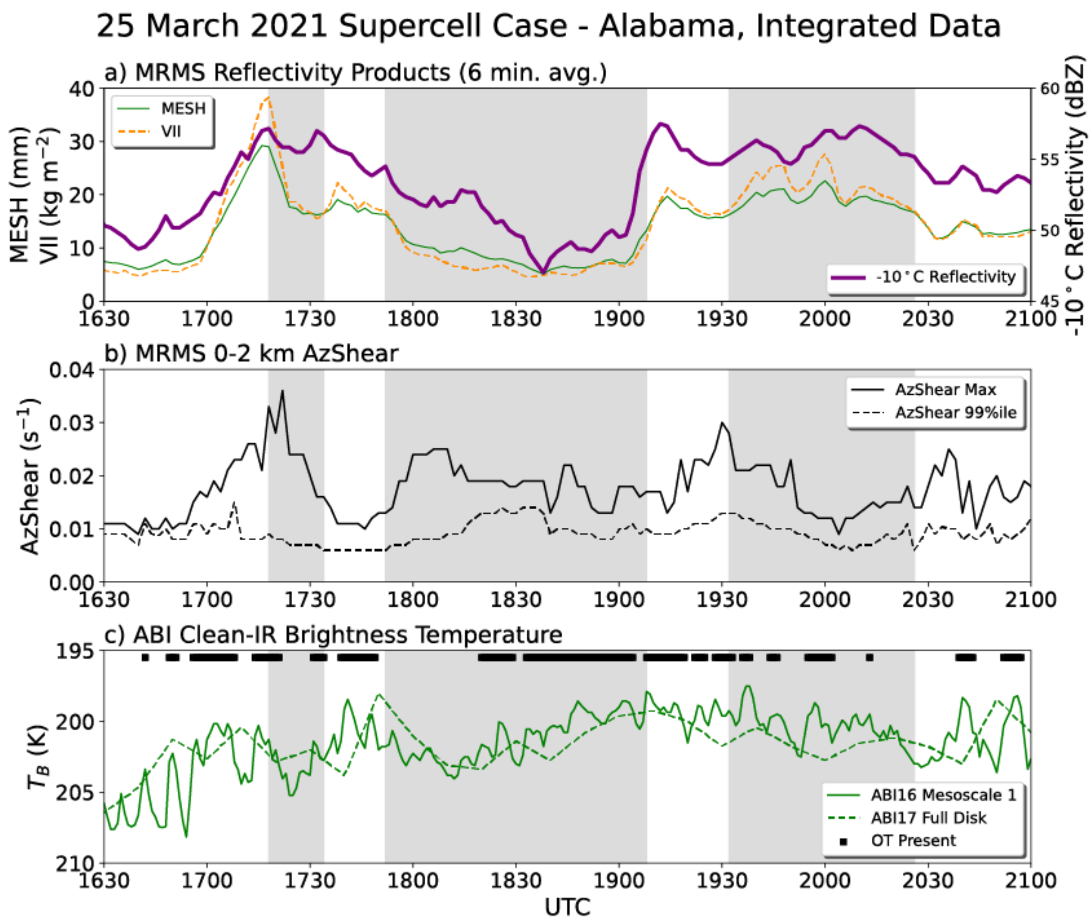

Figure 2.4: Same case as Figure 2.3, with MRMS reflectivity products (a), MRMS 0-2 km Azimuthal Shear (b), and ABI Clean-IR brightness temperatures from the available ABI16 and ABI17 scenes along with overshooting top (OT) identification (c).

time period, GLM17-TOE showed a third rapid increase from 253 to 2530 fJ, while maximum GLM16-TOE values increased from 215 to 608 fJ. The second tornado began at approximately 1752 UTC in northern Bibb County as the maximum AzShear value began to rise less the ten minutes prior. Maximum FED, maximum TOE, and total flash rates from GLM16 and GLM17 decreased from 1742 to 1830 UTC, and stayed at these lower values through 1900 UTC. The second tornado dissipated around 1908 UTC in extreme southern St. Clair County.

Around 1900 UTC, eight minutes before the second tornado ended, the parent updraft supporting the mesocyclone appeared to dissipate as a new updraft formed along its rear flank. Isothermal reflectivity at -10 °C rapidly increased from 48 to 59 dBZ by 1912 UTC, and in response MESH and VII also increased to 18 mm and 20 kg m^{-2} respectively by 1916 UTC. As more hydrometeors were lofted into the mixed phase region, GLM16, and ENTLN observed increasing flash rates while GLM17 recorded little change. Flash rates continued to increase across the three lightning location systems until genesis of the third tornado at 1932 UTC, just after the maximum AzShear value peaked at 0.03 s^{-1} again. Less than 10 minutes prior to tornadogenesis was the only instance where flash rates from GLM17 increased slightly in tandem with GLM16 and ENTLN. All three MRMS variables also remained elevated until the end of the third tornado at 2026 UTC. Through the 270-minute study of the supercell, GLM16 recorded 168% more flashes than GLM17. When accumulating the optical energy from all of flashes from each sensor, GLM16 recorded 27% more optical energy than GLM17, which means that GLM17 observed 112% more optical energy per flash than GLM16.

2.4 GLM, ABI, and MRMS Intercomparisons

Over the seven week period of study, 2.8 million instances of gridded GLM data were co-located with ABI and MRMS information across the central and eastern United States (Figure 2.5). Intercomparisons were largely limited to the continental United States due to spatial extent of the WSR-88D network used by the MRMS system. Samples were most frequently located in the Central Plains with a local maxima in southeast Kansas and broad regions exceeding 600 samples existed across the Central and Southern Great Plains.

Triple-sensor intercomparisons between ABI clean-IR cloud top brightness temperatures (hereafter referred to as brightness temperatures), gridded GLM variables, and the MRMS isothermal reflectivity at -10 °C in Figure 2.6 provided a unique perspective of convection across the three platforms with over 1.89 million samples. The 2-D histogram in Figure 2.6a, binned every 1 K and 1 dBZ, was used to examine the relationship between brightness temperature and isothermal reflectivity with respect to flashes recorded by the GLM. Flashes occurred at a variety of brightness temperatures and reflectivity values between 190 to 260 K and 10 to 65 dBZ respectively. GLM flashes most frequently occurred between brightness temperatures of 200 to 230 K and reflectivity values of 20 to 50 dBZ, with this region containing 50.2% of all samples in the bulk dataset. Median GLM values were sampled from the binned data in Figure 2.6a to assess trends in the gridded variables as a function of brightness temperature and isothermal reflectivity. Binned, median FED values in Figure 2.6b display a dependence on brightness temperature when isothermal reflectivity values were less than 30 dBZ. In this region, FED values increased from less than 2 flashes per 5 minutes at brightness temperatures greater than 240 K, to FED values greater than 10 and 20

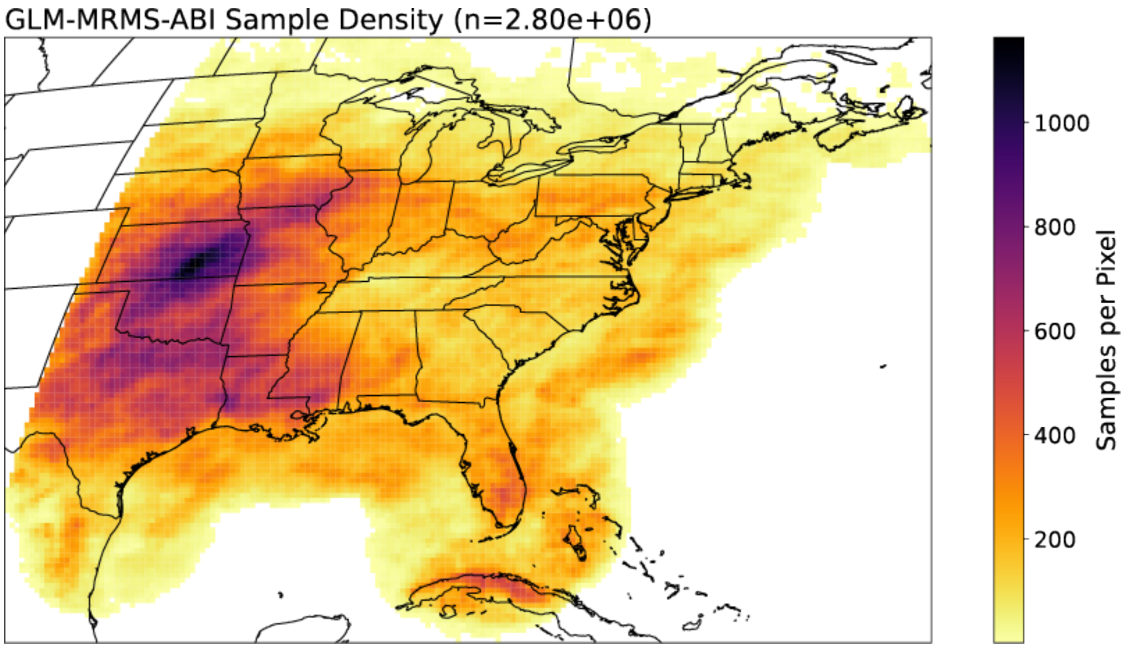

Figure 2.5: Location density values for all GLM-MRMS samples within the seven week period of study from 13 April to 31 May 2019.

flashes for brightness temperatures less than 205 and 200 K respectively. At isothermal reflectivity values greater than 30 dBZ, decreasing brightness temperatures and increasing isothermal reflectivity values correspond to greater FED values. Brightness temperatures below 210 K and isothermal reflectivity values above 50 dBZ correspond with FED values greater than 20 flashes per five minutes, indicating the presence of robust updrafts which generated more frequent local flash rates. FED values dramatically increase with brightness temperatures less than 200 K, exceeding 40 flashes across nearly all isothermal reflectivity values.

Variations in the median MFA values in each bin from Figure 2.6c also exhibit a strong dependence on brightness temperature when isothermal reflectivity values are below 30 dBZ, similar to Figure 2.6b. However there is an observed peak in MFA exceeding 500 km^2 between brightness temperatures from 210 to 230 K, and isothermal reflectivity values from 20 to 30 dBZ. Median MFA values then slowly decreases to

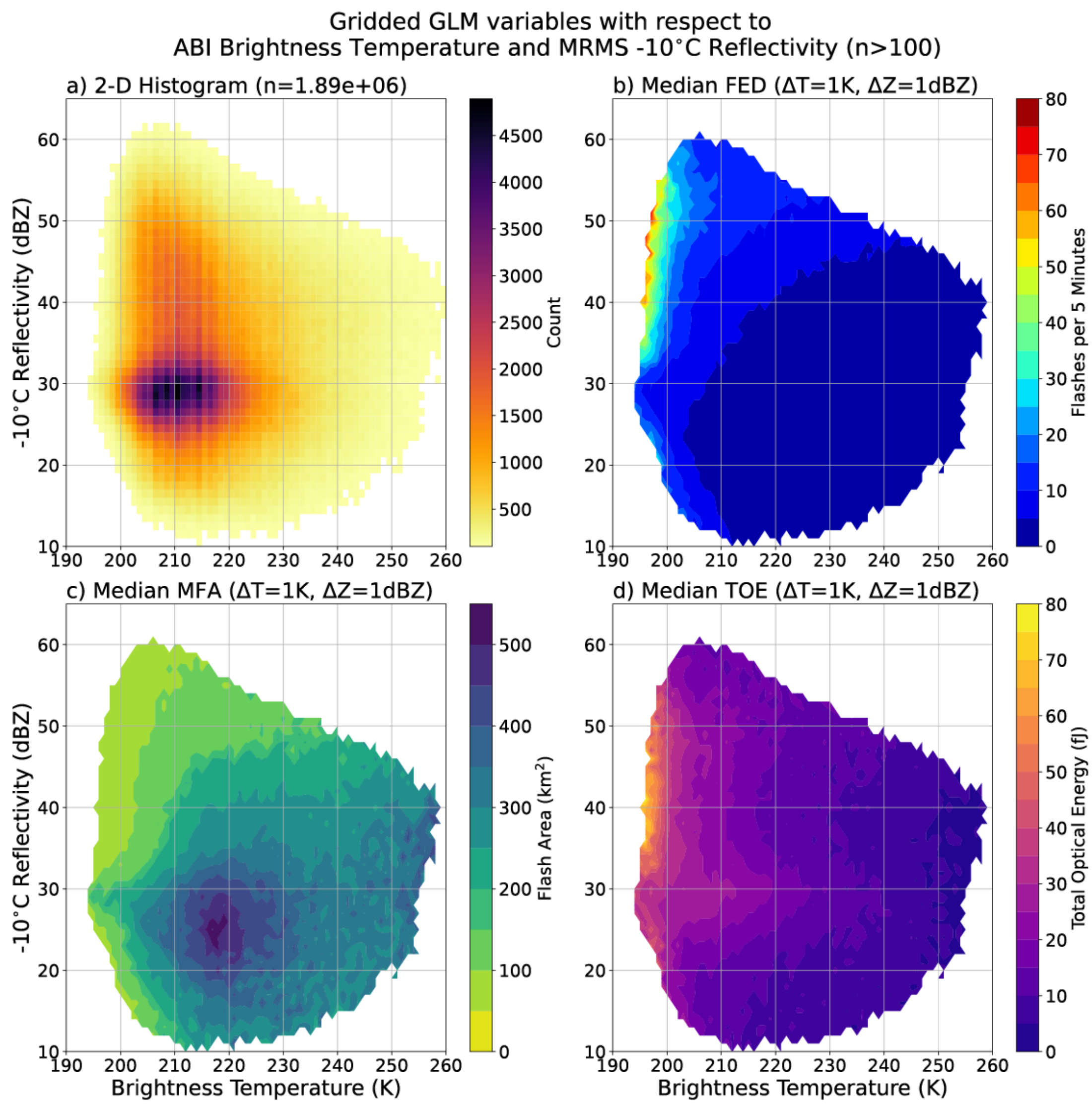

Figure 2.6: Gridded GLM variables compared to ABI Clean-IR brightness temperature and MRMS -10 °C reflectivity. Panel (a): The distribution of sampled GLM pixels, with the false flash filter applied, when binned by ABI brightness temperature every 1 K and MRMS -10 °C reflectivity every 1 dBZ. Panels (b), (c), and (d): Median FED, MFA, and TOE values sampled from the bins used in panel (a), respectively. (Median calculation requires minimum of 100 samples).

between 300 and 400 km^2 within this reflectivity range as the brightness temperature increases to 240 K. Conversely, decreasing brightness temperatures after this peak around 220 K correspond with MFA values decreasing to their smallest possible values below 100 km^2. For samples exceeding 30 dBZ, increasing isothermal reflectivity and decreasing brightness temperature corresponded with decreasing minimum flash areas. Median TOE values in Figure 2.6d did not exhibit similar relationships as Figures 2.6b and c. Across all isothermal reflectivity values, TOE exhibited a strong dependence on brightness temperature. A subtle maxima in TOE was observed between 25 and 35 dBZ coinciding with the peak in MFA in Figure 2.6c. The greatest median TOE values exceeding 60 fJ occur at brightness temperatures below 200 K and isothermal reflectivity values greater than 35 dBZ, which corresponded to the greater FED values in Figure 2.6b as more flashes contributed to the accumulated optical energy observed. Median TOE values exceeding 20 fJ typically occurred at brightness temperatures below 210 K, however between isothermal reflectivity values of 25 and 35 dBZ this contour increased to brightness temperatures of nearly 220 K at 30 dBZ.

While Figure 2.6 broadly defined how ABI clean-IR brightness temperature and MRMS isothermal reflectivity at -10 °C correspond to all gridded GLM variables, samples that coincided spatially and temporally with Storm Data events provided additional insight into these interrelationships with respect to severe convection. The 2-D histogram of all forty-four thousand points in Figure 2.7a reflects a shift in the proportion of samples to colder brightness temperatures and greater isothermal reflectivity values when compared to Figure 2.6a. Most samples are concentrated at brightness temperatures from 200 to 220 K and isothermal reflectivities from 25 to 60 dBZ. A peak in samples at a brightness temperature of 205 K and isothermal reflectivity of 50 dBZ are 5 K colder and 20 dBZ greater than the approximate peak in samples in Figure 2.6a. When coinciding with severe weather occurrence, median FED and MFA values depict a strong dependence on brightness temperature across all isothermal reflectivities (Figures 2.7b and c). MFA values below 100 km^2 at brightness temperatures below 210 K highlight an overall warmer threshold than similar MFA contours in Figure 2.6c. FED and MFA still show a prominent inverse relationship, especially for the peak in MFA values exceeding 300 km^2 from 25 to 30 dBZ and 215 to 220 K. Trends in median TOE values in Figure 2.7d were difficult to identify, with exception to a general dependence on brightness temperature similar to the median FED and MFA contours in Figures 2.7b and c. Overall, the greatest median TOE values (exceeding 30 fJ) occurred at brightness temperatures less than 205 K.

Distributions of the sampled MRMS MESH and VII values within the bulk dataset resemble exponential distributions. Thus, violin plots (Figures 2.8 and 2.9) provide distributions of gridded GLM values as functions of discrete MESH and VII bins. FED distributions within the MESH bins (Figure 2.8a) reveal an initial increase in FED as MESH increases, however for MESH values greater than 20 mm the distributions show little change. MESH values less than 10 mm peak in the distribution around 3 flashes per five minutes, with the median value of 8 flashes and 75th percentile value of 20 flashes. The 10-20 mm bin displays an increase in these values, with a peak in the distribution closer to 6 flashes, along with median and 75th percentile values of 14 and 38 flashes, respectively. All successive distributions contain peaks around 10 flashes per five minutes, with median values between 10 and 20 flashes, and 75th percentile values between 25 and 40 flashes. MFA distributions in Figure 2.8b show an inverse trend to the FED distributions, with flash areas decreasing initially with increasing MESH size. MFA values were consolidated around 150 km^2 (two GLM pixels) when MESH was less than 10 mm, and decrease to less than 100 km^2 (one GLM pixel) for all MESH bins greater than 10 mm. One ubiquitous aspect across all MESH bins is that

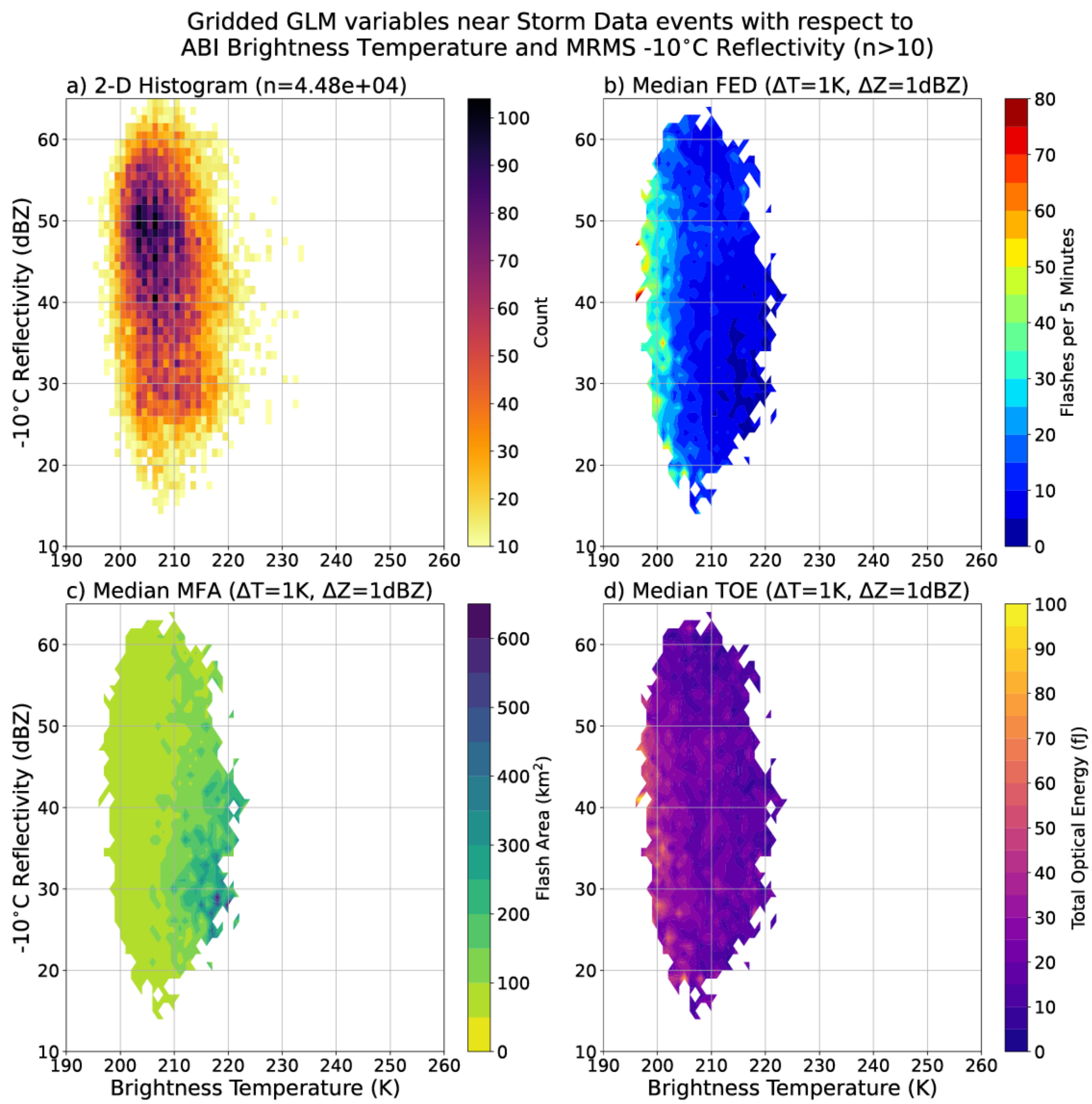

Figure 2.7: Gridded GLM variables compared to ABI Clean-IR brightness temperature and MRMS -10 °C reflectivity near local storm reports. Panel (a): The distribution of sampled GLM pixels, with the false flash filter applied, when binned by ABI brightness temperature every 1 K and MRMS -10 °C reflectivity every 1 dBZ. Panels (b), (c), and (d): Median FED, MFA, and TOE values sampled from the bins used in panel (a), respectively. (Median calculation requires minimum of 10 samples).

peaks in the frequency distributions occur at the size of a single GLM pixel, showing that convection capable of producing hail often coincided with the smallest possible GLM flashes. While FED and MFA showed distinct trends across the various MESH bins, TOE distributions in Figure 2.8c present no discernible signals in the median, 25th percentile, and 75th percentile values.

Gridded GLM and VII samples were binned every 5 kg m^{-2} for the first two bins, and every 10 kg m^{-2} afterward. These distributions with respect to VII in Figure 2.9a show an initial increase in the lowest VII bins similar to those observed in Figure 2.8a. Median and 75th percentile FED values increase across the lowest two VII bins (< 5 kg m^{-2} and 5-10 kg m^{-2}), from 4 to 11 kg m^{-2} and from 12 to 27 kg m^{-2}, respectively. Moving to successively greater VII bins, the distributions again show little variations with median values of approximately 12 kg m^{-2} and 75th percentile values between 30 and 40 kg m^{-2}. MFA and TOE distributions in Figures 2.9b and c also show similar results to those found in Figure 2.8b and c, respectively. Trends in MFA distributions are inversely proportional to those represented in the FED distributions, especially when inspecting the decreasing MFA values at the median and 75th percentile as the VII bins increased. TOE has little to no variations across the six discrete VII bins, with only slight differences between the 75th percentile TOE values.

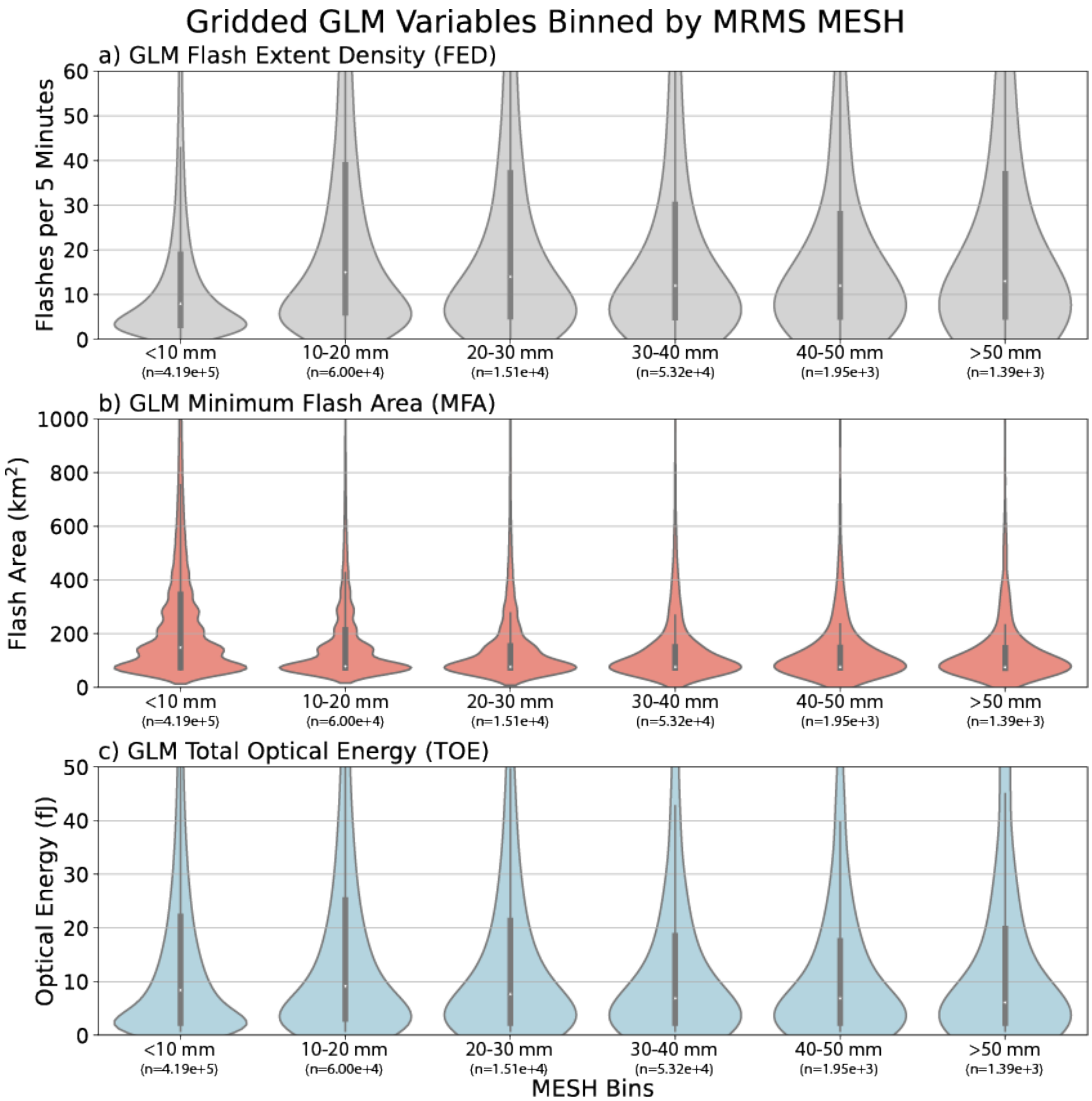

Figure 2.8: Distributions of the gridded GLM variables FED (a), MFA (b), and TOE (c) binned with respect to their corresponding MESH values every 10 mm.

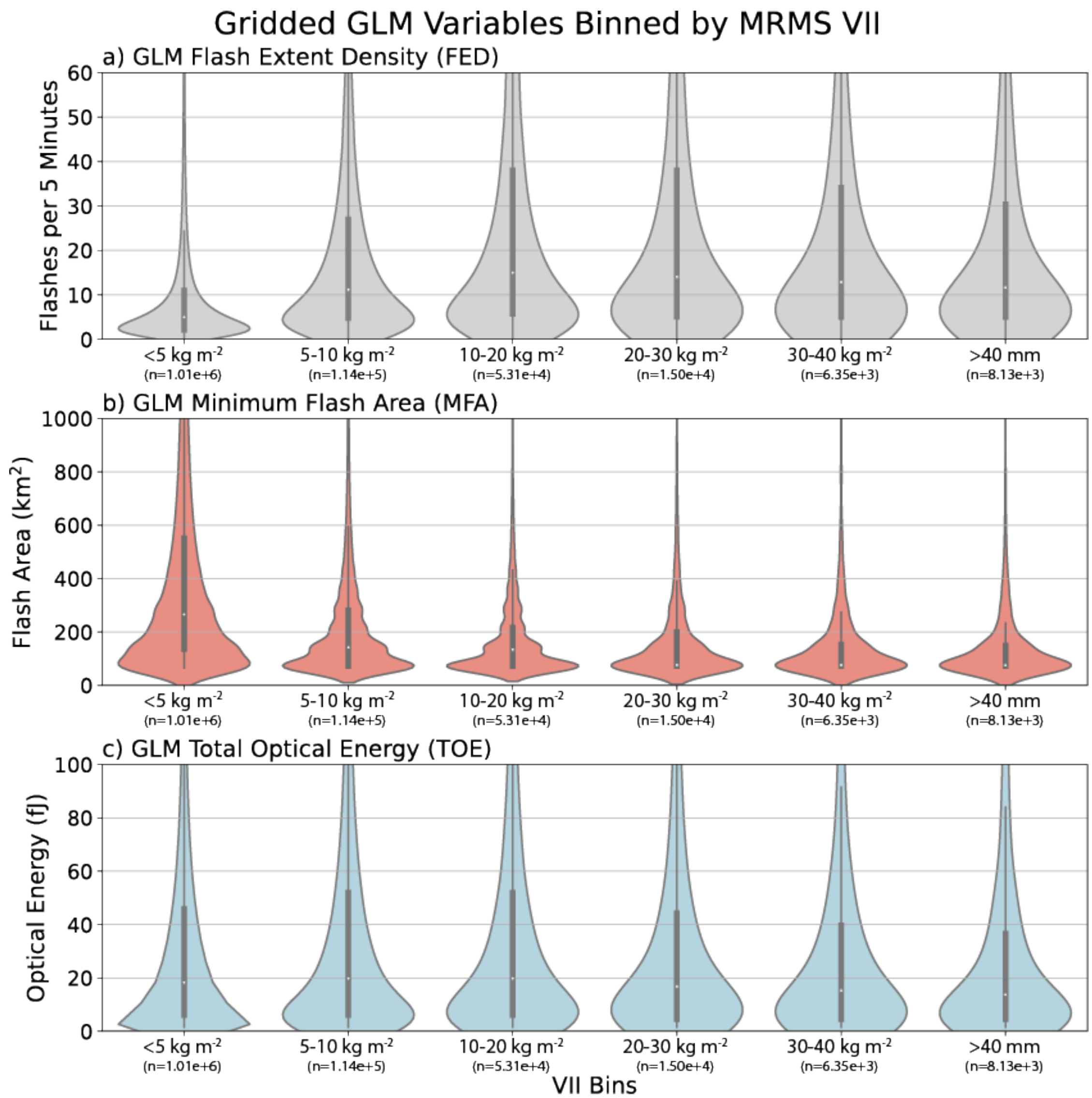

Figure 2.9: Distributions of the gridded GLM variables FED (a), MFA (b), and TOE (c) binned with respect to their corresponding VII values every 5 kg m^{-2} below 10 kg m^{-2}, and every 10 kg m^{-2} for values greater than 10 kg m^{-2}.

2.5 Discussion

2.5.1 GLM Data Fusion Applications

GLM Flash Extent Density corresponded inversely to local flash area in both supercell case studies and the larger 7-week study. Decreases in flash area, as reported from the local minima in MFA, for each supercell case (Figures 2.1 and 2.3) coincided with increasing maximum FED values and storm-total flash rates from the GLM16, GLM17, and ENTLN. The inverse relationship between local flash rates and areas was readily observed in the bulk study when the median, gridded GLM variables were plotted with respect to binned MRMS -10 °C isothermal reflectivities and ABI clean-IR brightness temperatures (Figure 2.6). For samples that coincided with severe convection (Figure 2.7), the inverse flash rate to flash area relationship persisted. Additionally, when binned by MRMS VII and MESH, FED and MFA presented relatively high and low values respectively when MESH exceeded 20 mm and VII exceeded 10 kg m^{-2}. The inverse relationship between local flash rate and area observed in the case studies and bulk study support the results from previous studies (Bruning and MacGorman 2013; Calhoun et al. 2013; Schultz et al. 2015). Elevated -10 °C isothermal reflectivity values, often exceeding 30 dBZ, can signal active charge separation within intensifying or robust convective updrafts (Buechler and Goodman 1990; Hondl and Eilts 1994; Mosier et al. 2011).

During the 24 May 2019 supercell case, updraft intensification at 2030 UTC from the GLM16 and GLM17-FED and -MFA values marked the onset of increasing trends from MRMS MESH, VII, and isothermal reflectivity. When considering the ambient deep-layer shear and unstable thermodynamic environment, this signaled the thunderstorm had transitioned into a supercell. Onset of the rightward deviation of storm motion from the mean wind, noted at 2040 UTC, was driven by the linear dynamic pressure perturbation of the mesocyclone (Rotunno and Klemp 1982; Bunkers et al. 2000; Flournoy et al. 2021). Increasing lightning activity during this period of mesocyclogenesis further supports the observations from a majority of supercells observed by Stough et al. (2017), and shows that pairing MRMS isothermal and vertically integrated reflectivity products with GLM gridded imagery can provide complementary information for thunderstorm morphology and subsequent trends in severity potential.

Environments conducive to larger GLM flashes were also observed using the binned ABI brightness temperature and MRMS -10 °C isothermal reflectivity in Figure 2.6, which exhibited a peak in MFA values between isothermal reflectivity values of 20-30 dBZ and brightness temperatures of 210-230 K. The combination of large flash areas with relatively low flash rates suggest that these scenarios contained a greater proportion of flashes which propagated through regions of stratiform precipitation supportive of local charge separation. Mecikalski and Carey (2018) showed from a sample of 27 mesoscale convective systems that a greater proportion of flashes were shown to propagate through regions of MRMS three-dimensional reflectivity between 20 and 30 dBZ, indicating an overall preference to larger, stratiform flashes within these reflectivities. While the reflectivity values sampled in the bulk study are restricted to the -10 °C isothermal layer, the larger spatial footprint of lightning flashes provided by the GLM shows that a majority of flashes between isothermal reflectivity values of 20-30 dBZ and brightness temperatures 210-230 K were associated with stratiform flashes. Operationally, a forecaster could use these values to highlight regions with the potential for large flashes that can expose the public to excessive lightning risk.

One additional caveat to this analysis can be found at the beginning of the 25 May 2019 supercell case study. MFA values from the storm exceeded 800 km^2, and coincided with ABI brightness temperatures between 210 and 220 K along with isothermal reflectivity values between 40 and 45 dBZ. Ongoing convection was noted near the storm of interest, with anvil regions from decaying convection present to the west and within 5 km identified from ABI16 brightness temperature data. Local charging within these anvil regions, and the presence of large flashes beyond the existing footprint of the developing storm, may have initiated in part due to interactions with the developing storm or from local initiation within the anvil as noted in Kuhlman et al. (2009) and Weiss et al. (2012). Because large, stratiform flashes can initiate in a variety of convective environments, the operational need to identify these electrified regions within stratified reflectivity and infrared brightness temperature regions remains a necessary area of study.

Gridded GLM products from the current study were evaluated in NOAA's Hazardous Weather Testbed - Experimental Warning Program (Calhoun et al. 2021). FED and MFA consistently received recommendations for operational implementation (Thiel and Calhoun 2021; Thiel 2022). The TOE product has been considered, however, specific applications within the context of short-term convective forecasting have been met with uncertainly by HWT participants (Thiel 2022). The qualitative feedback from the testbed was observed quantitatively in the presented study, as TOE did not present robust interrelationships with ABI, MRMS, and the other GLM variables within the study. Within the bulk study, trends in TOE did not correspond well with isothermal reflectivity in Figures 2.6 and 2.7 but did with respect to cloud-top brightness temperature. One possible explanation for these poor relationships is that the observed optical energy from a lightning flash varies with respect to not only the optical properties of the ambient convective cloud (Brunner and Bitzer 2020; Peterson 2020), but also the emitting properties of the lightning channels themselves (Thomas et al. 2000; Petersen and Beasley 2013). This presents considerable challenges for operational implementation of TOE, as HWT participants have shown reduced confidence and perceived utility in TOE when compared to FED and MFA (Thiel and Calhoun 2021; Thiel 2022).

2.5.2 Dual-GLM Observations

During both supercell cases, GLM16 observed greater storm-total and localized flash rates than GLM17 overall. However, the ratio of GLM16 to GLM17 flash rates varied temporally, with periods in both cases where GLM17-FED values exceeded those from GLM16. This occurred even at greater GLM17 viewing angles such as the 25 March 2021 case in the southeastern CONUS. Bateman et al. (2021) found average GLM16 detection efficiencies exceeded 70% in the southeastern, south central, and central CONUS regions, while GLM17 values were often below 50% in the southeastern CONUS and between 50% and 70% in the south and central CONUS regions. Rudlosky and Virts (2021) demonstrated relative differences in local GLM flash rates between GLM16 and GLM17 in the region of sensor overlap. In the southeastern CONUS, GLM16 observed nearly all of the flashes detected by GLM17, which observed approximately 50% of all GLM16 flashes. GLM16 also observed slightly more flashes in the central and southeastern CONUS regions than GLM17. Therefore, in both case studies presented GLM16 should observe more flashes than GLM17. This expectation was met throughout each case, with exception to times when the supercells intensified.

When GLM17-FED exceeded GLM16 values during the 24 May 2019 case between 2020 and 2030 UTC (Figure 2.1), storm total flash rates increased, MFA values decreased, and maximum TOE values from GLM17 increased to become almost twice as great as those from GLM16 by 2032 UTC. In the bulk study, increased FED frequently corresponded with increasing TOE near severe weather and all cases (Figures 2.6 and 2.7). However, there was a discrepancy when examining the FED and TOE imagery at 2032 UTC (Figure 2.10 a-d) where GLM17 observed greater TOE values in an area where GLM16 observed greater FED. As discussed previously, the GLM intensification signature signaled the onset of a mature supercell with a robust updraft and mesocyclone. Comparably, the 25 March 2021 supercell case also contained a period where local maxima in GLM16-FED and GLM17-FED were comparable (Figure 2.10 e-h), where GLM17 observed considerably greater TOE. MFA values also decreased just after 1730 UTC in Figure 2.3, and there was a greater disparity in maximum TOE values between GLM16 and GLM17 while their storm-total flash rates became comparable. This occurred before the second reported tornado in the case, along with over 30 minutes earlier before the first tornado. Both supercell storms, while viewed from considerably different GLM viewing angles and convective environments, presented different indicators of intensification. GLM17 observed greater optical energy signatures from greater TOE values, but only when the instrument had a direct view of the side of the intensifying updraft. Because GLM16 was in a more favorable position for flash detections than GLM17, the instrument still had greater FED values and storm-total flash rates than GLM17.

The two case studies provide instances of anomalous GLM16-to-GLM17 activity when compared to the bulk statistics provided by Bateman et al. (2021) and Rudlosky and Virts (2021), and show that the quality of GLM observations is impacted by the propagation of visible and near-infrared light originating from each lightning flash through a convective cloud. Previous studies using Monte Carlo simulations and Boltzmann transport theory to characterize the propagation of photons through a convective cloud have shown that the vertical and horizontal position of the simulated optical source provides the largest effect on the amount of light that escapes from the top and sides of the convective cloud (Thomson and Krider 1982; Light et al. 2001; Brunner and Bitzer 2020; Peterson et al. 2020). Brunner and Bitzer (2020) found that while changes in the size distributions of cloud droplets and ice particles more greatly influenced optical emission than the concentration of the particles, the optical source

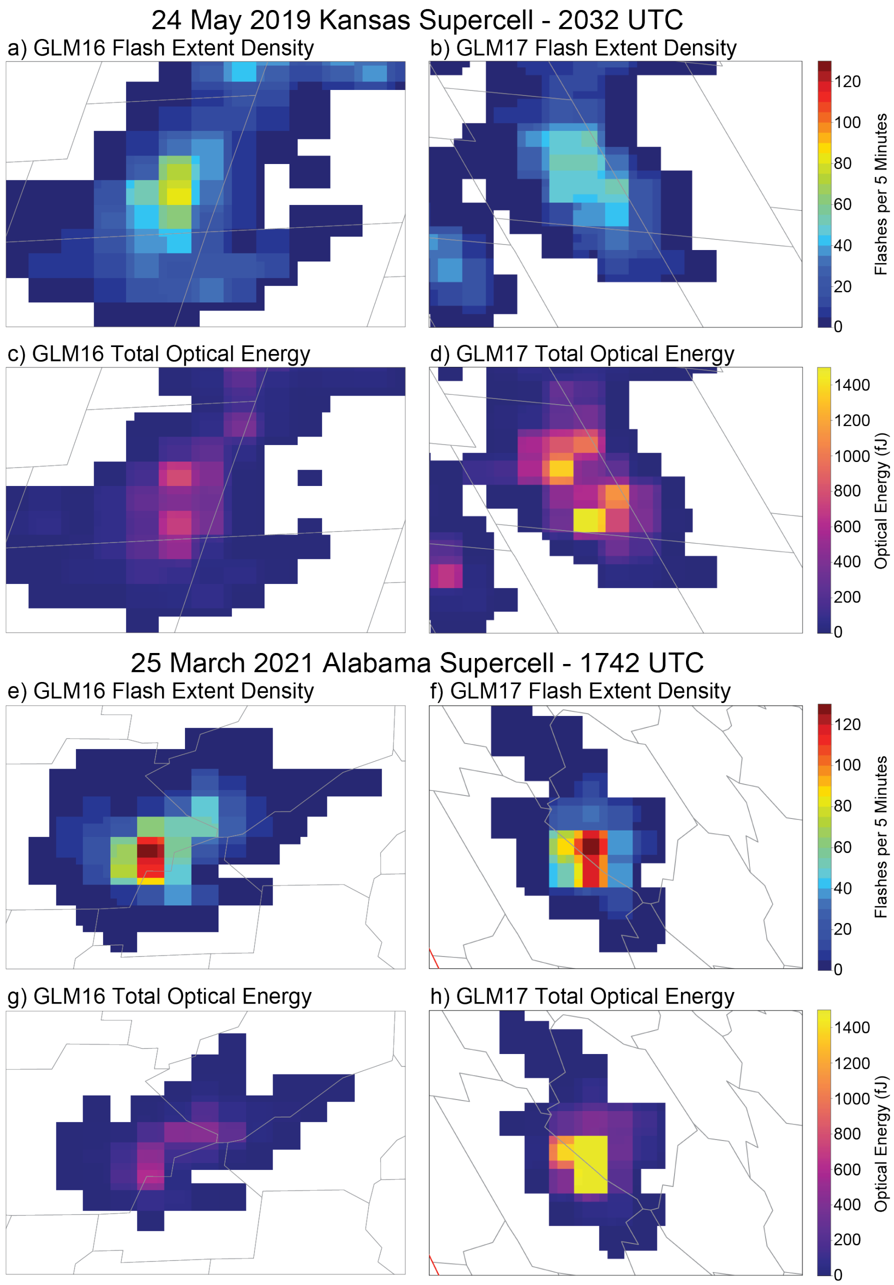

Figure 2.10: Snapshots of GLM Flash Extent Density (a, b, e, and f) and Total Optical Energy (c, d, g, and h) for two case studies from 24 May 2019 and 25 March 2021 from the perspective of GOES-16 (75 °W) and GOES-17 (137 °W).

height provided the largest impact on the amount of light that reached cloud top. This was especially apparent for source heights below 7 km. In supercell thunderstorms, Bruning and MacGorman (2013) showed that a greater number of flashes can occur upshear of the updraft. For both supercell thunderstorms studied, GLM17 had a more direct view of the flashes coinciding with each supercell's updraft due to its western perspective in these semi-discrete cases. This suggests that in certain scenarios with discrete updrafts in regions of moderate westerly shear, the GLM17 instrument may be able to capture more of the small flashes on the upshear side with higher optical radiances that help characterize updraft intensity trends.

Overall detection efficiencies from the GLM in the GOES-East position are still greater than overall in the south central, central, and southeastern CONUS regions than from the GOES-West GLM. However both case studies suggest that the additional perspective from the GOES-West position may provide useful lightning information in short-term convective forecasting, specifically related to rapid increases in updraft speed and volume prior to severe weather occurrence (Schultz et al. 2015, 2017). Total Optical Energy in particular appeared to be most useful when assessing temporal changes in GLM DE from both supercells, and additional dual-GLM studies are needed to confirm the consistency and predictive value of this TOE signature. During the 2022 Satellite Proving Ground HWT participants viewed initiating convection in the central United States from GLM16 and GLM17 (Thiel 2022), and similar anomalies in GLM16 and GLM17 FED and TOE values to the two presented case studies were observed in regions of increased deep-layer shear. The displaced convective anvils to the east and also provided GLM17 a more direct perspective of the storm's updrafts. Thiel (2022) also reported that from these observations, testbed participants supported increased dual-GLM training along with merged-GLM products in regions of overlap. Additionally, the day/night variations in GLM flash DE (Bateman et al. 2021) from each sensor may limit the optical energy differences to daytime convection, as both supercells occurred during the day.

Chapter 3

Identifying and Characterizing GLM 'First Flashes'

3.1 Motivation

The GOES-R GLMs provide continuous lightning detections across the CONUS, with an increasing length of record since 2017. This record, when coupled with lightning detections from the GOES-East and GOES-West GLM perspectives, allows lightning and its parent convection to be studied on larger spatial and temporal scales (Rudlosky and Virts 2021) without the spatial limitations from ground based lightning networks (Rudlosky 2015; Cummins and Murphy 2009). Previous studies of lightning activity have employed thunder-hours – the number of hours with observed lightning within a predetermined area – to describe the location and duration of convective activity across the CONUS region and globally (Taszarek et al. 2020; DiGangi et al. 2022). These studies provide insights into total thunderstorm activity, however assessing their ability to characterize developing convection was beyond their scope.

The development of deep, moist convective updrafts, known as deep convection initiation (DCI) poses a considerable nowcasting challenge due to synoptic and mesoscale forcing, the subtle interactions between convective instability, convective inhibition, and vertical wind shear (Markowski 2007). Therefore the ability to study and characterize DCI may provide insight into the observations and processes that govern convective development. Several studies have employed radar data and satellite imagery - both subjectively and objectively - across the Continental United States to study

DCI frequency and its attributes (Banta and Schaaf 1987; Tawfik et al. 2015; Reif and Bluestein 2017; Shield and Houston 2024). Ground-based radar studies of DCI from Reif and Bluestein (2017) and Shield and Houston (2024) spanned 20 years and 11 years respectively, which Reif and Bluestein (2017) used to characterize overnight convection in the Central United States and Shield and Houston (2024) used to study inter-annual variability in the same region. The scope of these works has been limited by the availability and quality of radar data from the WSR-88D network, with decreased coverage in the western United States. Manzato et al. (2022) used fourteen years of ground-based, cloud-to-ground lightning data over the Alpine area in Europe to study DCI timing and location in a region characterized by poor radar coverage. By studying developing thunderstorms through their related lightning activity, these domains of study may be expanded to cover the Continental United States with data from the GOES-East and GOES-West GLM.

It is expected that by studying developing convection and their first lightning flashes (hereafter referred to as first flashes) from the perspective of the GLM, thunderstorms at this stage across the CONUS can be studied with respect to other datasets such as satellite imagery (Banta and Schaaf 1987; Roberts and Rutledge 2003; Elsenheimer and Gravelle 2019; Cintineo et al. 2022) and radar (Stolzenburg et al. 2015). This study will attempt to use the GOES-R GLM to identify and characterize first flashes across the Continental United States with data from GLM16 and GLM17 in 2022. First flashes will be manually identified and studied with respect to ground based lightning networks in two case studies, followed by a manual analysis study of over three-thousand candidate first flashes to inform the selection of objective identification criteria. Lastly, these identification criteria will be applied to all GLM16 and GLM17 flashes across the CONUS for all of 2022. These data will be compared against satellite imagery, radar data, and a ground based lightning network to characterize first flashes and the signals associated with developing thunderstorms across the CONUS.

3.2 Data

3.2.1 Lightning Data

GLM16 and GLM17 were selected for their near-continuous coverage throughout 2022 and near-identical instrument configurations. Level 2 (L2) data from the operational GLM Lightning Cluster Filter Algorithm (LCFA) (Goodman et al. 2012) were used in this study and included flashes, groups, and events. Events are the individual pixels detected by the GLM based on rapid changes in brightness compared to a background image at the 777.4 nm wavelength, within a 2 ms frame rate. Adjacent events within the same frame are combined into groups, and all groups within 16.5 km and 330 ms are clustered into flashes. Flash, group and event level data from GLM16 and GLM17 were obtained to fully leverage the optical and spatial qualities of the flashes from geostationary orbit.

Lightning observations in the radio-frequency spectrum were collected from the ENTLN (hereafter referred to as ENI from Chapter 2) (Zhu et al. 2022) and Lightning Mapping Arrays (LMAs) (Rison et al. 1999; Thomas et al. 2004). By studying ENI flashes in 2022, this study can leverage these network improvements alongside the nearly continuous observations from GLM16 and GLM17. Meanwhile LMAs detect the time of arrival of lightning discharges to locate sources with a high degree of spatial (tens of meters) and temporal (tens of nanoseconds) accuracy (Thomas et al. 2004). The mapping of multiple sources can depict the origin and propagation of lightning flashes, with traditionally 10 sources, each detected from six or more stations, clustered within 3 km and 150 ms of each other being classified as a flash (Bruning and Bitzer

2023). Monte Carlo and curvature matrix model simulations from Chmielewski and Bruning (2016) revealed that flash detection efficiency often exceeds 95% within 100 km from the center of each cluster. Additionally, source detection efficiency and location errors depend on the configuration of LMA stations, the detection thresholds employed, and the range and altitude of the sources from the lightning flash.

In the very high radio frequency range, LMA data were collected from the Oklahoma LMA (hereafter 'OK-LMA') (MacGorman et al. 2008; Chmielewski et al. 2022a) and the National Severe Storms Laboratory Deployable LMA (hereafter 'NSSL LMA') during the Propagation, Evolution, and Rotation in Linear Storms (PERiLS) project (Kosiba et al. 2024; Chmielewski et al. 2022b) in 2022. The NSSL LMA consisted of eight deployable LMA stations positioned ahead of an anticipated quasi-linear convective system (QLCS), while the OK-LMA consisted of two clusters with 11 fixed stations in central Oklahoma and 7 fixed stations in southwest Oklahoma (Barth et al. 2015). Individual first flashes from a PERiLS deployment on 22 March 2022 and from the OK-LMA domain on 23 April 2024 were manually identified using the available LMA, GLM, and ENI flashes and analyzed to understand how multiple lightning location systems (LLSs) view first flashes. Lastly, only flashes from central Oklahoma – within the northeast cluster – of the OK-LMA were studied as only seven stations from the northeast cluster and three stations from the southwest cluster were available during the event.

3.2.2 Satellite Imagery and Radar Data

ABI16 data were employed again for this study form the CONUS scene. Clean–IR Brightness Temperatures (hereafter referred to as the cloud-top T_B). Cloud–top information at a resolution of 2 km from the cloud-top T_B help characterize developing convection from glaciating processes (Roberts and Rutledge 2003; Elsenheimer and

Gravelle 2019; Cintineo et al. 2022), features indicative of potential severe updrafts such as overshooting tops and above-anvil cirrus plumes (Adler et al. 1983; Bedka et al. 2018), and convective updraft strength with respect to local GLM flash density and area (Thiel et al. 2020). The second product used was the ABI Cloud–Top Height Algorithm (ACHA), which uses ABI bands from the 11.2, 12.3, and 13.3 μm wavelengths and profiles from the Global Forecast System (GFS) to produce cloud–top heights at a 10 km resolution for all pixels classified as cloudy by the ACM.

Radar data were also collected from the MRMS system leveraged in Chapter 2, including composite reflectivity and the isothermal reflectivity at -10 °C product. Isothermal reflectivity at -10 °C (hereafter referred to as isothermal reflectivity) provides insight into the density and size of hydrometeors that are lofted into the mixed phase region by a convective updraft, and can characterize the likelihood of local hydrometeor charging leading to a lightning flash (Mosier et al. 2011) and the characteristics of lightning flashes with respect to severe thunderstorms (Chapter 2).

3.3 First Flashes from Multiple LLSs

3.3.1 23 March 2022 - NSSL LMA

Multiple first flashes were manually identified within the NSSL LMA domain during the PERiLS campaign (Figure 3.1a). Developing convection most often occurred rapidly along the leading edge of a quasi-linear convective system (QLCS). The first flash of interest however was from a cell on the periphery of the of the trailing stratiform precipitation region, which developed gradually over approximately 30 minutes. Isothermal reflectivities near the initial flash observed by the NSSL LMA were between 35 and 40 dBZ over a broad broad area to the southwest (Figure 3.1c), suggesting a larger more diffuse updraft with lower than average vertical velocities.

Spatial and temporal observations of the flash from GLM16, GLM17, ENI, and the NSSL LMA as presented in Figure 3.2 provided a detailed view of its characteristics and lightning processes. The first LMA source occurred at 18.824 seconds at an altitude of 4.7 km, and subsequent sources decreased in altitude with the first GLM16 group recorded shortly afterwards. After LMA sources decreased to 343 m two more GLM16 groups were recorded, followed by an identified cloud-to-ground (CG) lightning flash from ENI with two return strokes and a peak current of -6.66 kA. LMA sources remained between 2 to 6 km until approximately 19.07 seconds, when a maximum source energy of 29.4 dBW was recorded. The first GLM17 group was observed at this time too, with both GLM16 and GLM17 groups recording their highest optical energy values of 26.2 and 44.4 fJ respectively. LMA sources remained around 5 km before decreasing again leading up to 19.2 seconds and reached a minimum altitude below 200 m when the last GLM16 group was recorded.

A planar view of the flash from the LMA sources and GLM events showed considerable differences in the flash footprint from each platform. Reported flash areas from GLM16, GLM17, and the NSSL LMA were 554, 224, and 24.3 km^2 respectively. Flash durations also varied between each of the networks. The NSSL LMA reported a flash duration of 0.404 s, while ENI reported 0.302 s and GLM16 reported 0.372 s. Meanwhile GLM17 reported the shortest duration of 0.058 s, with only 3 groups and 7 events. In comparison, GLM16 recorded 13 groups and 42 events. GLM16 showed an increased sensitivity to the optical energy emissions from the lightning flash, with a reduced minimum event energy of 0.95 fJ, while the minimum event energy from GLM17 was 6.83 fJ.

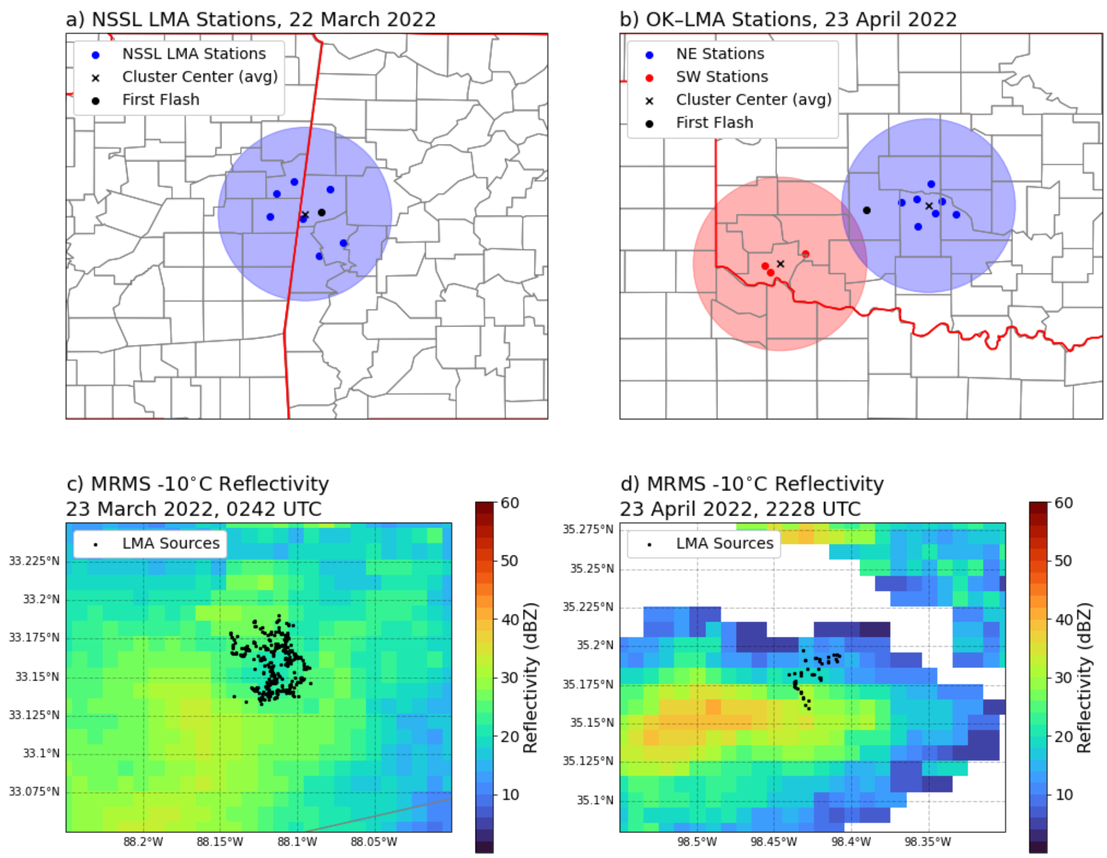

Figure 3.1: Maps of LMA station locations and first flash locations from the NSSL LMA on 22 March 2022 (a) and the OK-LMA on 23 April 2022 (b) with each circle showing the 100 km radius of study from the center of each network cluster. Planar views of the LMA sources from the NSSL LMA (c) and OK-LMA (d) coinciding with the MRMS -10 °C isolthermal reflectivity available at the time of the flash.

3.3.2 23 April 2022 - Oklahoma LMA

Similar to the previously described PERiLS study, first flashes were identified within the OK-LMA domain on 23 April 2022 (Figure 3.1b). Semi-discrete storms developed along a mesoscale boundary in west-central Oklahoma, oriented from the southwest to the northeast. Isothermal reflectivity values increased quickly and signaled robust charge separation within the concentrated updraft. Reflectivity values at 2228 UTC were over 40 dBZ as the storm moved northeastward along the boundary (Figure 3.1d).

The first lightning flash occurred at 2229 UTC between 51.4 and 51.7 seconds as shown in Figure 3.3, north of the local reflectivity maximum.

The first LMA source was recorded at 51.42 seconds at an altitude of 10.2 km and a source energy of 6.7 dBW. Successive source altitudes and energies increased to over 11 km and 23 dBW respectively, and altitudes remained over 9 km until the first GLM16 group was recorded at 51.55 seconds with an optical energy of 6.28 fJ. The final group from GLM16 at 51.68 seconds had the largest area at 150 km^2 and was the least luminous with an optical energy of 6.18 fJ. Around 51.69 seconds the OK-LMA recorded the final sources of the flash at just over 8.3 km, near the initiation point of the flash. No flash was reported during this time period and position from ENI and GLM17, and therefore we do not have a objective classification of flash type and polarity or a direction comparison with data collected by GLM16. Flash durations from the OK-LMA and GLM16 were 0.259 and 0.128 seconds respectively, with reported flash areas of 6.8 and 150 km^2. GLM16 collected three groups and four events, with a minimum event energy of 3.01 fJ.

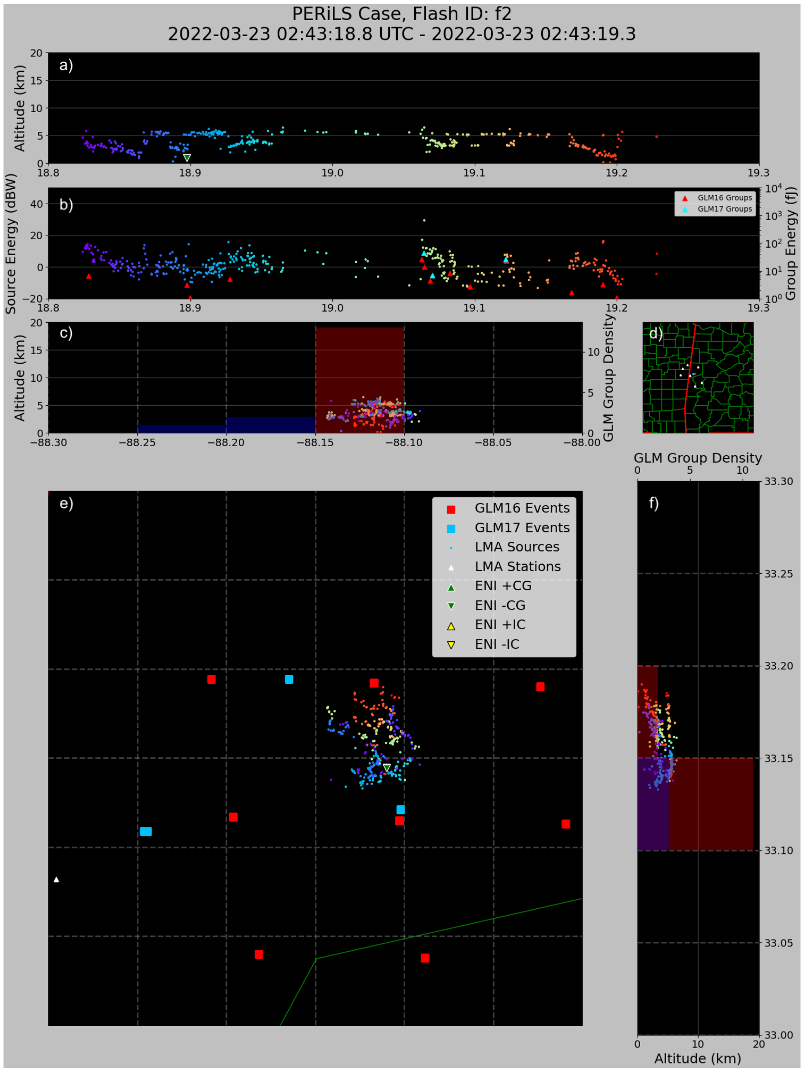

Figure 3.2: A manually identified first-flash from the NSSL LMA on the PERiLS campaign on 23 March 2022 at 0243 UTC from 18.8 to 19.3 seconds, with all LMA sources colored by time. Panel (a) is a time-series of LMA sources by altitude and the reported ENI flash time. Panel (b) is a time-series of LMA sources by energy (dBW) and GLM groups by optical energy (fJ). Panels (c) and (f) present LMA sources and GLM group densities by longitude and latitude respectively. Panel (d) displays the location of the flash from GLM16 and GLM17, along with the LMA station locations. Panel (e) maps the LMA sources, ENI flashes, and GLM16/GLM17 events by latitude and longitude.

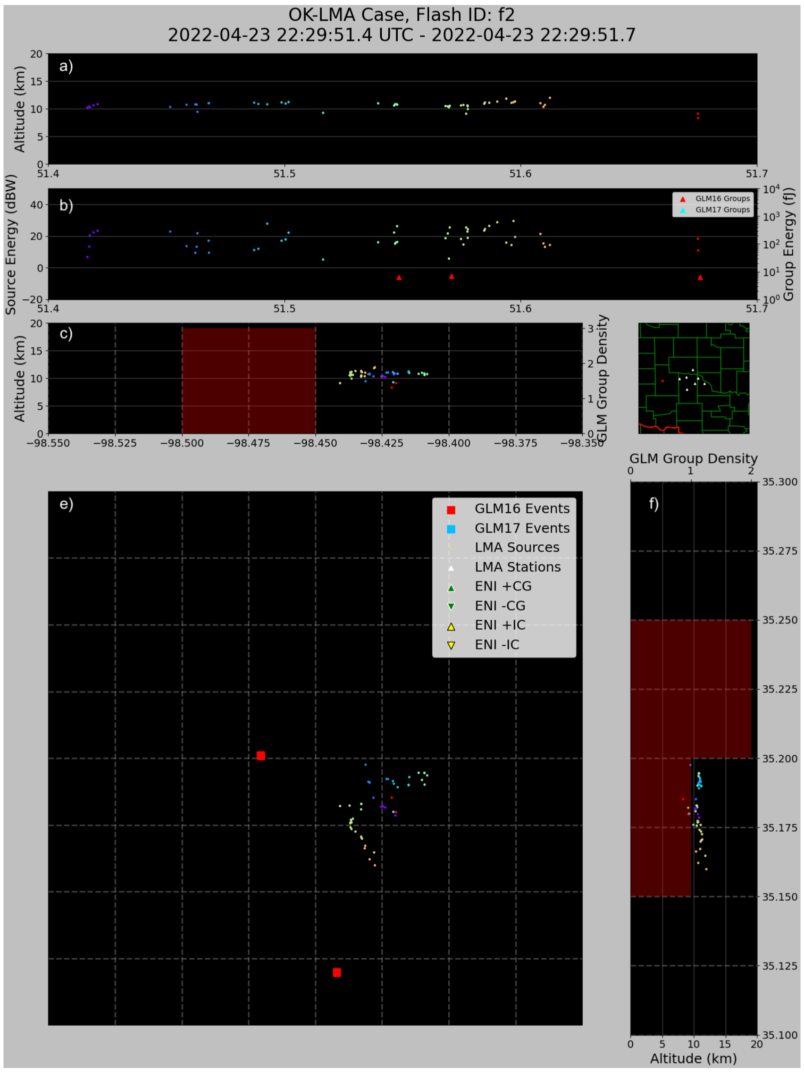

Figure 3.3: Similar to Figure 3.2 for a first-flash identified within the Oklahoma-LMA domain on 23 April 2022 from 51.4 to 51.7 seconds.

3.4 Manual Analysis

3.4.1 Procedure

First flashes were defined by manually analyzing many candidate flashes. Broadly, first flashes were defined as the first GLM lightning flash within a certain distance from other flashes over a specified time. The criteria for objectively identifying GLM first flashes are inherently subjective. Therefore, similar to tuning hyperparameters in a machine learning model (Géron 2019), 50 combinations of first flash criteria were evaluated to inform the selected criteria for this study. The first 25 combinations had distance criteria – from the flash centroid – from 10 to 50 km every 10 km, and time criteria from 10 to 50 minutes every 10 minutes. The next 25 combinations had the same time criteria range as the first 25 combinations, but the distance criteria ranged from 10 to 30 km every 5 km plus the 'flash area radius'. The radius of the GLM flash was calculated using the GLM flash area and by assuming the flash area was approximately circular. Early testing of various time-distance criteria found that larger flashes within regions of stratiform precipitation would be incorrectly classified as a first flash, and the expectation of including the flash area radius was to mitigate these effects. These 50 time–distance criteria were applied to seven cases of widespread convective development (Table 3.1), providing over three–thousand potential first flashes to manually investigate spread across the Continental United States (Figure 3.4). The potential first flashes were selected from the most lenient time and distance criteria (10 minutes and 10 km), and provided a baseline for the other 49 combinations.

Potential first flashes were identified using the most lenient search criterion of no other GLM lightning flashes within 10 minutes and 10 km of the current flash under investigation. This combination was first run over all seven cases to establish a baseline

Table 3.1: Information from the seven cases in 2022 used for manually analyzing GOES-16 GLM first flash candidates. Latitudes and longitudes are in degrees.

Case ID	**Start (UTC)**	**End (UTC)**	**Latitudes**	**Longitudes**
20220302-al	22 March, 1900	22 March, 2200	32.30 – 34.07	-89.10 – -87.43
20220423-ok	23 April, 2100	24 April, 0200	31.97 – 37.39	-101.03 – -94.11
20220504-tx	4 May, 1600	5 May, 0400	31.97 – 37.00	-103.00 – -95.14
20220612-co	12 June, 1900	13 June, 0300	37.00 – 45.85	-109.05 – -97.27
20220614-ne	14 June, 2200	15 June, 0600	37.32 – 43.25	-109.05 – -91.12
20220921-ut	21 Sept., 1600	21 Sept., 2000	39.59 – 44.67	-116.98 – -109.10
20220925-tn	25 Sept., 1500	26 Sept., 0100	35.17 – 38.29	-85.78 – -80.94

for evaluating all 50 combinations. The identification algorithm was then rerun for the other 49 combinations to establish a validation dataset. Ten minute composites of GLM and ENI flashes were plotted against ABI cloud-top T_B and MRMS isothermal reflectivity to identify regions of increasing lightning potential. These data were plotted every minute in the ten minutes before and five minutes after the potential first flash occurred. In the final minute leading up to the potential first flash, data were plotted every ten seconds along with the five seconds before and after the potential first flash. This series of 23 images were used to determine if the event was a first flash (Hit), not a first flash (False Alarm), or if the ENI observed a first flash event over five seconds before the GLM-identified first flash (Late). With each classification, a confidence value was subjectively assigned from 1 (Low confidence) to 5 (High confidence). Lastly, the primary location of the GLM flash was subjectively assigned based on if the flash coincided with a convective updraft (Convective core), the anvil region down shear of a parent updraft (Anvil), in a region of stratiform precipitation with no parent updraft (Stratiform), or in an unassigned category (Other).

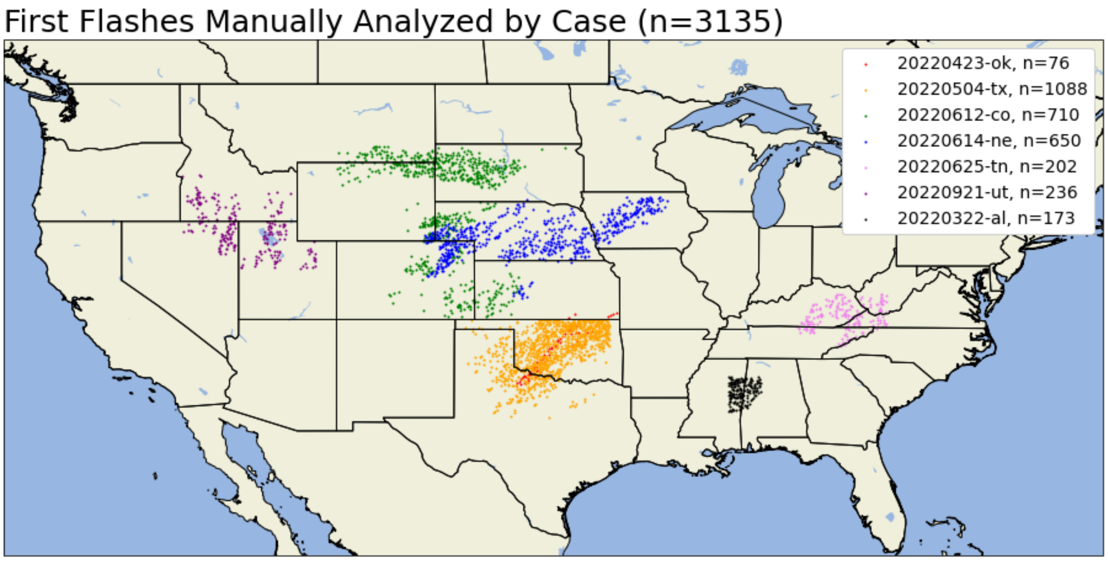

Figure 3.4: A map of all potential first flashes that were manually analyzed in the study. The color of each dot coincides with the case studied.

Each identification criteria provides a binary classification of first flashes against the binary classification from the manual analysis. The problem can therefore be posed in a contingency table as presented by Baldwin and Kain (2006) and shown in Figure 3.5, with true positive (a), false negative (b), false positive (c), and true negative (d) classifications. By assuming the most lenient criteria captures all first flashes, evaluation statistics such as the probability of detection (POD, Equation 3.1),

$$POD = \frac{a}{a+b} \tag{3.1}$$

false alarm ratio (FAR, Equation 3.2),

$$FAR = \frac{c}{a+c} \tag{3.2}$$

success ratio (SR, Equation 3.3),

$$SR = 1 - POD \tag{3.3}$$

and critical success index (CSI, Equation 3.4)

$$CSI = \frac{a}{a + b + c} \tag{3.4}$$

could be calculated (Baldwin and Kain 2006; Barnes et al. 2009). Each identification criteria can then be viewed as a function of SR, FAR, and CSI on a performance diagram (Roebber 2009) to inform the selection of criteria to apply for all GLM data in the 2022 bulk study.

Observed		**Predicted: No**	**Predicted: Yes**
	No	**True Negative (d)**	**False Positive (c)**
	Yes	**False Negative (b)**	**True Positive (a)**

Figure 3.5: A contingency table showing the outcomes of a binary classification between the predicted and observed labels.

3.4.2 Results

Manually analyzed flashes were frequently placed into three categories: 1) First flash in the convective core, 2) Flashes propagating through thunderstorm anvils or stratiform precipitation regions, and 3) GLM flash geolocation errors. Examples of each scenario were found in the 4 May 2022 case in Texas and Oklahoma (20220504-tx) and shown in Figure 3.6. The first example from Figures 3.6a and b shows a manually verified first flash that comes from a developing convective updraft. Decreasing cloud-top T_B and increasing -10 °C isothermal reflectivity in the previous ten minutes indicates cloud–top cooling coincident with glaciation as more hydrometeors are lofted into the mixed phase region where substantial charge separation can occur. At 1831 UTC and 33 seconds GLM16 and ENI both recorded a lightning flash as the updraft intensified over the next five minutes. All of this information led to the conclusion of a high–confidence first flash associated with a convective core.

In the next example, Figures 3.6c and d showed an intensifying supercell thunderstorm, evident by its constrained outflow in the cells forward and rear flanks along with rightward deviation from the mean wind. In the ten minutes leading up the potential first flash numerous lightning flashes were recorded by GLM16 and ENI that coincided with an updraft with notably colder cloud–top T_B and greater isothermal reflectivity near the updraft core. The potential first flash occurred at 1945 UTC and 37 seconds, down-shear from the flashes that coincided with a convective updraft and on the edge of the forward flank precipitation region. This placed the flash within the anvil of an already ongoing storm and was therefore a false alarm. Similarly, the last example in Figures 3.6e and f was also identified as a false alarm from a mature supercell thunderstorm. However the location of the GLM flash did not align with the other recorded GLM or ENI flashes, brightness temperatures, or isothermal reflectivity values. Instead, the flash was southeast of the storm in a region with no convective activity during the entire fifteen minute period of investigation. Based on the southeast displacement of the flash from the convective core and no convection within the area, this flash was determined to be a false alarm in a convective scenario of 'Other' with the most probable cause being a geolocation error from the GLM LCFA lightning ellipsoid.

Instances like the three presented previously were identified and categorized across all 3135 events shown in Figure 3.4, and their categorizations are shown in Figures 3.7a and b. Over three–quarters of all candidate flashes investigated (2364) were classified as a false alarm when using the 10 km and 10 minute criteria from the established baseline. Conversely, just under one–quarter of all flashes (771) were confirmed as a first flash from the perspective of the GLM with 8.9% (280) classified as 'Late' with respect to the ENI flash detections. When classified by convective scenario nearly half of all flashes were associated with a convective core (1563), while over one–third (1050) were classified within an anvil region. Approximately 10% (374) of flashes were classified within a stratiform precipitation region, with the remaining 184 flashes classified as 'Other' due to geolocation errors. Of the 280 'Late' flashes with respect to ENI, the GLM–identified first flashes were often recorded within the next five minutes, with ninety GLM flashes observed one minute or less before the ENI–identified first flashes (Figure 3.8).

When examining the scenario and classification categories jointly (Figure 3.7a), false alarms from the anvil region were most common with 994 occurrences followed by 859 flashes from the convective core. Flashes classified as hit or late were most often in the convective core with 704 flashes, while 56 flashes occurred in the anvil region. Relatively few flashes (11) classified as 'Hit' or 'Late' and had scenarios categorized as stratiform or other. The joint distribution of classification and confidence level of manually analyzed flashes (Figure 3.7b) offers a different perspective, with a strong majority of flash classifications receiving the highest confidence level of five. Of the 2482 flashes with a confidence level of five, over 80% of them coincided with flashes

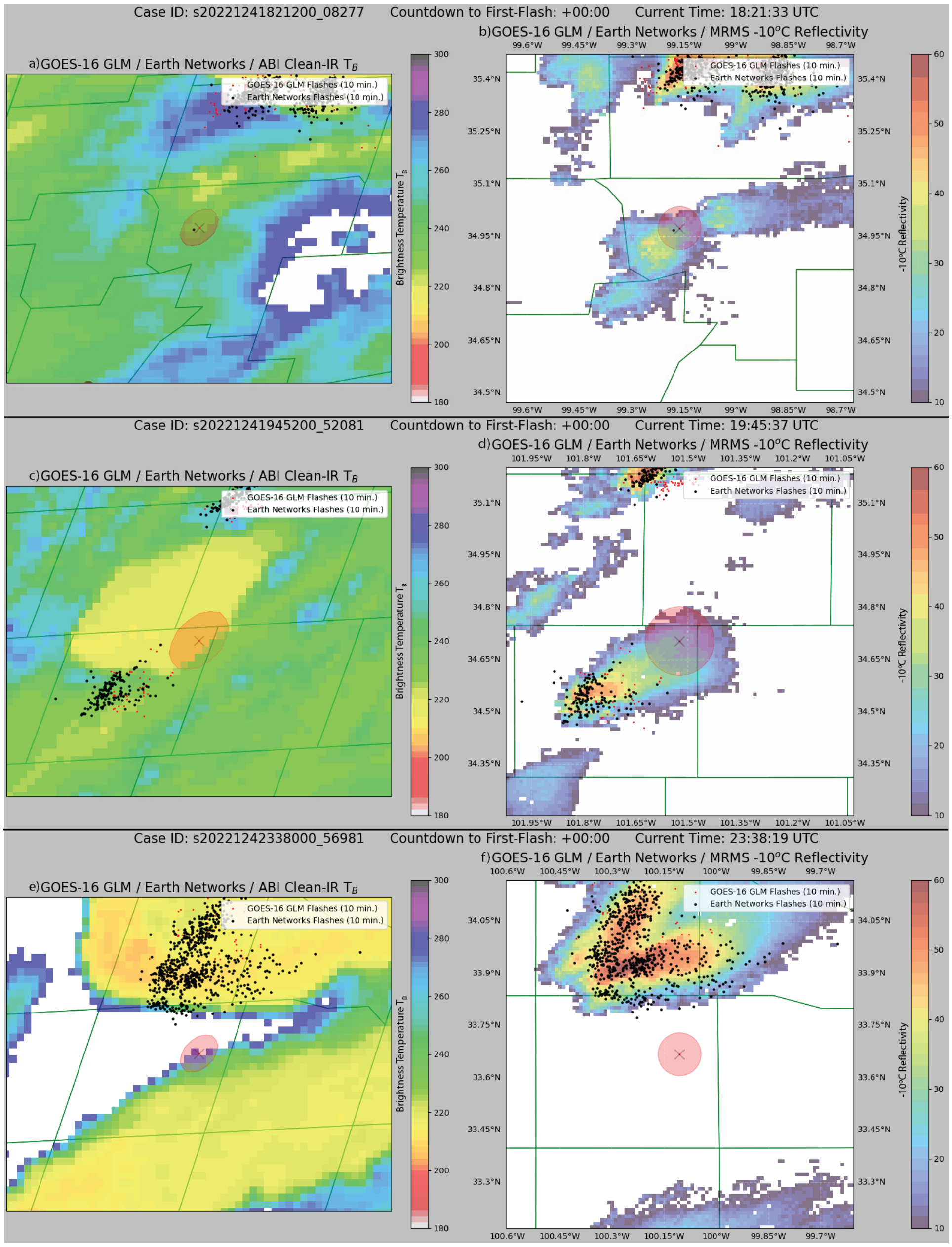

Figure 3.6: First flash examples from the 4 May 2022 manual analysis case in Texas (20220504-tx) of a 'Hit' (a,b), 'False Alarm' (c,d), and 'Miscellaneous' (e,,f) flashes at the time of occurrence. Panels a, c, and e show ten-minute accumulations of GLM (red) and ENI (black) flash locations overlaid on the coincident GOES-16 ABI Clean–IR Brightness Temperature, with the first flash location noted by the red circle. The size of the circle corresponds to the reported GLM flash area. Similarly, panels b, d, and f show the same GLM and ENI flashes but overlaid on the coincident MRMS -10 °C reflectivity.

in the convective core or anvil region. The confidence level distribution with the most spread per flash classification were those associated with convective cores, as levels two, three, and four all contained over 100 flashes.

Manually assigned flash classifications when using the most lenient flash identification criteria (10 minutes and 10 km) created a baseline from which all other combinations of identification criteria can be assessed. Assuming a POD of 1 (100%) for these criteria (Combination 0) if 'Late' flashes are also assumed as a 'Hit', then the POD, FAR, and SR were calculated and plotted as a performance diagram for all confidence thresholds (Figure 3.9a). For combinations 0 through 24 without the flash area radius addition changes in the distance – especially for the lower thresholds – yields substantial decreases in POD and SR. When increasing the time criterion across all 50 combinations, POD decreases with comparatively smaller increases in SR. POD values range between 0.1 and 1.0, while SR values range between 0.3 and 1.0. Combinations 1 and 25 sit closest to the bias line of 1, with POD and SR values of approximately 0.6, and maximize their CSI values near 0.4. While this may be the optimal choice statistically, a more conservative approach was necessary to balance between algorithm performance and an acceptable signal-to-noise ratio between the 'Hits' and 'False Alarms' when studying a bulk dataset. Performance statistics were recalculated for only scenarios with the highest confidence level of five and plotted in Figure 3.9b to interpret the sensitivity each metric and combination. By removing the lower confidence flash classifications, the POD and SR increased and numerous combinations had CSI exceeding 0.4. To optimize between the algorithm performance, desiring a sufficiently large dataset to sample, and the need penalize false alarms combination number 32 (20 minutes and 20 km plus the flash area radius) was selected to employ for the bulk study. The detection efficiency of first flashes using the selected criterion

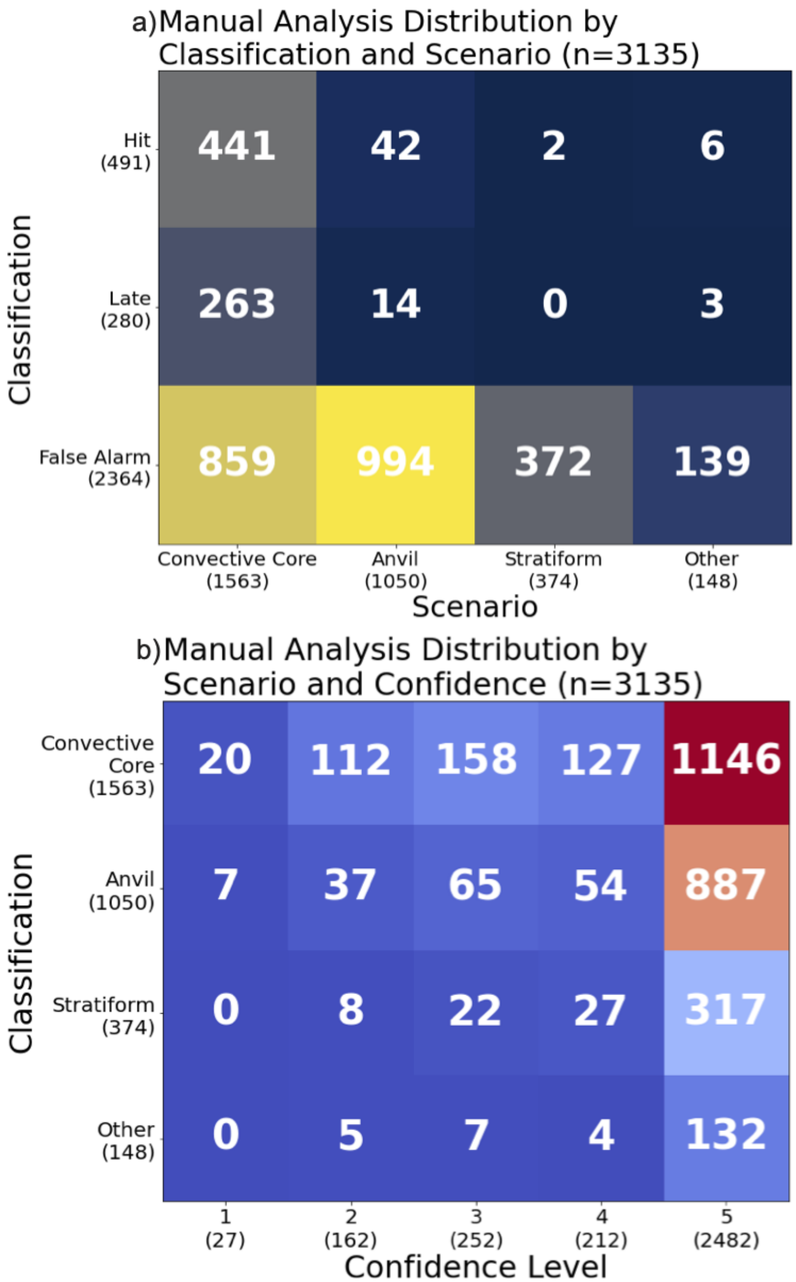

Figure 3.7: Two–dimensional histograms from the manually analyzed potential first flashes showing the distributions of scenarios versus classifications (a), and classifications versus confidence levels (b).

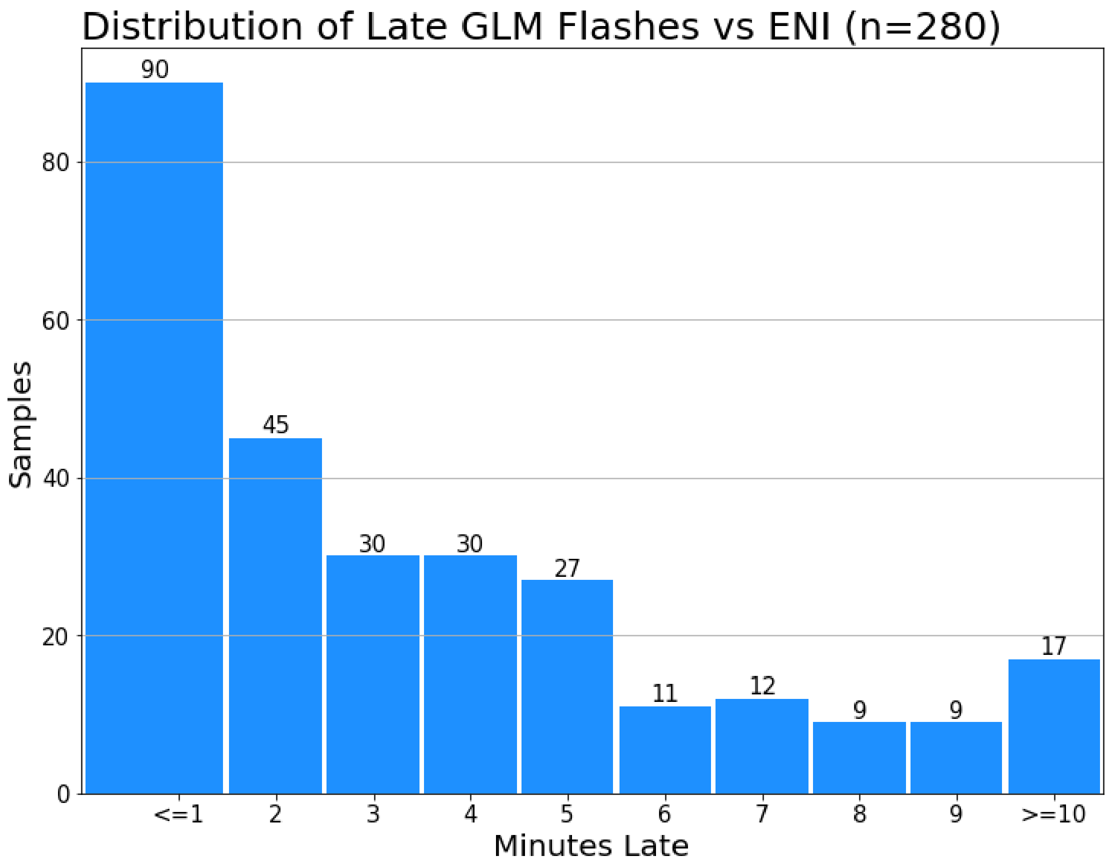

Figure 3.8: A histogram of the manually classified 'Late' GLM first flashes by time, relative to identified ENI flashes that were designated as the first flash.

was approximately 40%, with a false alarm ratio of 5% to 10%. By assuming the flash's footprint was circular, the radius of the flash was calculated from the GLM flash area and included to bias our classified flashes away from those which occur in stratified layers of charge such as thunderstorm anvils and regions of stratiform precipitation.

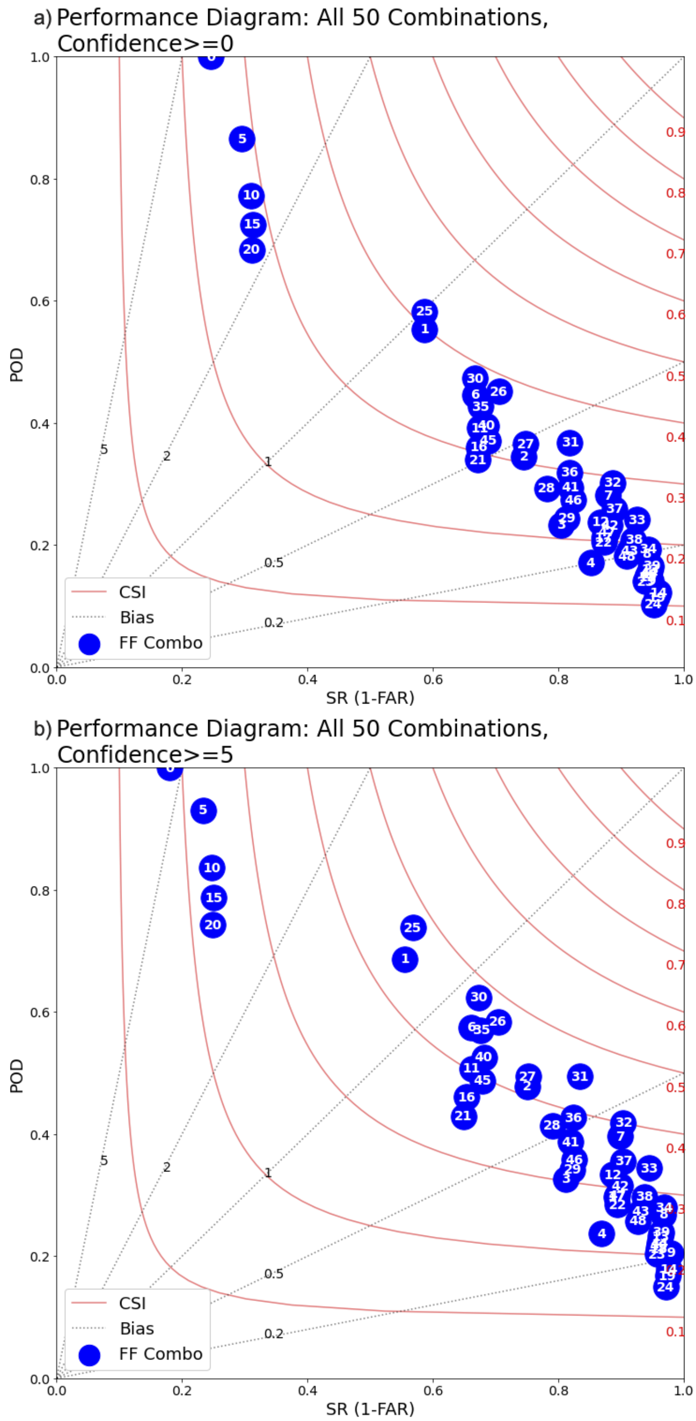

Figure 3.9: Performance diagrams of all fifty first flash combinations ('FF Combo' in legend) for all available confidence values (a) and for only flashes with the highest confidence value of five (b).

3.5 First Flashes Across the CONUS

3.5.1 Bulk Study Processing

Using the identification criteria previously discussed, first flashes were identified for all of 2022 from GLM16 and GLM17. Since lightning flashes in maritime convection have generally different characteristics (duration, area, optical energy, etc.) than in continental continental convection (Rudlosky et al. 2017; Rudlosky and Virts 2021) – and ensuring the quality of collocated isothermal reflectivity data from MRMS – flashes were required to occur on land within the Continental United States (CONUS).

ABI and MRMS variables were collected within a range of 20 km from the GLM first flash centroid, and the maximum values were sampled from the most recent data available. The ABI clear–sky mask applied to the ACHA data was also used against the Clean–IR T_B to ensure only cloud pixels were included in the study. The maximum values of ABI Cloud-Top Height, MRMS Composite Reflectivity, and MRMS Isothermal Reflectivity -10$^{/circ}$C were sampled, while the minimum ABI Clean-IR T_B was sampled. ENI flashes were matched with GLM first flashes using criteria similar to Rudlosky and Virts (2021) of 50 km from the GLM flash centroid and 200 ms from the GLM flash start and end times. If multiple ENI flashes matched with a GLM first flash, the ENI flash whose halfway point in time was closest to the corresponding GLM first flash halfway point was selected similar to Ringhausen et al. (2021). This method led to a matching fraction of approximately 73% for the period of study. To further validate the ENI classification of intra-cloud (IC) and cloud-to-ground (CG) flashes - and fill the unmatched GLM first flashes - a random forecast model trained by Ringhausen et al. (2021) (hereafter 'RRF') was employed. The RRF model classifies GLM flashes as IC or CG based on the characteristics of GLM flashes themselves, with a reported accuracy of approximately 75% over the CONUS domain.

3.5.2 Spatial and Temporal Distributions

Approximately 170-thousand first flashes from the GOES-East and GOES-West GLMs were objectively identified over all of 2022 (Figure 3.10). Greater spatial densities (>40 samples per 0.25° pixel) of first flashes (Figure 3.10) were collected in the southwestern United States (i.e. Arizona, Colorado, New Mexico, and Utah) which coincided with regions of elevated terrain. Similarly the southeastern U.S. (Alabama, Florida, Georgia, Louisiana, Mississippi, and South Carolina) also had increased samples, especially along the coasts of the Atlantic Ocean and Gulf of Mexico. Lastly, a highly concentrated region of first flash detections was recorded in northern Illinois. Lower first flash densities (<10 samples per 0.25° pixel) were identified along the coast of the Pacific Ocean and in the far northeastern United States. On a monthly basis (Figure 3.10b) August was the most frequent month for first flash occurrence with over 41-thousand first flashes, followed closely by July with over 40-thousand flashes. The least first flashes occurred in the wintertime months of December, January, and February, with January containing the lowest monthly total of 1354 flashes. From this minima in January the number of first flashes per month increased until the maxima in July and August, followed by a consistent decline through the rest of 2022 into December. A diurnal cycle of developing convection was present when all first flashes were binned hourly by their local solar time (LST) (Figure 3.10c). First flashes were least observed overnight between 0300 and 0400 LST with 3070 and 3073 flashes respectively. From 2200 LST to 0800 LST no hourly bin recorded more than 4-thousand first flashes. By 0900 LST the number of first flashes increased steadily through the period of maximum solar insolation (1200 LST) until its peak at 1400 LST with over 16-thousand flashes. After 1400 LST the number of first flashes decreased through the end of the day at 1800 LST and into the overnight hours.

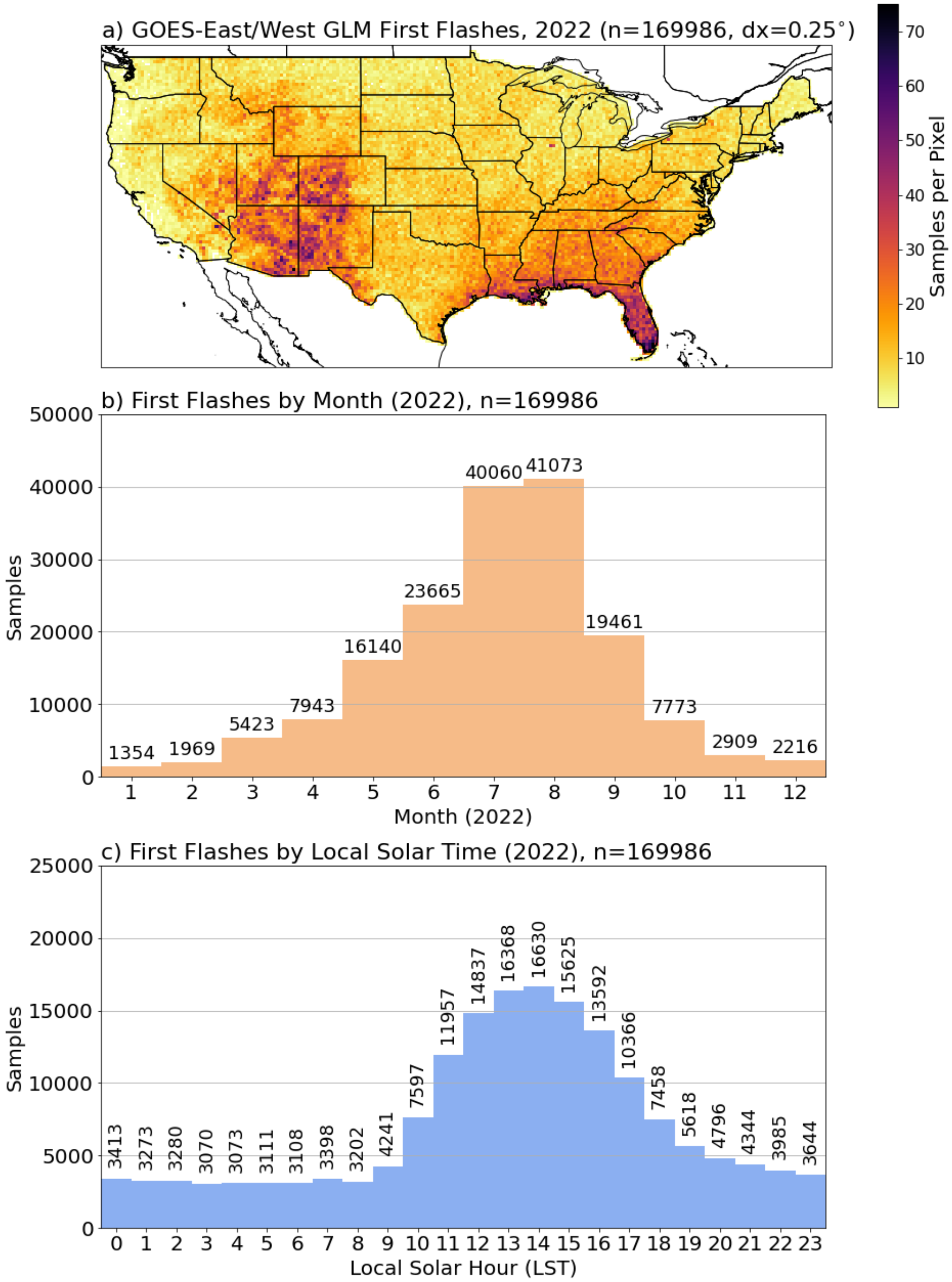

Figure 3.10: a) A two-dimensional density plot of GOES-East/West GLM first flashes from all of 2022, represented as the number of samples per a 0.25° latitude and longitude pixel. b) A histogram of GLM first flashes by month in 2022. c) A histogram of GLM first flashes binned by the local solar time (LST) on an hourly basis in 2022.

Spatial patterns in the temporal frequency of GLM first flashes can also be inferred when selecting the most common month and solar hour per a defined area of 1.0° latitude and longitude (Figure 3.11). On a monthly basis from Figure 3.11a, first flashes were most frequently recorded in the months of July and August similar to the distribution from Figure 3.10b. Greater monthly variability was observed in the Central and Northern Great Plains (Iowa, Kansas, Missouri, North Dakota, Nebraska, Oklahoma, Minnesota, and South Dakota) region of the United States, with modes of April, May, and June also observed. Additionally, regions along the coast of the Pacific Ocean in California had modes that extended into August, September, October, and December while further north the modes were more frequently the months of April and May. Spatial variations in the mode solar hour (Figure 3.11c) also appear similar to the distribution from Figure 3.10c, with mode solar hours between 1200 LST and 1600 LST observed over a vast majority of the United States. Across the Central and Northern Great Plains mode hours shifted to the overnight hours between 2000 LST and 0600 UTC.

3.5.3 GLM, ABI, and MRMS Attributes

All GLM first flashes were binned by season and the part of day by local solar time, and the distributions of their GLM flash characteristics were shown as box and whisker plots in Figure 3.12. Flash area distributions of GLM first flashes over each season and day segment (Figures 3.12a and b) showed the variability in flash sizes between 64 km^2 and over 1000 km^2. Median flash areas during the boreal spring, summer, and fall months were between 120 km^2 and 250 km^2, while the median first flash area during the winter month was around 400 km^2. During the morning (0600-1100 LST) and evening (1200-1700 LST) segments median first flash areas were between 150 km^2

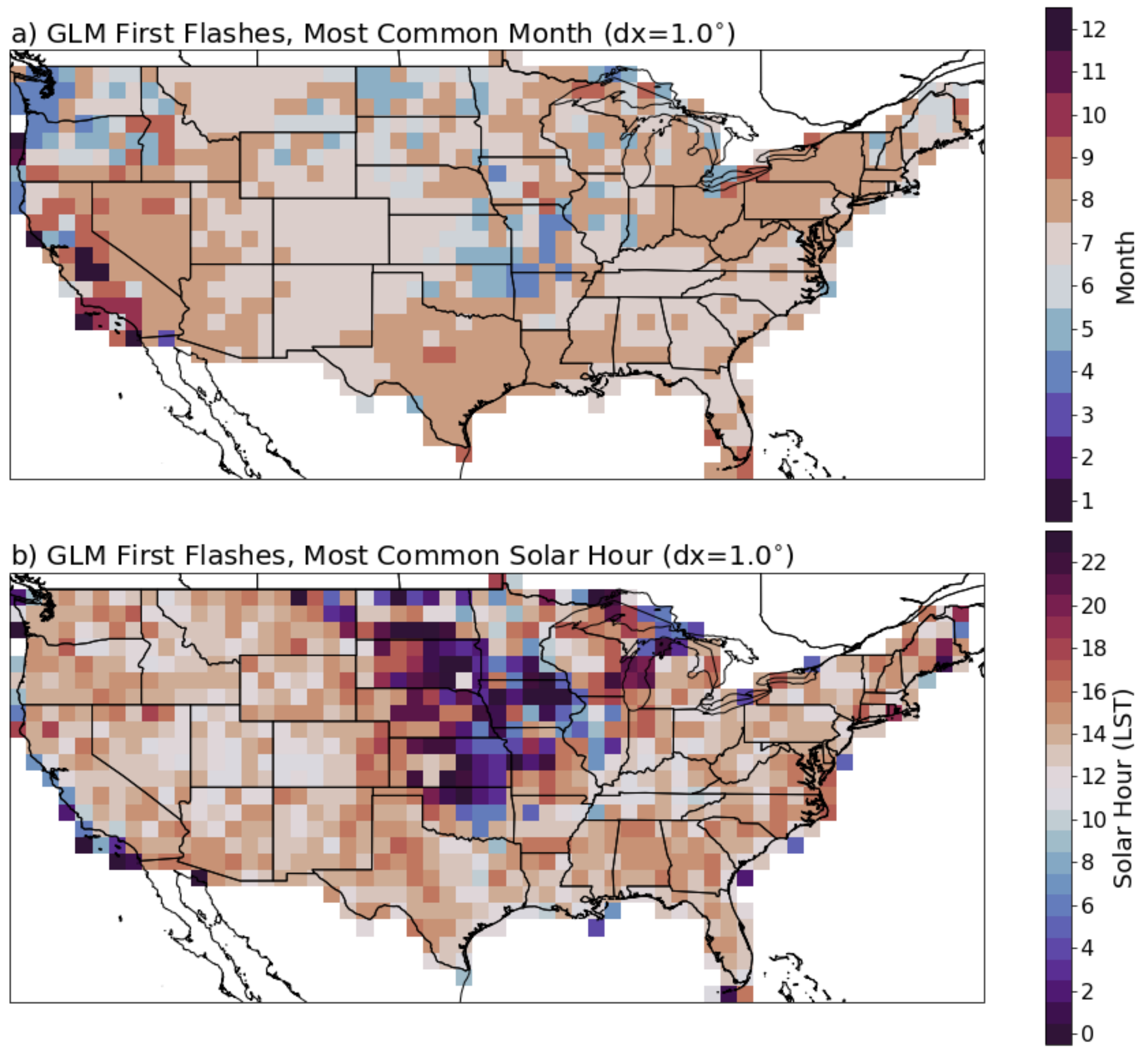

Figure 3.11: The spatial distribution of GLM first flashes from 2022 based on the most common month (a) and local solar time (LST) (b) at horizontal resolution of 1.0 ° latitude and longitude.

and 200 km^2, with larger median areas during the early night (18-23 LST) and late night (0000-0500 LST) segments between 275 km^2 and 400 km^2. Flash energy by season and day segment (Figures 3.12c and d) showed little variability, with median values concentrated between 40 fJ and 110 fJ. Interquartile ranges of flash energy were also consistent between each season and day segment. The duration of first flashes corresponded with the observed trends in flash area, as median flash durations from the boreal summer and fall months were shorter than the median duration from the winder months. Similarly, the median durations of first flashes were shorter during the day segments than at night. All median flash durations across all seasons and day segments were between 50 ms and 150 ms.

Corresponding radar and satellite data from the MRMS system and ABI were collected with each GLM first flash, and binned the recorded values by season in 2022 (Figure 3.13). MRMS composite reflectivity distributions were similar across each season, with all median values between 36 and 38 dBZ and interquartile ranges between 40 and 51 dBZ. Similarly, distributions of isothermal reflectivity had similar medians across all seasons between 36 and 41 dBZ. Reflectivity distributions in Figure 3.13b showed greater values in the boreal summer and fall seasons, with the lowest value and interquartile range recorded during the winter season. Seasonal distributions of ABI cloud-top height contained median values between 9 and 10.5 km, with interquartile ranges between 8 and 11 km. The greatest cloud-top heights across all points in the distributions were recorded during the boreal summer season, and conversely the boreal winter season contained the lowest cloud-top heights. Similarly, ABI cloud-top T_B distributions showed differences in their seasonal distributions. Median values across all seasons were between 224 and 235 K, with all interquartile ranges between 218 and

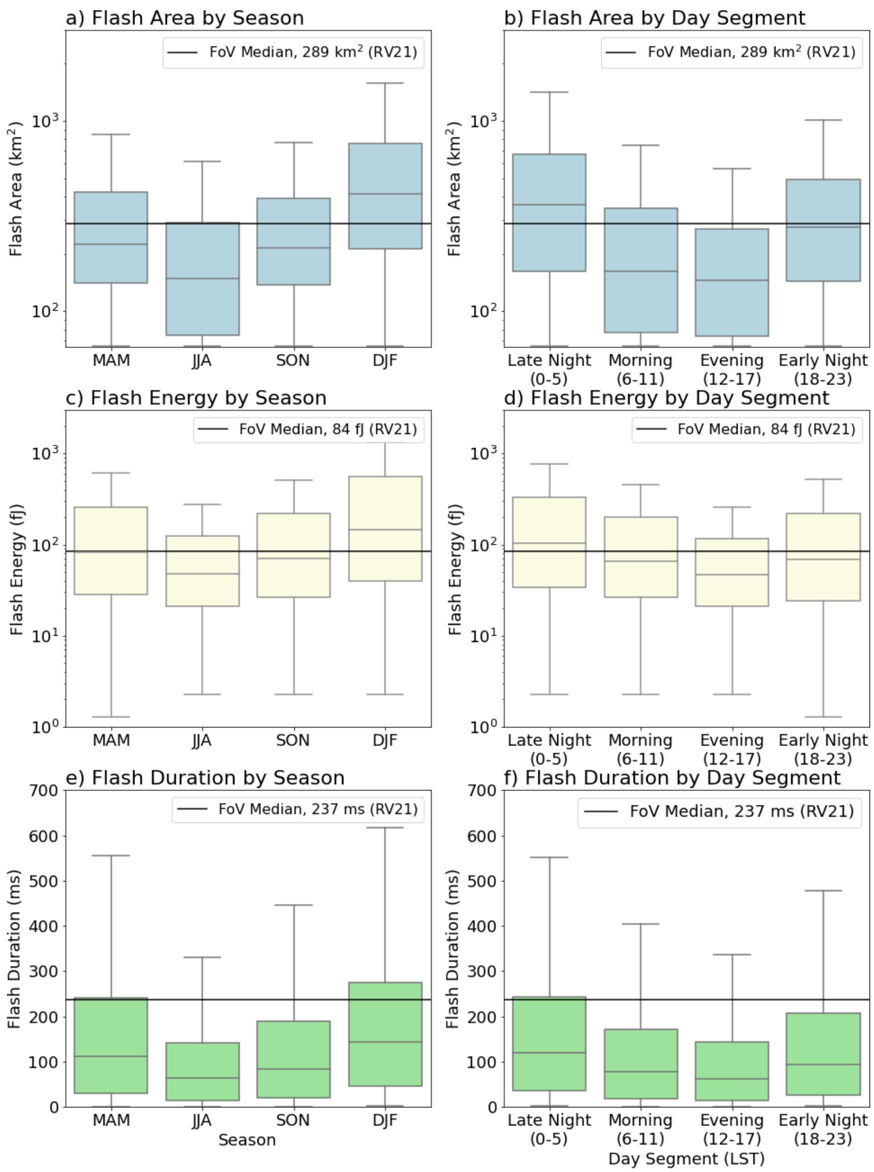

Figure 3.12: Distributions of GLM first flashes and their lightning flash characteristics from the GLM by season (MAM, JJA, SON, and DJF) and by LST day segment (Late Night: 00-05 LST, Morning: 6-11 LST, Evening: 12-17 LST, and Early Night: 18-23 LST). Box and whisker plots of flash area (a and b), flash optical energy (c and d), and flash duration (e and f). Median values from the GLM field of view (FoV) reported by Rudlosky and Virts (2021) (RV21) are annotated for reference.

242 K. The coldest brightness temperature distribution was notably during the winter season, with the warmest distribution in the fall.

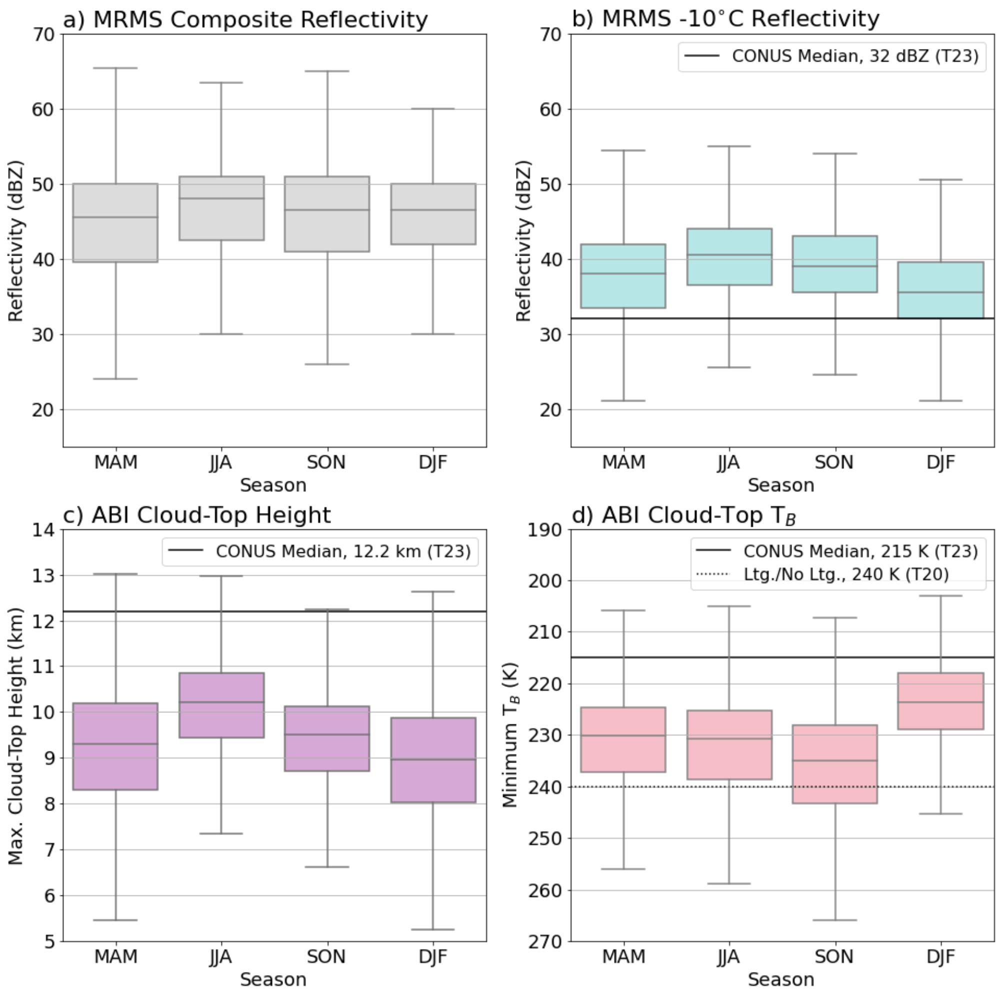

Figure 3.13: Box and whisker plots of maximum MRMS Composite Reflectivity (a), MRMS -10 °C Isothermal Reflectivity (b), ABI Cloud-Top Height (c), and ABI Clean-IR Cloud-Top Brightness Temperature (d) within a 20 km range of GLM first flashes, binned by season in 2022. Median values from Thiel et al. (2023) (T23) and a conclusion from Thiel et al. (2020) (T20) are annotated for reference.

3.5.4 Regional Characteristics

Temporal and spatial distributions of GLM first flashes from Figures 3.10 and 3.11 showed three regions of the United States with distinctive patterns. The Southwest, Great Plains, and Southeast regions as defined previously were separated to investigate their temporal distributions of developing convection through first flashes in Figure 3.14. While the Great Plains region is the largest by area (1.5 million sq km) when compared to the Southwest (1.1 million sq km) and Southeast (0.8 million sq km) (Bureau 2021), it had the lowest number of first flashes in 2022 with 22,751. The Southwest and Southeast regions recorded 40,842 and 30,798 flashes respectively. This resulted in first flash per km^2 values of 0.015 for the Great Plains, 0.037 for the Southwest, and 0.038 for the Southeast.

On a monthly basis (Figures 3.14d, e, and f) all three regions recorded the most developing convection in July with August coming in second. However, the number of first flashes recorded in these months, and in comparison to other months of the year, varied based upon their region. In the Southwest region the number of flashes quickly rose between the months of May July, from over one-thousand to over 12-thousand flashes and coincided with the onset of the summertime monsoon. Increasing instances of developing convection were also observed in the Great Plains and Southeast regions prior to the July maximum. Lower rates were observed when compared to the Southwest region, especially in the Great Plains with a July maximum of just over four-thousand first flashes.

Hourly distributions from each region based on the Local Solar Time (Figures 3.14g, h, and i) broadly matched the distribution presented in Figure 3.10c, with the maximum number of first flashes observed between 1200 LST and 1600 LST. The Southwest and Southeast regions peaked in recorded first flashes at 1300 LST, while the Great Plains region peaked later at 1500 LST. Both the Southwest and Southeast regions have a single peak in the hourly number first flashes, while the Great Plains region has a secondary peak during the overnight hours at 2200 LST. The number of first flashes recorded overnight in the Great Plains region is often greater than the amount recorded in the other two regions, and presents a more evenly distributed temporal frequency of first flashes.

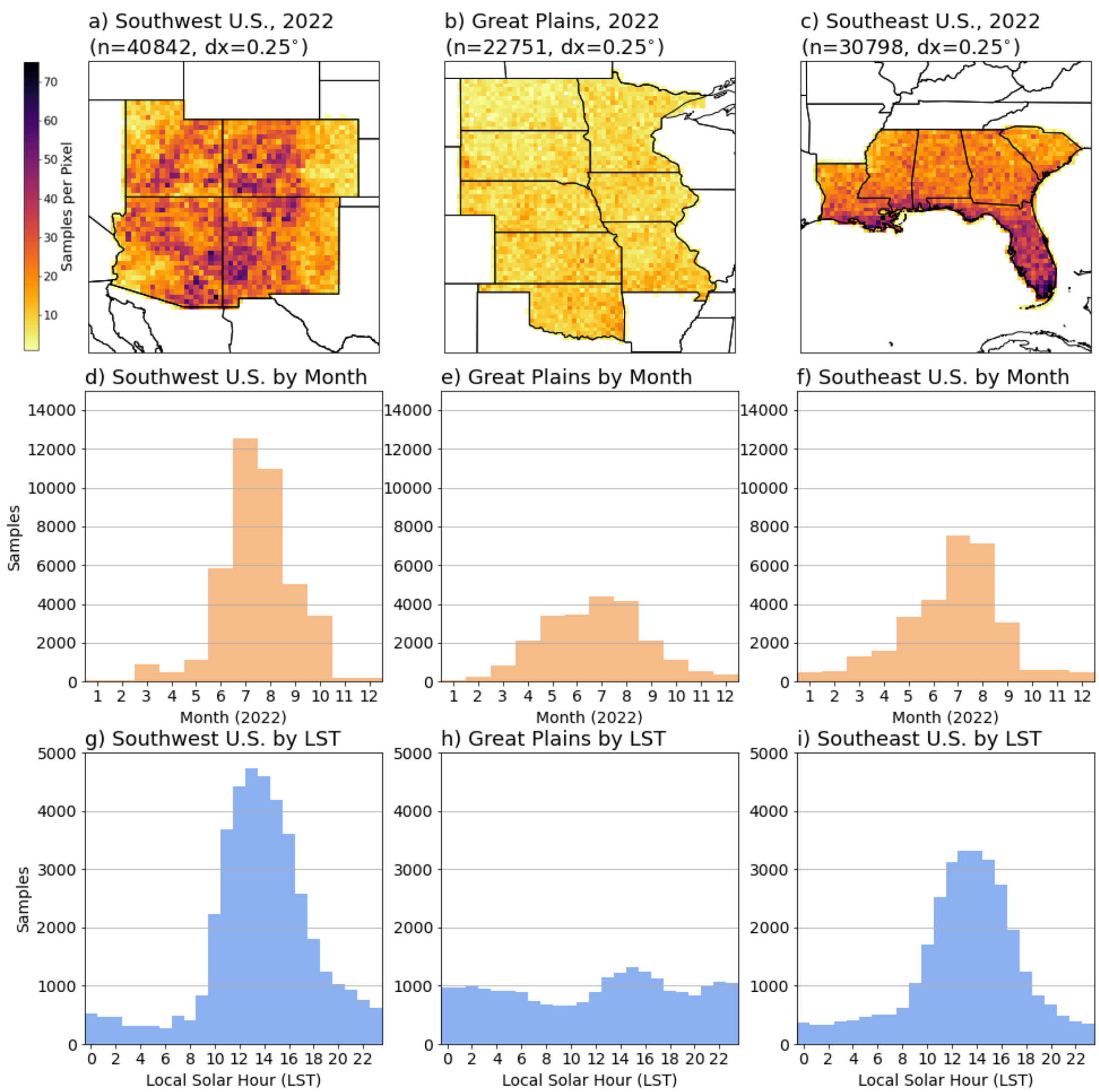

Figure 3.14: Similar to Figure 3.10, except the recorded first flashes are divided by region to represent the Southwest U.S. (a, d, and g), Central Plains (b, e, and h), and Southeast U.S. (c, f, and i).

3.5.5 IC-CG Classifications

After matching ENI flashes with the recorded GLM first flashes from 2022, their classification as intra-cloud (IC) and cloud-to-ground (CG) by ENI were used to calculate the percent difference between these two flash types in Figure 3.15a. Overall the ratio of IC to CG flashes was approximately 1.60, leading to a percent difference between IC and CG flashes of 23%. Across nearly all of the CONUS, the matched ENI first flashes were predominantly IC flashes. This was especially true in the High Plains region of western Kansas, western Nebraska, eastern Colorado, and the panhandles of Oklahoma and Texas with percent differences exceeding 50%. Another region east of the Appalachian Mountains, extending from Virginia to Florida, also contained percent differences of 50% or more. Percent differences were closer to 0%, meaning the proportion of IC to CG flashes were nearly even, in the southwestern United States along with the lower Mississippi Valley regions. Isolated regions, often near the edge of the United States, contained negative IC-CG percent differences, meaning the ENI-matched first flashes favored CG flashes over IC flashes. These regions included far western Texas, the Pacific Coast from Central California to Washington, and along the Canadian border from North Dakota to Minnesota.

For additional context of the ENI-matched first flashes and their IC-CG classifications, the percent of ENI matches with respect to the recorded GLM first flashes were also recorded and plotted spatially over the CONUS in Figure 3.15b. Overall, 73% of the 170-thousand GLM first flashes could be matched with an ENI lightning flash. Matching percentages frequently exceeded 80% and 90% across the Central and Southern Plains region, along with a vast majority of United States east of the Mississippi River Valley. In the Inter-Mountain West, a majority of matching percentages exceed 60%, with a region from central Wyoming to northern Arizona often exceeding 70%. The lowest matching percentages were found in central and northern California with values between 20% and 60%, along with northern Minnesota and northern Maine both containing values as low as 20% to 30% near the Canadian border. Another small region with lower matching percentages was identified in eastern Louisiana and southern Mississippi.

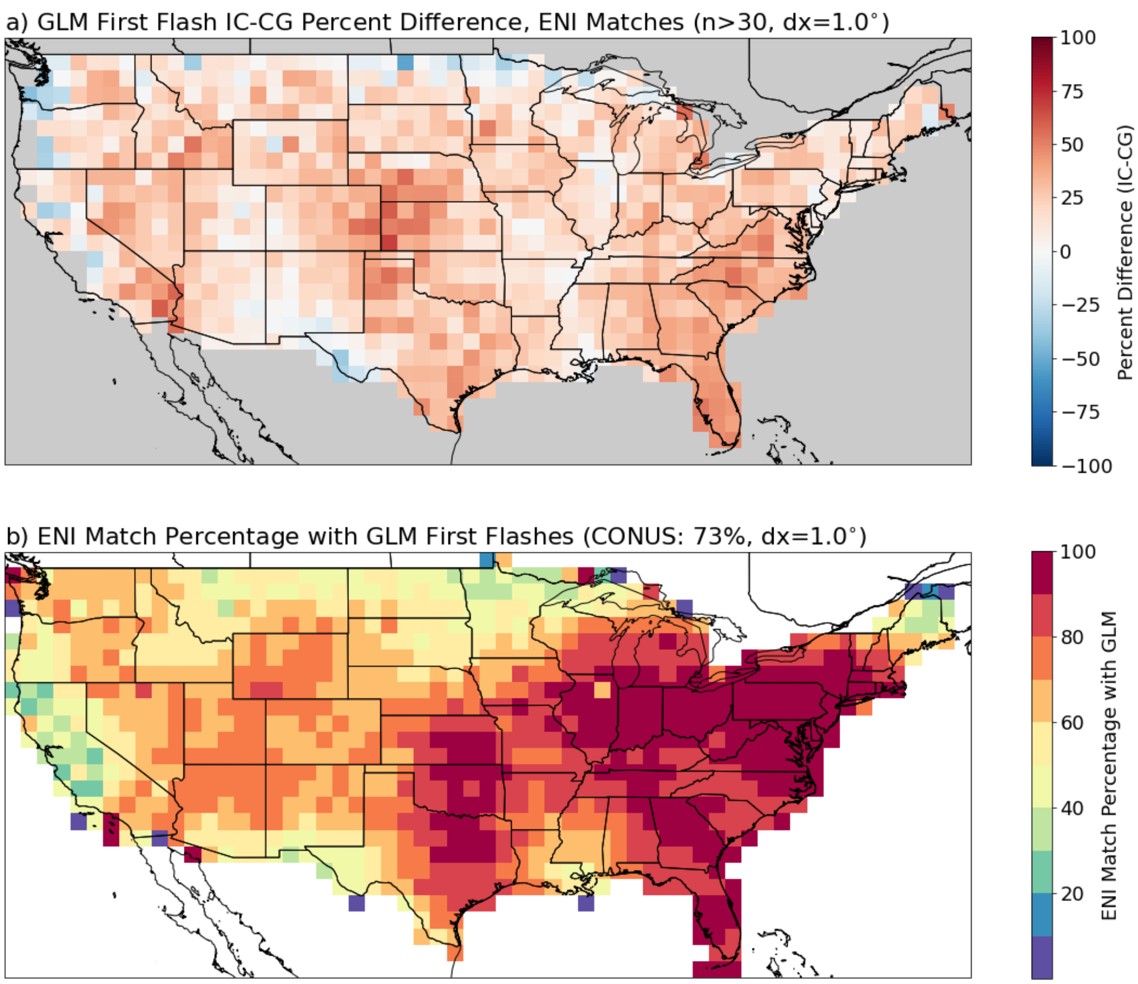

Figure 3.15: (a) A spatial percent difference map between the IC and CG flashes from ENI that were matched with GLM first flashes in 2022. Positive percent differences (reds) favor more IC flashes, and negative values (blues) favor more CG flashes. Any 1° latitude by 1° longitude bin with thirty or less samples was excluded and colored gray. (b) A map of the fraction of ENI flashes that were matched with GLM first flashes, represented as a percentage, in 2022.

In comparison to the ENI-matched first flashes from Figure 3.15a, the IC-CG classifications from the RRF model (Figure 3.16a) showed considerable spatial differences in IC and CG flash occurrence from GLM first flashes. The IC to CG ratio of first flashes classified by the RRF model was approximately 1.87, with a percent difference of 30%. Of the ENI flashes that matched with the GLM first flashes in the study, 73% of the RRF model classifications had the same classification as ENI. The greatest percent difference values were recorded in the Northern Great Plains, the northwestern United States, and southern California with values readily exceeding 50%. Flash classifications also consistently favored IC flashes in the southwestern United States with values between 30% and 60%. Isolated regions of negative values favoring CG flashes by the RRF model were identified from Minnesota to Missouri, western North Dakota to northeast Colorado, and central Maine. Spatial discontinuities in RRF classifications were revealed at 37 °N, with a greater number of flashes classified as IC south of the line and notably fewer IC flashes north of the line. Another region with sudden changes between positive and negative percent difference values was found in the Northern Plains around the region that strongly favors IC flashes.

First flash IC and CG classifications from ENI and the RRF model were combined in Figure 3.16b by filling all GLM first flashes that did not have a ENI-matched flash with the RRF model classifications. In the merged dataset, the greatest percent difference values were in the high plains region similar to the values observed in Figure 3.15a and in the northwestern United States similar to Figure 3.16a. Percent difference values were consistently negative and favoring CG flashes in the southwestern United States from southern California to western Colorado and eastern New Mexico. Based on the reported values from Figure 3.15a in this region, the RRF model contributed a substantial number of CG classifications to the unmatched first flashes. Lastly the southeastern United States, similar to Figures 3.15a and 3.16a, consistently favored IC flashes.

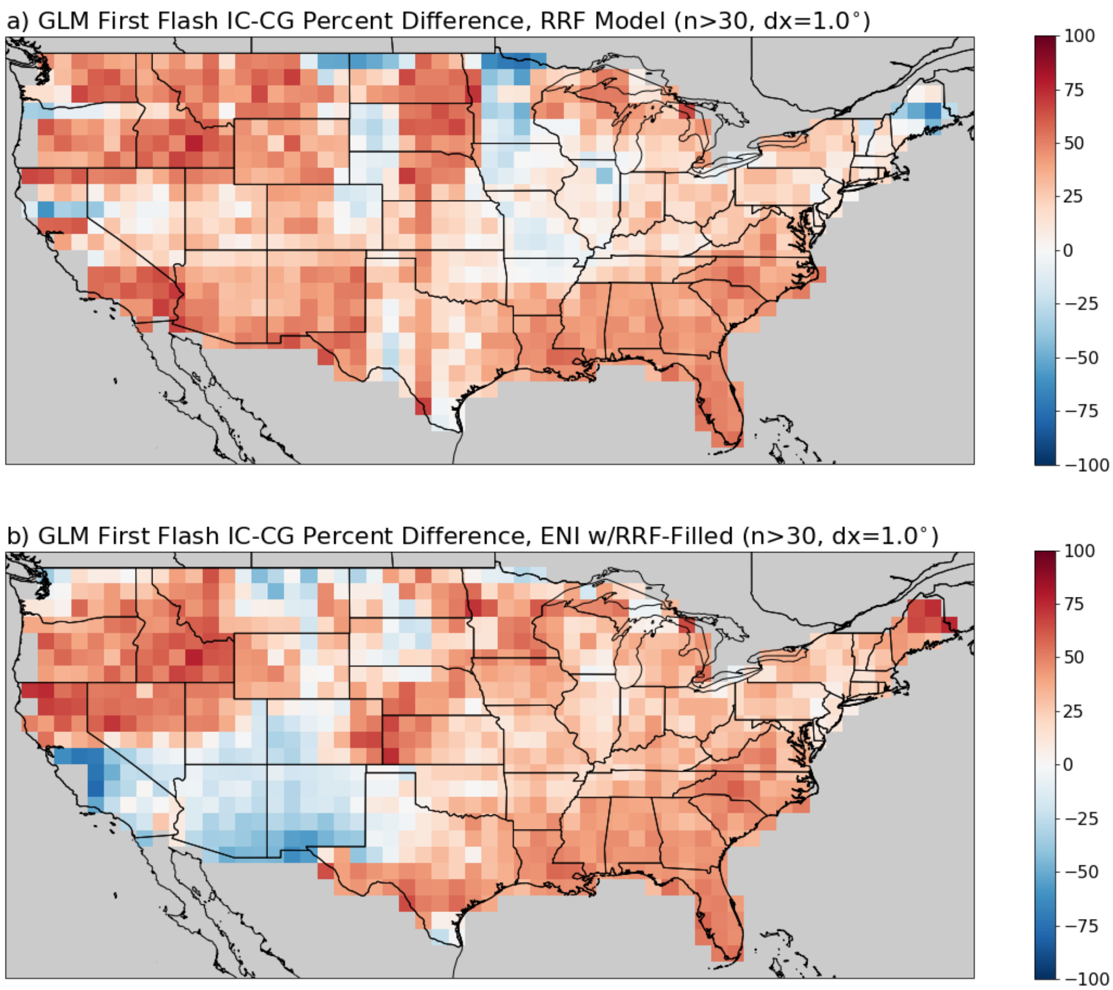

Figure 3.16: Similar to Figure 3.15a except (a) the GLM first flashes were classified by the RRF model using only the GLM flash characteristics, and (b) a combination of the ENI and RRF classifications where the first flashes were classified first by the ENI matches while the remaining 27% were classified by the RRF model.

3.6 Discussion

3.6.1 GLM Characteristics of First Flashes

GLM-observed first flash characteristics help to characterize the associated convection, especially with respect to flash area and duration. Rudlosky and Virts (2021) observed GLM16 and GLM17 flashes over both sensors field of view from 1 December 2018 to 31 May 2020. The GLM16 median values from this study were annotated in Figure 3.12 for additional context with these distributions. While Rudlosky and Virts (2021) showed that GLM flashes on land were on average smaller in area, shorter in duration, and brighter in optical energy than flashes over the ocean, the median value provides a meaningful points of reference. The median values of flash areas and durations were notably reduced when compared to the median values from Rudlosky and Virts (2021). Median flash areas were often one to two GLM pixels smaller during the daytime hours and warmer months of the year between March and November. Similarly, median flash durations were often 100 to 150 ms shorter during all seasons day segments. The propagation of lightning flashes are sustained by sufficient electric potential between regions of charge (Bruning and MacGorman 2013), therefore the area and duration of a thunderstorms first lightning flash can provide insight into the thunderstorms sampled within the study. During maxima in convective instability, such as warm season months and during the daytime, flash areas and duration were notably smaller indicating more vigorous updrafts which will increase charge separation in the mixed phase region and create smaller regions of resultant charge Bruning and MacGorman (2013); Calhoun et al. (2014). This is supported by the individual flashes studied from the OK-LMA and NSSL LMA domains (Figures 3.2 and 3.3), relating the development of their parent thunderstorms to their resultant durations and flash footprints.

Classifying first flashes as IC or CG allows direct applications for lightning safety, and the ability to infer the charge structure characteristics of the developing convective cloud. The ratio of IC to CG flashes from ENI-matched first flashes was 1.60 while the RRF model of GLM flashes was slightly greater at 1.87. In comparison, (Boccippio et al. 2001) used four years of total lightning observations from the Optical Transient Detector and National Lightning Detection Network to estimate a higher IC to CG ratio of 2.64 to 2.94 over the CONUS and a standard deviation of 1.1 to 1.3. Greater IC to CG ratios were observed in the central high plains in Figure 3.15 and by Boccippio et al. (2001), with lower values in the southwestern United States. Approximately 73% of all GLM first flashes had a matching ENI flash, however this matching fraction had considerable spatial variations (Figure 3.15b). Regions with matching fractions below 60% included the southern and northern borders of the CONUS, along with much of the west coast, eastern Louisiana, and Maine. In these regions the lower IC-CG scaled differences may be influenced by the matching criteria in regions with lower GLM detection efficiencies (Murphy and Said 2020; Bateman et al. 2021), and that the GLM is more likely to observe CG flashes than IC flashes due to their increased group area (Zhang and Cummins 2020). Another potential influence is the ENI network configuration and the detection efficiency respective to IC and CG flashes, where regions with lower ENI sensitivity may be less likely to observe lower amplitude IC pulses (Cummins and Murphy 2009). However, CONUS-wide detection efficiency maps from ENI are unavailable for this study and therefore these impacts cannot be defined explicitly.

Cross validation against the ENI-matched first flashes was conducted by using the RRF model as described in Ringhausen et al. (2021). While the RRF classification matches in 73% of the ENI-matched first flashes, the scaled IC-CG differences showed little similarities between Figures 3.16a and 3.15a. The increased proportion of IC classifications suggests that most of the unmatched-ENI flashes are also IC flashes, and may be subject to ENI detection efficiencies as previously described. On the other hand, spatial discontinuities in the proportion of IC and CG flashes injects uncertainty into the RRF model classifications. A feature analysis of the RRF in Ringhausen et al. (2021) showed that spatial variables held the most weight in the classifications such as maximum group area, maximum distance between groups, and maximum distance between events, with larger values trending towards CG flashes. Time of day also held an elevated importance with a larger proportion of CG flashes occurring during the daytime hours. When using the RRF model to fill the first flashes that couldn't be matched with ENI, large contributions of CG flashes from the RRF model were observed in the southwestern United States while many locations along the northern and southern CONUS border increased in the proportion of IC first flashes. In the southwestern United States the increased elevation, and resultant lower freezing levels may partially explain the increased proportion of CG first flashes. Boccippio et al. (2001) observed a qualitative trend in decreasing IC-CG ratios with increasing elevation. Meanwhile Fuchs et al. (2015) studied the impact of environmental controls on charge separation and resultant lightning activity within four LMA domains across the central and eastern CONUS. Elevated cloud bases, or a disproportionate ratio of precipitation above the freezing level, can limit the development of a lower positively charged region cased by melting hydrometeors and alter the distribution of IC and CG flashes from a thunderstorm. First flashes may have an increased likelihood of being CG flashes in this region, however additional studies using LMAs in the region would be necessary to confirm this impact on the charge structure in developing convection and resultant first flash type between IC and CG flashes.

One important consideration when interpreting RRF model classifications in the presented study is the use of GOES-17 GLM first flashes west of 103 °W. The RRF model was trained only on flashes from the GOES-16 GLM, but the training dataset did not contain geospatial reference data (e.g. latitude and longitude). Differences in flash characteristics from the GLMs in the GOES-East and GOES-West positions were observed by Rudlosky and Virts (2021) across the CONUS, in individual storms by Thiel et al. (2023), and an individual flash in Figure 3.2. These differences are driven by spatial variations in GLM group detection thresholds as discussed Cummins (2020). This effect was observed in Figure 3.2, where the lower sensitivity of GLM17 recorded fewer, and smaller, GLM groups resulting in a reduced flash footprint. The weight of spatial flash variables in the RRF model, timing of observed first flashes from Figure 3.14g, and increased sensitivity of GLM17 may lead to a larger proportion of CG flashes. Lastly, the presented study focuses only on the first lightning flash from developing convection, and uses the GLM to observe the first lightning flash. Missed GLM flash detections of first flashes were observed in approximately two-fifths of manually verified cases with respect to ENI flashes, and may bias the GLM towards the more luminous CG flashes.

3.6.2 ABI and MRMS Characteristics

Sampled MRMS reflectivity and ABI cloud-top characteristics demonstrated the type of convection associated with GLM first flashes. Elevated MRMS composite reflectivity values exceeding 40 dBZ in all seasons (Figure 3.13a) suggested that convective updrafts with increased hydrometeor size and density were within 20 km of a large portion of the recorded first flashes. This was supported by the isothermal reflectivity distributions in Figure 3.13b, where all 25th percentile values for all seasons exceed 30 dBZ. From the study conducted in Chapter 2 (also referred to as Thiel et al. (2023)), the median isothermal reflectivity value was 32 dBZ, which was still at or below the 25th percentile of the presented distributions in Figure 3.13b. In two summertime cases of thunderstorm electrification and first lightning flashes in New Mexico, Stolzenburg et al. (2015) observed the presence of a 40 dBZ echo exceeding the -10 °C isotherm shortly before electric fields at the surface increased, signaling the onset of localized, non-inductive charge separation. During the boreal summer and fall months isothermal reflectivities increased, suggesting increased convective instability and the ability of developing updrafts to loft hydrometeors into the mixed phase region to support charge separation (Emersic and Saunders 2010). Mecikalski and Carey (2018) demonstrated that lightning flashes in single cell and multi-cell thunderstorms from the southeastern United States typically initiate in reflectivity regions between 30 and 40 dBZ. This study used a three-dimensional reflectivity field, however the corroborating distributions in Figure 3.13b demonstrate that the sampled convection near first flashes should also coincide with lightning activity.

While the MRMS reflectivity values signal the presence of deep convection, the corresponding ABI cloud-top heights and brightness temperatures provide another perspective. Cloud-top heights across all seasons in Figure 3.13c were considerably lower than the median from Thiel et al. (2023) of 12.2 km, with most inter-quartile ranges between 8 and 11 km. Similarly, brightness temperatures were notably warmer than the median of 215 K from Thiel et al. (2023) with all inter-quartile ranges between 215 and 245 K and median values between 224 and 235 K. Thiel et al. (2020) provided a similar study to Thiel et al. (2023) across the same GOES-East ABI domain for only ABI and gridded GLM imagery. When comparing the sampled Clean-IR T_B that did and did not coincide with GLM flashes, the 240 K value was found to be a favorable discriminator between regions associated with lightning activity and those with no activity. The interquartile ranges in Figure 3.13d were between 212 and 240 K, and when combined with the decreased ABI cloud-top heights, signal that weak or developing convection was observed for a substantial portion of the study.

Another way to view the ABI and MRMS distributions, and compare them to previous results, is through two-dimensional histograms with the same bins and formatting as shown in Thiel et al. (2020) and Thiel et al. (2023) (Figure 2.6a). The joint distributions in Figure 3.17 show a shift in the peak of the sampled distribution to lower cloud top heights, warmer cloud-top T_B, and greater isothermal reflectivity. While this suggests that the present study is sampling comparatively weaker convection from the perspective of the ABI, it remains established that the samples are provided by convective updrafts based on the MRMS composite isothermal reflectivity distributions. This however does not mean that all first flashes were observed within the study, as reflected by POD values of the selected criteria of 30-40% in Figure 3.9. The presented study may bias against semi-discrete updrafts which develop in close proximity – less than 20 km – from ongoing convection. Convective cores and their close proximity to each other made classification more difficult when manually analyzing candidate first flashes, and contributed to lower confidence values in Figure 3.7)a. However, this expense comes with the benefit of reduced false classifications of first flashes for larger flashes through stratiform precipitation and those impacted by geolocation errors as observed in Figure 3.6. Flashes propagating through larger, stratified layers of charge were identified in Figure 2.6c between brightness temperatures of 210 to 230 K, and isothermal reflectivity values between 20 and 30 dBZ. When compared to Figure 3.17b, few first flashes were observed in this range, with peaks between 220 to 240 K and 30 to 50 dBZ.

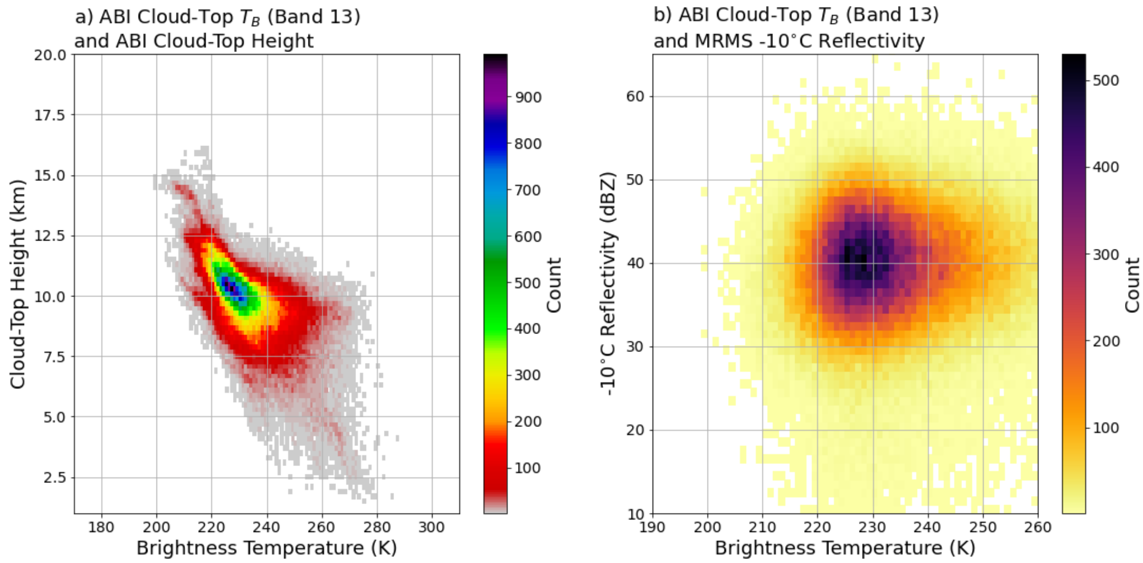

Figure 3.17: ABI and MRMS distributions from all GLM first flashes in 2022 (n=167421) by ABI Cloud-Top T_B and ABI Cloud-Top Height (a) similar to Figure 2a from Thiel et al. (2020), and by ABI Cloud-Top T_B and MRMS -10 °C Isothermal Reflectivity (b) similar to Figure 2.6a. Panel a is binned every 1 K and 200 m, and panel b is binned every 1 K and 1 dBZ.

3.6.3 Regional Influences of Thunderstorm Development

3.6.3.1 Southwestern Region

In the Southwestern region from Figure 3.14, first flash densities are more scattered and tied to regions of elevated terrain, similar to what was observed by DiGangi et al. (2022). These instances of developing convection often occurred during peak solar insolation and the boreal summer, coinciding with the annual North American Monsoon (NAM) (Higgins et al. 1999). Onset of the NAM typically begins in early June across southern Mexico and progresses northward into the Southwestern U.S. by early July, bringing additional moisture, heavy rainfall, and increasing thunderstorm activity to the region. A review of the 2022 NAM by NWS Phoenix (2023) revealed an early onset of monsoon activity to the Southwestern U.S. by the middle of June, leading to the ninth wettest monsoon season on record. The 2022 NAM was also characterized as the fourth warmest with record moisture values as indicated by precipitable water from June through September across the region. The increase first flashes in the Southwestern U.S. from May to June in Figure 3.14d represents the increasing convection developing in a region with elevated convective instability and tropospheric moisture to support convective development. This was especially true in regions with orographically-forced convection (Kirshbaum et al. 2018) which can occur during peak daytime insolation (Figure 3.14g). Inter-annual variability of the NAM may contribute to the number of semi-discrete thunderstorms, and therefore first flashes, within the analysis. However, additional first flash studies from other monsoon seasons within the region may provide additional utility to help characterize regional precipitation patterns in the Southwestern U.S. and other more remote regions.

3.6.3.2 Great Plains Region

The most common solar hour of first flashes from the Great Plains in Figure 3.11b featured overnight hours between 2000 LST and 0600 LST, which was a departure from the rest of the CONUS which most often observed first flashes during the daytime hours from 1100 LST to 1800 LST. First flash spatial densities from Figure 3.14 were reduced in the Great Plains region when compared to the Southwestern and Southeastern regions, making each spatial bin more sensitive to noise. However, the large geographic spread of overnight values in the Great Plains suggests meteorological influences driving convective development during the overnight hours. DiGangi et al. (2022) created a thunder-hour climatology from January 2015 to December 2019 with data from the Earth Networks Global Lightning Network. Over the Great Plains region used in the presented study, DiGangi et al. (2022) reported a peak probability in thunder-hour occurrence during the overnight hours from 2200 LST to 0600 LST. This feature was most pronounced during the boreal summer and fall seasons. Taszarek et al. (2020) provided similar results when compiling a 40-year lightning climatology from 1979 to 2018 with data from the National Lightning Detection Network. The 'Midwest' region used by Taszarek et al. (2020) most closely matches the Great Plains region of the presented study, and hourly distributions peaked at approximately 2300 UTC and remained elevated into the overnight hours. Hourly distributions of first flashes from the Great Plains region in Figure 3.14h presented a localized peak around 2000 LST to 2200 LST, with the primary maxima between 1400 LST to 1600 LST.

While the studies from DiGangi et al. (2022) and Taszarek et al. (2020) focus on total lightning flash occurrence, rather than the first lightning flash, the overlapping spatial patterns reinforce the development and maintenance of convection overnight in the Great Plains region. Shield and Houston (2024) noted the frequency of DCI in the central United States and the increased contribution of nocturnal forcing within its analysis. When studying nocturnal DCI events from Reif and Bluestein (2017), a majority of events were related to the development of linear convection. These events were frequently associated with outflow boundaries in the early overnight hours, and no boundaries in the later overnight hours respectively. One supporting factor is the development of supergeostrophic winds above the nocturnal boundary layer and the sloping terrain of the Great Plains, which are conducive to nocturnal low-level jets across the region (Blackadar 1957; Bonner 1968; Stensrud 1996). Low-level jets can support the development of deep convection, especially when superimposed with upper-level atmospheric jets (Uccellini and Johnson 1979). Another prominent feature of the Great Plains region is the increased frequency of Mesoscale Convective Systems (MCSs) (Parker and Johnson 2000; Houze 2004), which were also noted by Taszarek et al. (2020) and DiGangi et al. (2022) during the summertime months in their respective thunder-hour climatologies. Convectively-generated cold pools, when aided by the lower level jet, allow MCSs to persist for up to five hours or longer (Coniglio et al. 2010). GLM flashes with large areal extents within the stratiform precipitation regions of these MCSs may be incorrectly classified as first flashes in the Great Plains region. However, the addition of flash area radius in addition to the standard 20 km spatial buffer provided decreased false detections compared to the criteria without the flash area radius.

3.6.3.3 Southeastern Region

Among the three regions defined in Figure 3.14, the Southeastern U.S. region had the highest density of first flashes in 2022 with nearly all areas containing over thirty samples. First flashes most often occurred over the boreal summer during, and slightly after, the period of daily peak insolation. Along the coast of the Gulf of Mexico and the Atlantic Ocean, the most common solar hours were from 1200 to 1400 LST (Figure 3.11b). Afternoon sea breezes during synoptically quiescent periods of the boreal summer can act as a localized source of lift for thunderstorms (Hsu 1970), which were most prominent over the Florida peninsula with sea breezes from its eastern and western coasts (Byers and Rodebush 1948; Hodanish et al. 1997). Similar spatial and temporal thunder-hour observations were made by DiGangi et al. (2022) and Taszarek et al. (2020), reinforcing the role of land-sea interactions with thunderstorm development. Further inland, the most common solar hours were later - between 1400 and 1700 LST, indicating the need for increased daytime heating before convection could develop in the absence of localized forcing from land-sea interactions.

3.6.3.4 Anomalous First Flashes

One unusual feature from the observed first flash spatial densities featured in Figure 3.10a was a compact region with increased densities in northern Illinois and west of the Chicago metropolitan area. Closer inspection of these flashes spatially revealed dense, tightly packed first flash locations localized to approximately the size of four GLM pixels (Figure 3.18). When sampling the flashes in this area and comparing them to those around it, the flashes in this dense region were considerably smaller in area and had lower optical energies. These flashes were also most frequent during the afternoon hours of 1400-1600 LST and the month of December, while the flashes around had temporal frequencies similar to the Great Plains region. Plotted examples of first flash occurrences (not shown) showed GLM flash detections in regions with no MRMS reflectivity or cloud cover. All of these findings suggest that the first flashes in this compact area were from false GLM detections. Solar glint from natural and manufactured reflective surfaces such as solar electricity farms, lakes, and rivers may contribute to these false detections, and their lack of associated convection may make them more likely to be collected by the objective algorithm employed for this study. Similar to Chapter 2, additional filtering with corroborating satellite and radar observations may be needed to further improve these datasets and identify more regions with unknown false GLM detections.

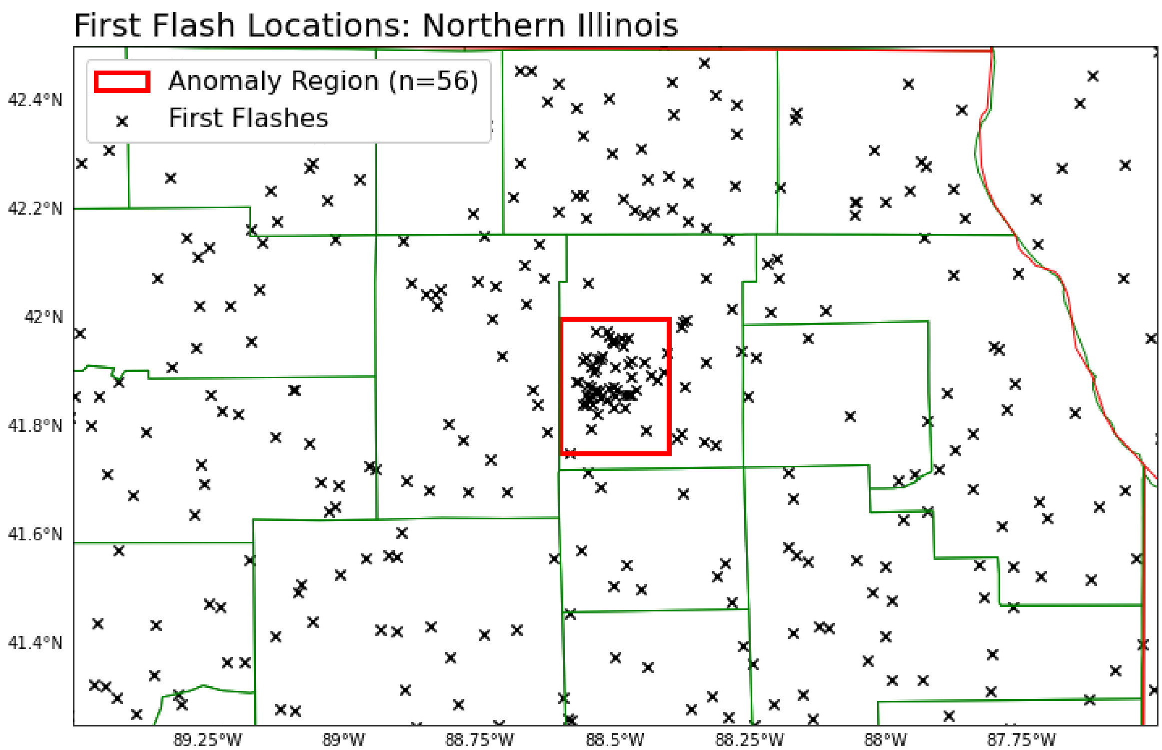

Figure 3.18: A scatter plot of GLM first flash locations from all of 2022, centered over an area of anomalously frequent first flashes. The red box highlights area of the anomaly.

Chapter 4

Machine Learning Applications for Identifying and Classifying Convection

4.1 Motivation

The work previously established in Chapters 2 and 3 demonstrated how developing and severe convection may be identified by the GLM when used with satellite imagery and radar data. Machine learning methods have been developed more recently as prognostic and diagnostic tools to identify lightning occurrence and the coverage of convection (Hilburn et al. 2021; Lagerquist et al. 2021; Cintineo et al. 2022; Harrison et al. 2022; Ortland et al. 2023), along with assessing the potential for convective hazards (Karstens et al. 2018; Cintineo et al. 2020a,b, 2024). These previous studies focus on a single task, however the multi-faceted utility of integrated GLM, ABI, and MRMS datasets as shown in previous chapters provides the opportunity to develop integrated, multi-tier models that address both of these issues. The development of such a model would also validate these previous observations, trends, and applications with respect to all stages in a thunderstorm's life cycle. This chapter explores the creation of a two-tiered machine learning model, which is expected to identify convection and classify its intensity based upon its lightning activity. The training, validation, and demonstration of both tiers of the model will also be discussed.

4.2 Data and Methods

The same ABI and MRMS variables leveraged in Chapter 3 were used as the observations and predictors for both tiers of the posed machine learning problem. These included composite reflectivity, -10 °C isothermal reflectivity, cloud-top height, and cloud–top T_B. The training and testing datasets were created using the same cases of semi-discrete convection described in Table 3.1. Each domain was gridded every 0.2 ° in latitude and longitude, to provide an approximately 20 km by 20 km grid. The seven cases provided over 640-thousand samples to use for training and testing a machine learning model. The maximum radar variables and cloud-top heights were sampled within each grid point, along with the minimum cloud-top T_B, every five minutes to coincide with the temporal resolution of the ABI CONUS scene. MRMS values were sampled from the most recently available file - every 0th and 6th minute per 10 minute segment - with all other data excluded for this analysis. Additionally, all ABI data were parallax-corrected based on the reported ABI cloud-top height using the SatPy python package (Raspaud et al. 2022) and surface T_B values were excluded using the ABI Clear-Sky Mask. Lastly, lightning flashes from GLM16 were collected in each grid cell and accumulated 20 minutes into the future from each point in time.

Lightning flashes from GLM16 were used to identify convection and create their target classifications of 'strong' or 'weak'. As mentioned previously in Chapter 3, the appearance of lightning has been used to identify deep convective updrafts by Manzato et al. (2022) while machine learning methods have also used satellite imagery to identify regions favorable for lightning production (Cintineo et al. 2022). For the purposes of this study, pixels in the dataset containing at least 1 lightning flash in the next twenty minutes were considered as convection with lightning. Classifying the intensity of convection by its total lightning production has been addressed most commonly through rapid increases in total flash rates prior to severe weather occurrence (Williams et al. 1999; Schultz et al. 2009) along with identifying thunderstorms with exceptional local flash rates (Calhoun et al. 2013; Thiel et al. 2020). To avoid reporting biases and subjective limitations from severe weather reports (Trapp et al. 2006; Potvin et al. 2019) the number of flashes within a single 0.2 ° pixel was used to classify identified convection as 'strong' or 'weak'. Pixels were defined as 'Strong Convection' ('Weak Convection') if they had at least (less than) five GLM flashes in the next 20 minutes. This definition was determined by comparing the distributions of ABI clean-IR T_B and MRMS -10 °C isothermal reflectivity from the compiled testing and training dataset (not shown) against the distributions of all convection and severe convection from Figures 2.6a and 2.7a respectively. Peaks in the distributions of clean-IR T_B and isothermal reflectivity for pixels with at least five GLM flashes shifted to below 220 K and above 35 dBZ, similar those observed in Chapter 2. While five-minute Flash Extent Density values from Figure 2.6b would suggest a value of 10 flashes, this study presents the density of GLM flash centroids. Centroid density values will be comparably less for deep convection which can support persistent charge separation, and therefore increased flash rates, as robust convection frequently exceeds the confines of a single 0.2 ° pixel. Distributions of GLM flash areas from Rudlosky and Virts (2021) also demonstrate the number of flashes that may contain footprints that exceed a single pixel, with mean flash areas over the central and eastern United States frequently exceeding 400 km^2. The reduced spatial information from GLM flash centroids when compared to FED were also noted in HWT product demonstrations (Calhoun 2018, 2019).

Rather than developing two independent machine learning models to address the identification of convection and its strength, a two-tiered model of binary classifications was created such that convection was identified first, followed by the decision of if that convection was weak or strong. Random forests were selected for both tiers (Breiman

2001) based on their ability to train on large datasets with high levels of dimensionality, no scaling or centering required (Géron 2019), and produce consistent probabilities within a class. The first and second tier random forest will be referred to as TRF1 and TRF2, respectively, hereafter. A random forest is a collection of decision trees which divide a dataset into two or more predefined classes using a series of decision nodes (Breiman et al. 1984). Variability of the weaker individual trees, trained on only a subset of the data, are combined to produce a stronger forest. Decision trees themselves are most commonly tuned through the maximum number of leaf nodes resulting from their decision nodes and the maximum depth of the tree, with the random forest commonly tuned by the number of trees within the forest. For the purposes of training and testing each random forest, 80% of the available dataset was randomly selected and used to construct the model with the remaining 20% for testing. Due to the imbalance in each dataset of 'Lightning' to 'No Lightning' pixels and 'Strong Convection' to 'Weak Convection', the proportion of target classes were stratified between the training and testing datasets.

The following two sections will discuss the construction of each random forest and its performance against the testing dataset. An example case from 14 May 2022 - independent from the machine learning training and testing datasets - was created to visualize the probabilistic and deterministic output from each tier of the model. The MRMS, ABI, and GLM data from these cases had the same temporal and spatial resolution as the testing and training datasets, with starting and end times of 14 May 2022 1500 UTC and 15 May 2022 0400 UTC, a latitude range of 34° to 38°, and a longitude range of -95° to -89°. One region of interest centered in Northwestern Arkansas will be discussed, followed by two case studies of thunderstorms near Fayetteville, Arkansas and Mena, Arkansas. Lastly, the MRMS MESH product will also be included in the case study as another indicator of updraft strength and thunderstorm hazards.

4.3 Identifying Convection - TRF1

The first step in building TRF1 was tuning the hyperparameters to the posed machine learning problem. Individual decision trees were created with incremental adjustments to the maximum depth and leaf node parameters, creating a total of 231 unique model configurations. The training and testing datasets were split into 40 folds, yielding 40 decision trees within each model configuration and a total of 9240 trees to evaluate. Each tree was scored based on its $F1$ score (Sasaki 2007) (Equation 4.1). The F1 score is the harmonic mean between a models ability of how to retrieve only relevant items (precision) and how many relevant items are retrieved (recall), with 0 representing the worst performance and 1 representing the best performance.

$$F1 = \frac{2 * a}{2 * a + b + c} \tag{4.1}$$

Each combination in the testing and training datasets received a mean $F1$ score from its 40 folds, and these values were plotted in Figure 4.1. Mean $F1$ values ranged from 0.59 to 1.00 in the training dataset and 0.58 to 0.67 in the testing dataset. These values increased with increasing leaf nodes and depth with respect to the training dataset (Figure 4.1a), especially as the maximum depth increased when there were no restrictions on the maximum number of leaf nodes. Many $F1$ value trends in the in the training dataset were observed in the testing dataset, with exception to the deeper trees with an unlimited number of leaf nodes. In this section of Figure 4.1b mean $F1$ values decreased, suggesting that a deep random forest with an unlimited number of leaf nodes was overfitting to the training dataset. With only four predictors and the concern for overfitting, trees with a maximum depth of five and a maximum of 20 leaf nodes selected as the 'optimal' decision tree to leverage within the random forest.

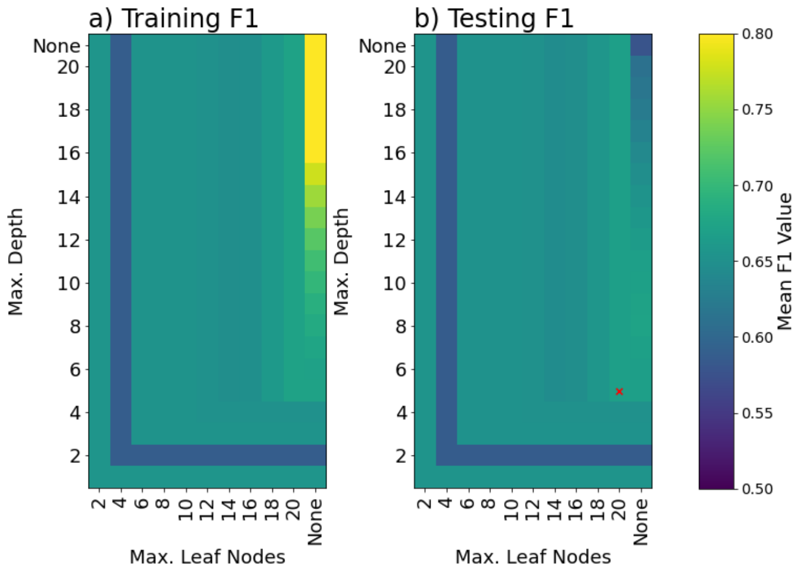

Figure 4.1: Mean F1 values of decision trees (40 stratified folds) with respect to its maximum leaf nodes and maximum depth with respect to the training (a) and testing (b) datasets. The red 'x' in panel b represents the selected tree employed for the random forest.

Plotting the optimal decision tree in Figure 4.2 showed the distribution of decisions and thresholds between the regions that did and did not produce lightning, with -10 °C isothermal reflectivity frequently used, followed by both ABI variables. Gini impurity values (Géron 2019), which demonstrate the ratio of false positive or true negative events within each node, range from 0.008 to 0.499 across the tree. This distribution reflected the continuum of skill in the decision tree to discriminate between these regions. Next, combinations of maximum depth, maximum leaf nodes, and the number of decision trees were used in a similar format to tune the hyperparameters of TRF1. Mean F1 values showed similar trends from Figure 4.1 with respect to the maximum leaf nodes and maximum depth. Little to no variations were noted in the number of decision trees used by the random forest. however it was noted that when using beyond 100 decision trees model training and probabilistic output became computationally more expensive. Therefore, 100 decision trees were selected to make up TRF1.

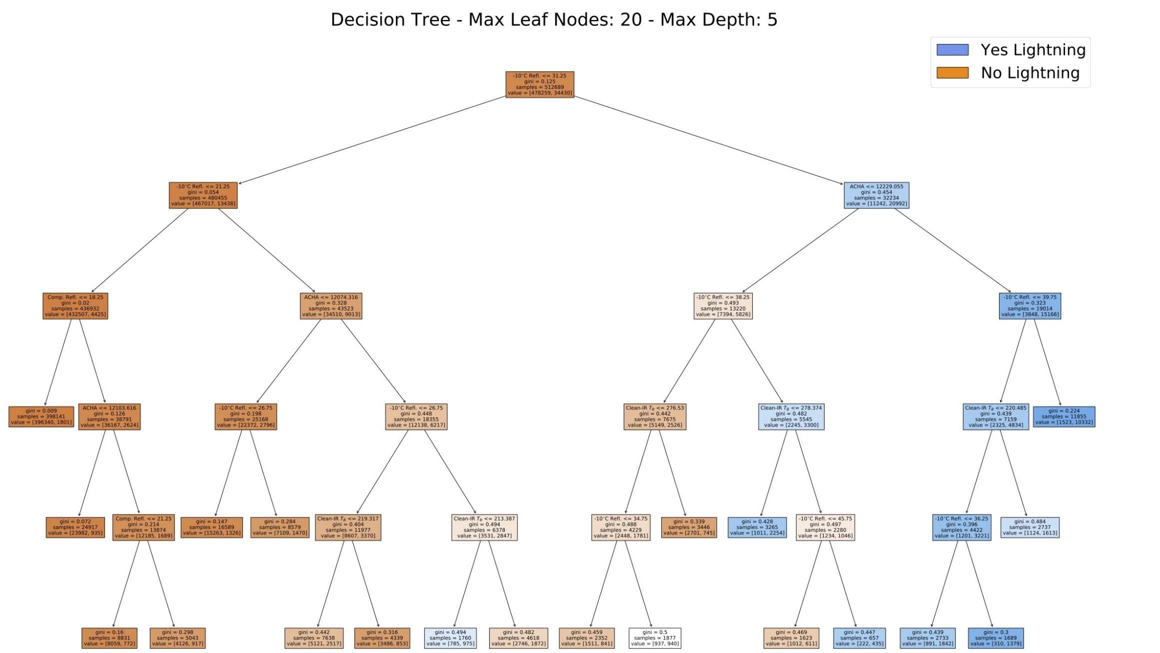

Figure 4.2: A decision tree with the 'optimal' maximum leaf nodes (20) and maximum depth (5). Orange nodes contain more samples without lightning than with lightning, and vice versa with blue nodes.

4.3.1 TRF1 Performance

The first tier of the random forest (TRF1) was trained with a maximum of 20 leaf nodes, a maximum depth of five, and the number of trees set to 100. Contingency tables similar to Figure 3.5 were created for TRF1 with respect to the test dataset and a threshold of 0.5 (Figure 4.3a). False negative samples (3759) were slightly less frequent than the true positive samples (4848), while TRF1 identified over 118-thousand of the 119-thousand samples that did not contain lightning. Using the true positive, false negative, and false positive samples from TRF1 at the 0.5 probability threshold provided a POD of 0.56, a FAR of 0.20, and a CSI of 0.49. When the decision threshold was decreased from 0.5 to 0.05 (Figure 4.3b), samples between these thresholds were transferred into the predicted label of 'Yes Lightning'. At the considerably lower threshold of 0.05, the number of true positives increased to over eight thousand samples, while the number of false positive values increased one order of magnitude to over 16-thousand samples. Only 550 false negative events remained, providing a higher level of recall but a lower level of precision at this decreased threshold. The 0.05 probability yields a POD of 0.97, a FAR of 0.67, and a CSI of 0.33.

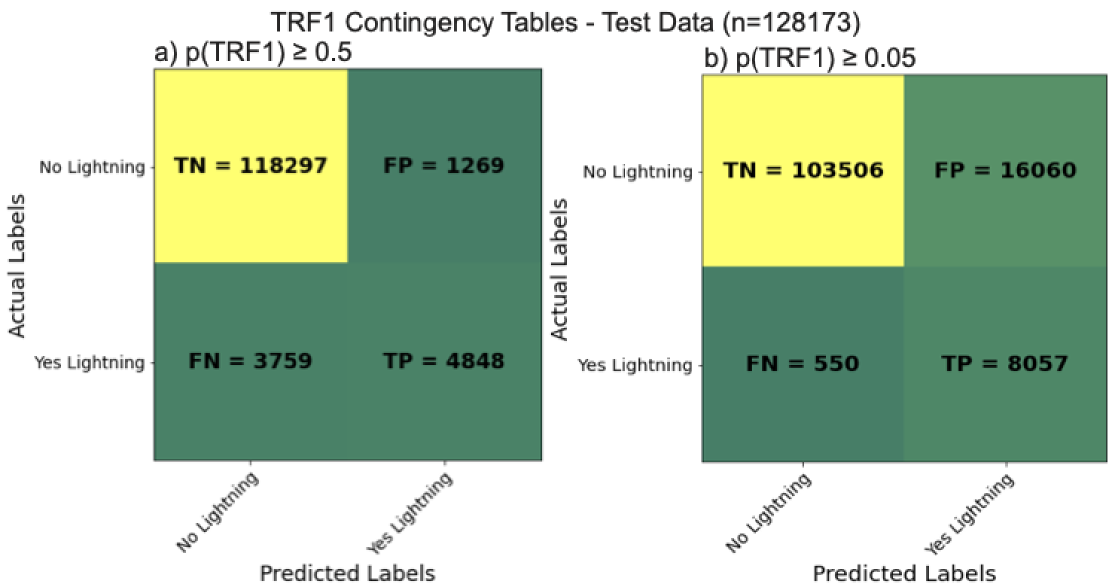

Figure 4.3: Contingency tables of test data from TRF1 for probability thresholds of 0.5 (a) and 0.05 (b).

The value of each predictor within TRF1 was examined by calculating the mean decrease in impurity (MDI), using the Gini impurity in the leaf nodes before and after the decision nodes that leveraged each variable (Figure 4.4). Both ABI variables had MDI values between 0.13 and 0.15, while both MRMS variables were between 0.30 and 0.45. Standard deviations of MDI values were nearly as large as the MDI values themselves, meaning a one standard deviation increase of the ABI variables would provide MDI values as high as 0.30 and a one standard deviation decrease in the MRMS variables would provide MDI values as low as 0.05. Overall the MRMS -10°C Reflectivity had the greatest MDI value of 0.41 and the ABI Clean-IR T_B had the lowest MDI value of 0.13.

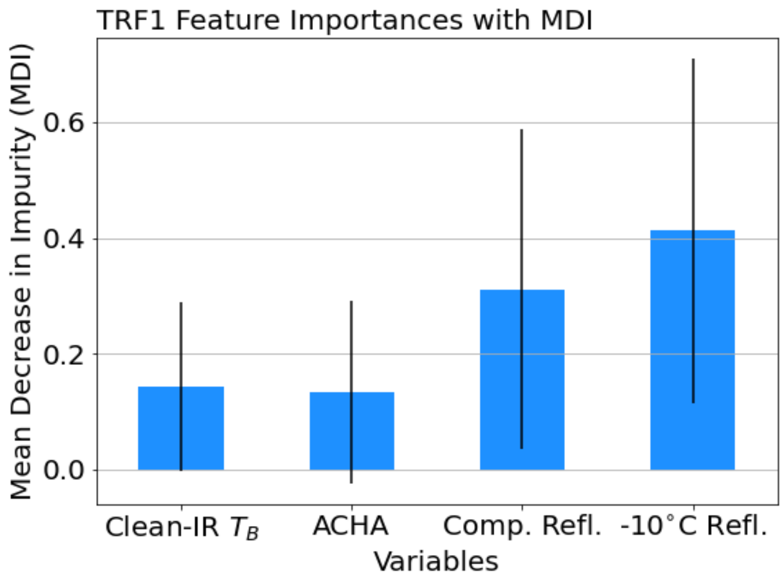

Figure 4.4: Feature importance of TRF1 in all testing data with respect to the mean decrease in the Gini impurity (MDI) through each decision node containing each of the predictors in the random forest. Black bars represent one standard deviation of variability within each predictor.

Reliability and performance diagrams were created for TRF1 probabilities to examine the performance of the model and its calibration with observed lightning frequency (Figure 4.5). Probabilities from TRF1 in Figure 4.5a were frequently near the perfect forecast line where the predicted and observed probabilities are similar. A slight underforecasting bias was observed for probabilities greater than 0.5, where the predicted probability was between 0.05 to 0.10 less than the observed probability. Additionally, the probability distribution from TRF1 contained over two-thirds of all output below the 0.05 probability threshold. The distribution of low TRF1 probabilities was shown in the performance diagram from Figure 4.5b, with a substantial increase in the success ratio (decreasing false alarm ratio) from 0.07 to 0.44 between TRF1 probabilities of 0.0 and 0.1. During this same period the probability of detection decreased from 1.0 to 0.89, while the critical success index increased from 0.07 to 0.42. As the decision probabilities from TRF1 increased further, POD values decreased while SR values increased. CSI values increased initially until the 0.3 and 0.4 probability thresholds, when they reached their peak of 0.53 while also crossing the bias line of 1 (where the number of false positive samples matched the number of true negative samples). These CSI values then decreased again to 0.22 at the last available TRF1 probability threshold of 0.87.

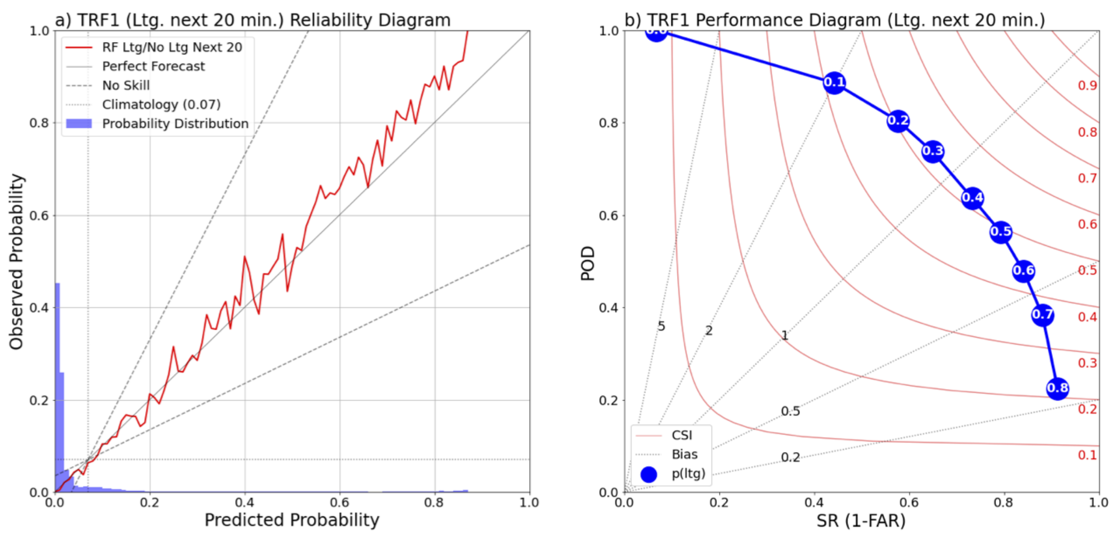

Figure 4.5: Reliability (a) and performance (b) diagrams of TRF1 with respect to the testing dataset. The scaled probability distribution is represented in panel a with values binned every 0.01.

To demonstrate how the ABI and MRMS predictors influenced the TRF1 probabilities, and relate them to the results from Chapters 2 and 3, two dimensional histograms were created comparing the ABI Clean-IR T_B with the ABI Cloud-Top Height and the MRMS -10 °C Reflectivity samples were created using the 0.05 probability threshold (Figure 4.6). Pixels with maximum reflectivity values of 0 dBZ were excluded from the analysis to focus on clouds with precipitation. When the TRF1 probabilities were below 0.05 in Figures 4.6a, distributions of cloud-top height and T_B peaked around 230 to 250 K and 9 to 11 km. No samples were observed at cloud-top T_B below 220 K and heights above 14 km. A second broad peak in the distribution occurred at cloud top heights between 7 and 12 km and brightness temperatures between 275 and 300 K. Isothermal reflectivity values at TRF1 probabilities below 0.05 (Figure 4.6b) were rarely above 23 dBZ with a peak in the distribution between 10 and 15 dBZ. When TRF1 probabilities are at least 0.05 (Figures 4.6c and d), the peak in cloud-top height distribution shifted to between 12 and 15 km, while the peaks in the cloud-top T_B were between 210 and 222 K and the isothermal reflectivity were between 15 and 30 dBZ. Samples were still found at warmer and lower cloud tops similar to the samples with TRF1 probabilities less than 0.05. Similarly, isothermal reflectivity values in Figure 4.6d were observed below 22 dBZ, especially for brightness temperatures below 225 K.

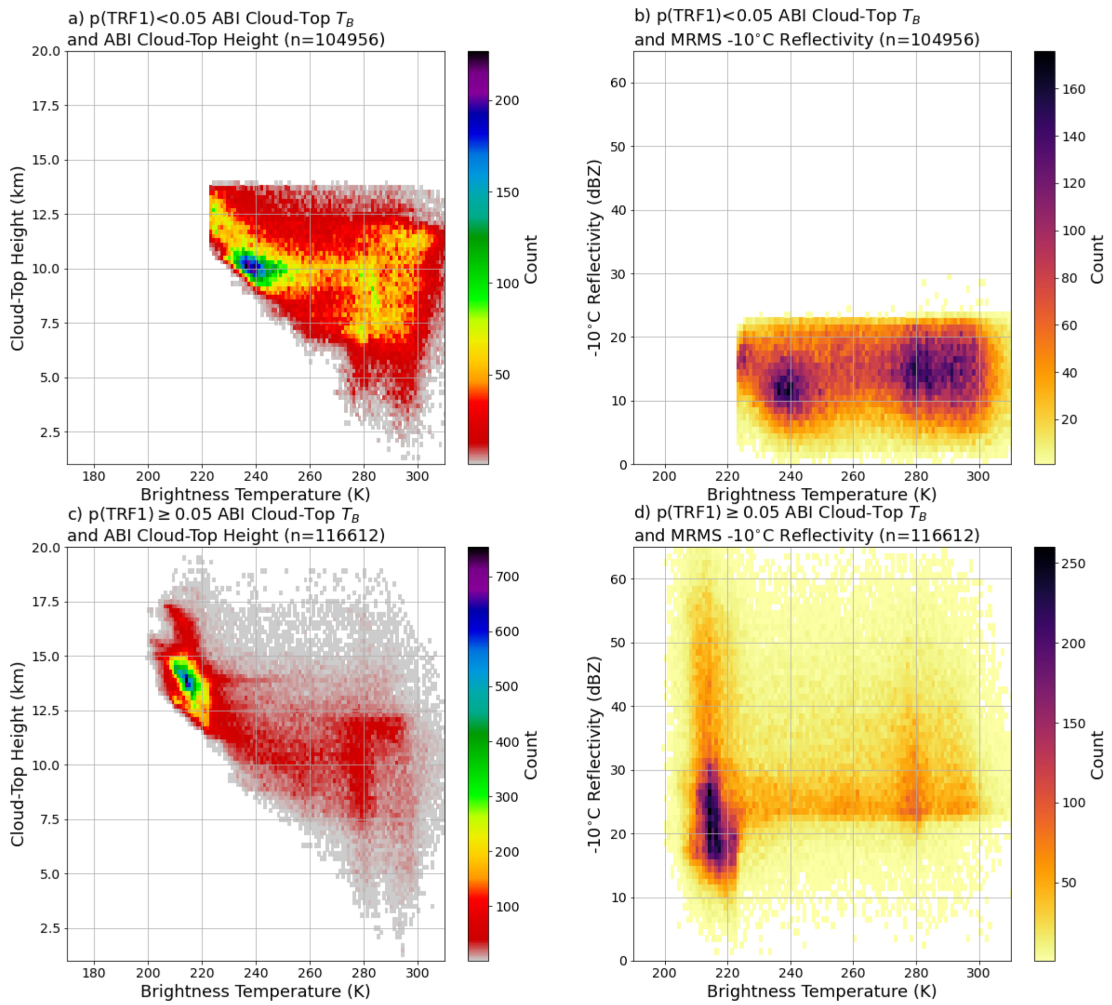

Figure 4.6: Histograms of ABI Cloud-Top T_B and Height (a and c) and ABI Cloud-Top T_B and MRMS -10°C Reflectivity (b and d) for all TRF1 probabilities less than 0.05 (top row) and at least 0.05 (bottom row). Cloud-Top Heights, Cloud-Top T_B, and -10 °C Reflectivity are binned every 200 m, 1 K, and 1 dBZ respectively.

4.4 Classifying Convection - TRF2

Based on the performance of TRF1 to identify convection by regions that did and did not produce lightning, a second-tier random forest (TRF2) was constructed to classify convection as 'strong' or 'weak'. Samples with TRF1 probabilities below 0.05 were excluded from the training and testing of the model. This threshold removed over two-thirds of the original sample as referenced in Figure 4.5a, while removing relatively few false negative (missed) events and none of the samples that would be classified as strong in the dataset. This threshold left 125-thousand of the original 640-thousand samples with approximately 19% labeled as strong and the other 81% labeled as weak. TRF2 was trained on the same four ABI and MRMS variables as TRF1, with the addition of the TRF1 probabilities themselves. The expectation when including the TRF1 probabilities was to provide additional calibration and characterization with samples where the probability of lightning occurrence may correspond with the probability of sustained lightning production. TRF2 contained the same hyperparameters as TRF1 with a maximum depth of 5, maximum leaf nodes of 20, and 100 trees making up the forest. Several combinations of hyperparameters were tested with similar results to the problem posed previously with TRF1, and with a limited number of predictors more shallow trees were preferred to avoid overfitting as shown in Figure 4.1.

4.4.1 TRF2 Performance

Another set of contingency tables were created for TRF2 at the 0.50 and 0.35 probability thresholds between strong and weak convection (Figure 4.7) using the over 25-thousand samples from the test dataset. When the probability threshold was set to 0.50 in Figure 4.7a, slightly fewer samples were classified incorrectly as weak convection (false negative samples: 2271) than correctly as strong convection (true positive samples: 2571). With 1032 samples classified incorrectly as strong convection, this provided a POD of 0.53, FAR of 0.29, and a CSI of 0.44. When the probability threshold was reduced to 0.35 in Figure 4.7b the contingency table was more balanced between the false negative (1769) and false positive (1806), while also increasing the number of correctly identified samples with strong convection (true positives: 3040). The POD, FAR, and CSI values under this threshold were 0.66, 0.36, and 0.48 respectively. When evaluating the feature importance of each variable in TRF2 using the mean decrease in the Gini impurity (Figure 4.8), the probabilities from TRF1 had the largest MDI value of 0.37. MRMS isothermal reflectivity and composite reflectivity had the next highest MDI values of 0.26 and 0.25 respectively, while both ABI variables had the lowest MDI values.

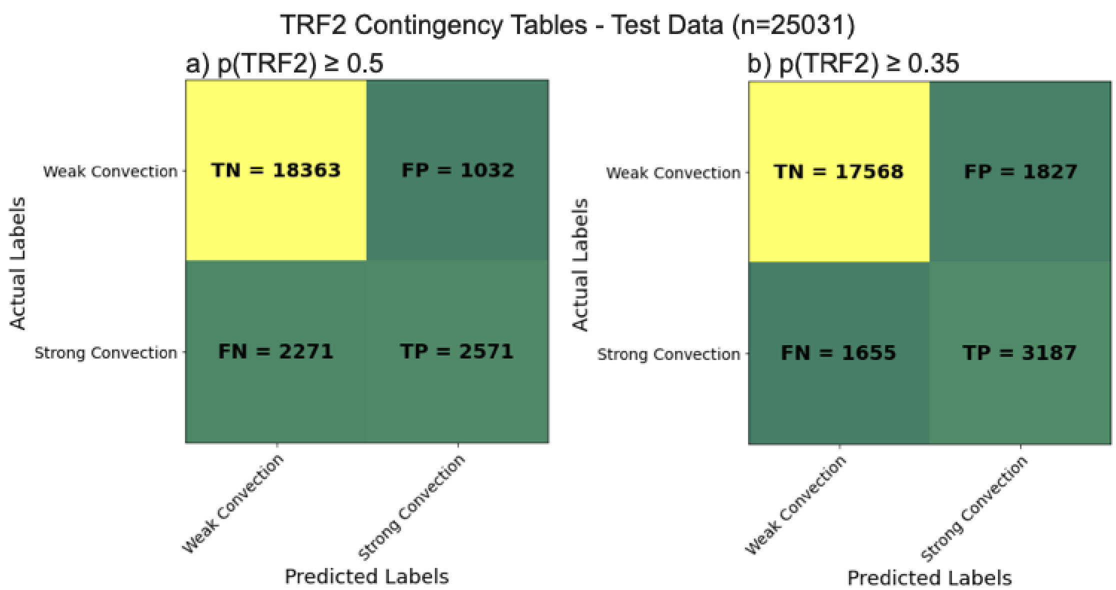

Figure 4.7: Contingency tables of test data from TRF2 for probability thresholds of 0.5 (a) and 0.35 (b).

TRF2 followed many similar trends to TRF1 when the probability distributions were placed within the reliability and performance diagrams (Figure 4.9). Within the

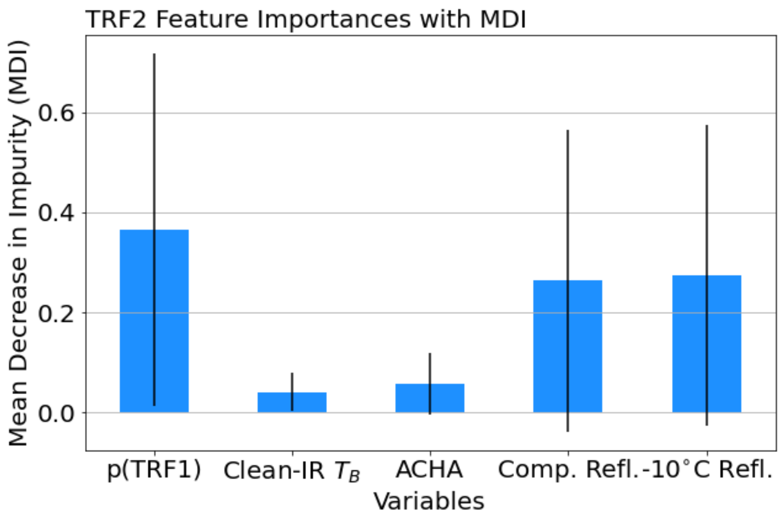

Figure 4.8: Feature importance of TRF2 in all testing data with respect to the mean decrease in the Gini impurity (MDI) when each predictor is removed. Black bars represent one standard deviation of variability within each variable.

reliability diagram in Figure 4.9a predicted probabilities match the observed probabilities, with notable variance around the 'Perfect Forecast' line. Probability distributions within the histrogram show little to no TRF2 probabilities below 0.03, with a peak in the distribution between 0.03 and 0.10. After the 0.10 probabilities the distribution decreased to lower values until a second peak was observed between the 0.70 and 0.82 TRF2 probabilities. TRF2 probabilities in the performance diagram from Figure 4.9b started from the base rate of 0.20 and monotonically increased in POD and SR as the TRF2 probabilities increased to 0.3. The TRF2 probability of 0.3 had to greatest CSI value of 0.48, crossing the bias line of 1 between the 0.3 and 0.4 probabilities. CSI values decreased steadily for increasing probabilities greater than 0.4, which were met with greater decreases in POD and only slight increases in SR.

While the 0.5 probability is the default decision threshold between strong and weak convection, the reduced number of false negative events, increased true positive events, and a model bias close to one motivated the decision to use the 0.35 probability instead

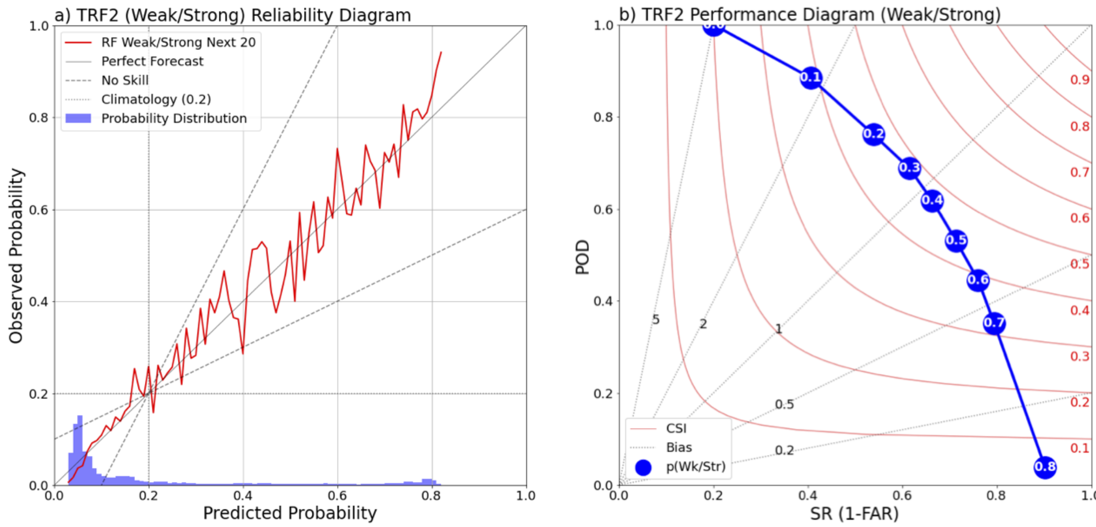

Figure 4.9: Reliability (a) and performance (b) diagrams of TRF2 with respect to the testing dataset. The scaled probability distribution is represented in panel a with values binned every 0.01.

as the threshold for classifying convection as strong or weak. Similar to Figure 4.6, the ABI and MRMS values used to train and test TRF2 were split along the 0.35 probability threshold in Figure 4.10. When comparing between the ABI cloud-top heights and T_B for samples with TRF2 probabilities of less than 0.35 or at least 0.35 (Figures 4.10a and c), peaks in the distribution showed only small differences. For TRF2 probabilities less than 0.35, cloud top T_B were most often between 210 and 220 K, while for samples with probabilities of at least 0.35 brightness temperatures were most often between 205 and 217 K. Similarly, cloud-top heights observed a slight increase of 12.6 and 14.8 km to 13.6 and 15.2 km between the respective categories. The most notable change in the distributions occurred from the removal of samples within warmer (greater than 230 K) cloud-top T_B for increasing probabilities. When the MRMS -10 °C isothermal reflectivity was included in the distributions (Figures 4.10b and d), the samples below the TRF2 probability of 0.35 were mostly between 15 and 30 dBZ. Conversely for TRF2 probabilities above 0.35 much of the distribution contained samples between

31 and 55 dBZ. These distributions showed substantial differences, with lower TRF2 probabilities rarely achieving isothermal reflectivity values over 30 or 40 dBZ. Vice versa, greater TRF2 probabilities were associated with isothermal reflectivity values exceeding 30 dBZ.

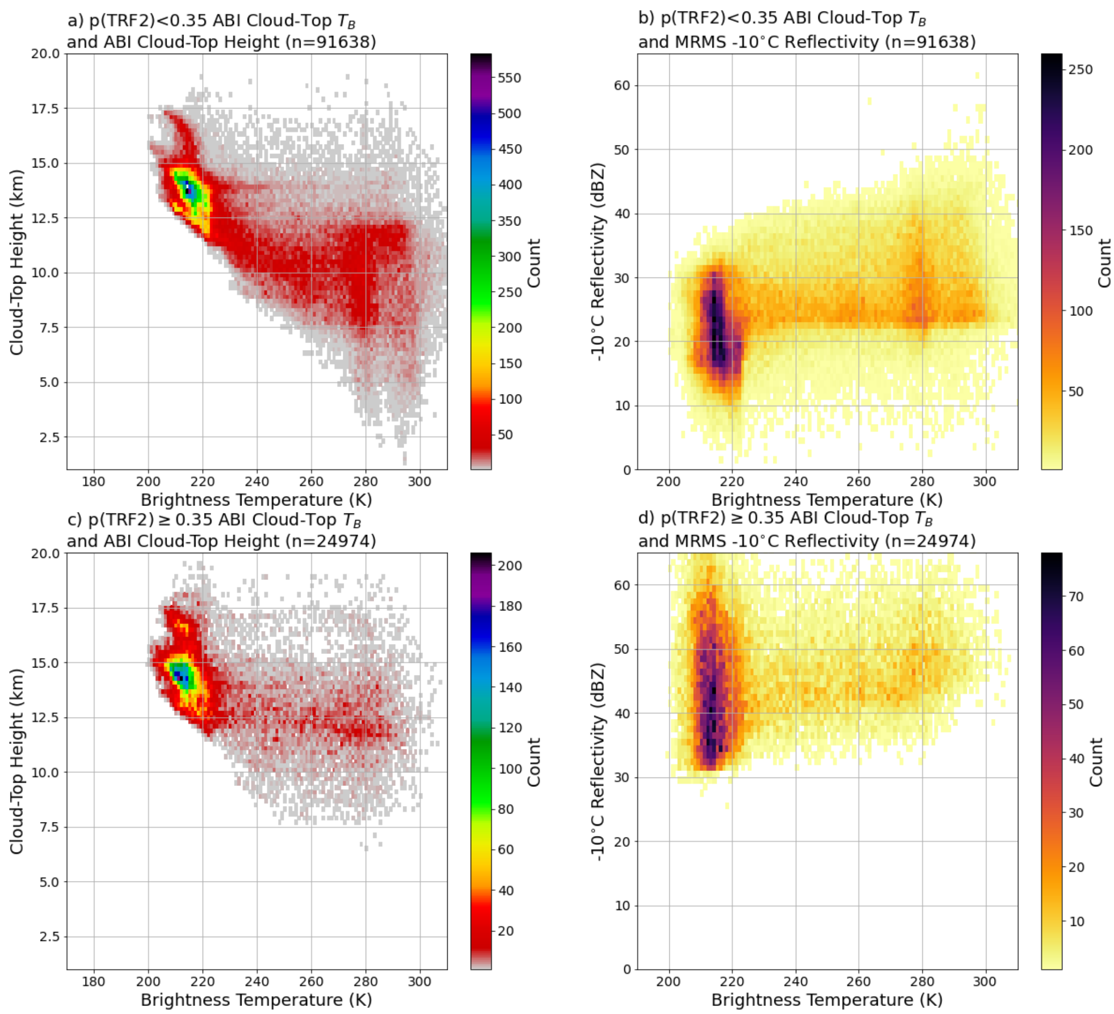

Figure 4.10: Histograms of ABI Cloud-Top T_B and Height (a and c) and ABI Cloud-Top T_B and MRMS -10° Reflectivity (b and d) for all TRF2 probabilities less than 0.35 (top row) and at least 0.35 (bottom row). Cloud-Top Heights, Cloud Top T_B, and -10°C Reflectivity are binned every 200 m, 1 K, and 1 dBZ respectively.

4.5 Case Study - 14 May 2022

4.5.1 Northwest Arkansas Thunderstorms

Thunderstorm activity during the afternoon of 14 May 2022 in the southern Mississippi Valley region was characterized by elevated convective instability, little to no inhibition, and modest deep layer shear, resulting in widespread and frequently disorganized convection. Per the Storm Prediction Center (SPC) Thunderstorm Event Archive (Carbin et al. 2000), surface-based CAPE from the SPC mesoanalysis exceeded 3000 J/kg by 1700 UTC across the entire forecast area. A remnant cold pool of the previous night's mesoscale convective system coincided with weak surface-based CIN in central and eastern Arkansas, with values decreasing as surface heating continued during the morning hours. The nearest available NWS radiosonde at 1200 UTC in Springfield, Missouri had 24 kts of 0 to 6 km shear and a 700 to 500 hPa lapse rate of -7.1 °C km^{-1}. By 1700 UTC the SPC mesoanalysis confirmed this strong convective instability with lapse rates between -7 and -8 °C km^{-1}. The combination of copious instability, weak inhibition, and modest deep-layer shear in the environment provided the potential for widespread thunderstorm activity (Figure 4.11).

Thunderstorms began around 1730 UTC, with isothermal reflectivity values appearing close to the border of Arkansas and Missouri with two discrete updrafts. By 1800 UTC TRF1 values exceeded 0.1 (10%) for the storm in southern Missouri and 0.25 (25%) for the storm in northern Arkansas, with isothermal reflectivity values of at least 25 and 35 dBZ respectively (Figure 4.11a). TRF2 classified both storms as weak across the four available pixels that exceeded TRF1 probabilities of 5% (Figure 4.11b), with neither storm producing lightning flashes as observed by GLM16. The storm in northern Arkansas continued to intensity with increasing isothermal reflectivity magnitudes and coverage, and its first GLM16 flash at 1815 UTC while TRF1 probabilities remained at 25% and TRF2 categories remained at weak convection. Thunderstorm activity in this area gradually increased until 1910 UTC, when the first TRF2 classifications of strong convection were observed for two pixels that coincided with TRF1 probabilities of at least 50%, but did not contain any GLM16 flashes. One pixel did not contain any lightning flashes 20 minutes later, while another contained three flashes. The coverage of convection increased further, along with more TRF2 strong convection pixels, as more GLM16 flashes were observed with convective cores with local isothermal reflectivity maxima exceeding 50 dBZ.

Over the next three hours the disorganized cluster of thunderstorms translated southeastward, as outflows helped to initiate new updrafts and thunderstorms. By 2200 UTC TRF1 probabilities exceeding 25% were widespread across the domain, with probabilities exceeding 75% within updrafts with isothermal reflectivity values greater than 50 dBZ (Figure 4.11c). Strong convection classifications from TRF2 were also more widespread and broadly aligned with TRF1 probabilities of 50%. Many of the strong pixels coincided with regions of focused GLM16 flashes (Figure 4.11d). Strong pixels with little-to-no flashes were adjacent and often to the east of ongoing thunderstorms. Two isolated thunderstorms developed along the border of Arkansas and Oklahoma over the following three hours, and remained stationary as the cluster of thunderstorms to the east decreased in intensity while moving further south. By 0200 UTC on 15 May TRF1 probabilities had decreased considerably to the east with a maximum contour of 25% and few GLM16 flashes during this period (Figure 4.11e). All TRF2 classifications to the east were weak, while two pixels from a thunderstorm in far northwestern Arkansas were classified as strong with many GLM16 flashes near the thunderstorm core (Figure 4.11f). No more flashes occurred to the east and continued to diminish after sunset at 0150 UTC, while the thunderstorm to the west continued to strengthen through 0300 UTC and dissipate by the end of the analysis period at 0400 UTC.

4.5.2 Mena, Arkansas Thunderstorm

From the case study previously described, one discrete thunderstorm of note occurred between 2230 UTC (14 May) and 0140 UTC (15 May) northwest of Mena, Arkansas. The discrete nature of this thunderstorm made it ideal to examine how the variables for TRF1 and TRF2 influenced their output and verified against GLM16 flashes (Figure 4.12). The storm began at 2230 UTC with a MRMS composite reflectivity of 5 dBZ and no -10°C reflectivity. The minimum cloud-top brightness temperature was over 290 K, and remained at these values for the following 45 minutes while the cloud-top heights frequently exceeded 9 km and both MRMS reflectivity values increased. At 2245 UTC TRF1 probabilities exceeded 5%, and therefore classifications from TRF2 began with a single pixel of weak convection. Both MRMS reflectivity products increased to between 25 and 30 dBZ from 2245 to 2300 UTC, signaling growth of the updraft into the mixed phase region supportive of non-inductive hydrometeor charging. By 2300 UTC TRF1 was at 20% as MRMS reflectivity values increased further, and TRF1 values by 2315 UTC were at 43% when the first lightning flash was recorded by GLM16. At this time the maximum isothermal reflectivity was 43 dBZ, while cloud-top heights and brightness temperatures were 11.1 km and 291 K respectively.

The next time step at 2320 UTC revealed the first TRF2 classification of strong convection and a maximum TRF1 probability of 54%, as cloud-top T_B decreased to 262 K and the isothermal reflectivity was then 46 dBZ. While only two flashes had occurred in the last 20 minutes from the thunderstorm, at 2325 UTC three additional flashes were recorded within the same pixel, raising the total to five flashes and verifying the storm as strong convection. TRF1 probabilities increased to 68% and storm total flash rates increased to seven flashes at 2335 UTC, which was the most flashes over the entire case. Also at 2335 UTC, MRMS MESH values exceeded 16 mm, suggesting a robust updraft capable of supporting hail production. Thirty-five minutes later at 0010 UTC TRF1 produced its greatest probability for the case of over 73% while isothermal reflectivity frequently exceeded 50 dBZ. TRF2 continued to classify the storm as strong convection and cloud-top T_B were between 215 and 225 K. After this maxima in TRF1 probabilities, they decreased to 59%, -10°C reflectivities decreased to 48 dBZ, and TRF2 classifications returned to weak convection at 0020 UTC. Flash rates at this time returned to zero and no more flashes were produced for the rest of the case. TRF1 probabilities decreased to below 10% at 0045 UTC and remained there as -10°C reflectivities fell below 25 dBZ and cloud-top T_B slowly increased. TRF2 probabilities ceased for the storm after 0110 UTC while cloud-top T_B increased to above 250 K. After 0130 UTC isothermal and composite reflectivities decreased below 10 dBZ to 0 dBZ at 0140 UTC, as the thunderstorm had almost entirely dissipated.

4.5.3 Fayetteville, Arkansas Thunderstorm

A thunderstorm started to develop northwest of Fayetteville, Arkansas around approximately 0100 UTC and produced substantially greater flash rates and one report of severe hail from the NWS (Figure 4.13). Similar to the previous case, the stationary and discrete nature of this thunderstorm provided the opportunity to view a storm of greater intensity. Maximum TRF1 probabilities initially were below 1% prior to 0115 UTC while -10 °C isothermal reflectivities were below 15 dBZ, cloud-top brightness temperatures were around 290 K and cloud-top heights were above 10 km. Once TRF1 probabilities exceeded 5% at 0120 UTC TRF2 categorizations began. MRMS isothermal reflectivity maxima increased to 39 dBZ by 0140, coinciding with the first recorded GLM flash, the appearance of MRMS MESH values, and a 36% TRF1 probability. Flash rates exceeded the five flash threshold for strong convection five minutes later at 0145 UTC, and continued increasing to over 20 flashes by 0155 UTC when TRF2 started to classify the storm as strong convection. TRF1 probabilities exceeded 70% by this time, with isothermal reflectivity values of 51 dBZ, MESH values of 16 mm, and a minimum cloud-top brightness temperature of 238 K.

Storm total flash rates from GLM16 continued to increase after 0155 UTC to over 100 flashes per 20 minutes by 0240 UTC, coinciding with the case maxima in isothermal reflectivity of 63 dBZ and MESH of 56 mm. TRF1 probabilities had exceeded 80% since 0210 UTC, nearing the maximum possible output by the model. The peak in radar-derived intensity was proceeded by a report of severe hail of approximately 38 mm (1.5 inches) ten minutes later at 0250 UTC. Flash rates continued to increase after the severe hail report until the case maxima of 162 flashes at 0310 UTC, meanwhile both MRMS reflectivity variables decreased slightly below 60 dBZ and the MESH product declined to 16 mm. Afterwards all variables except for those from the ABI began to decline until TRF2 returned to the classification of weak convection at 0335 UTC when the -10 °C isothermal reflectivity maxima fell to 29 dBZ with a TRF1 probability of 47%. TRF1 probabilities quickly declined to below 10% by 0345 UTC as both MRMS reflectivity products also declined to below 30 dBZ and the storm stopped producing lightning. The remnants of the thunderstorm then moved slowly southeastward with the upper level flow until the end of the period of study at 0400 UTC.

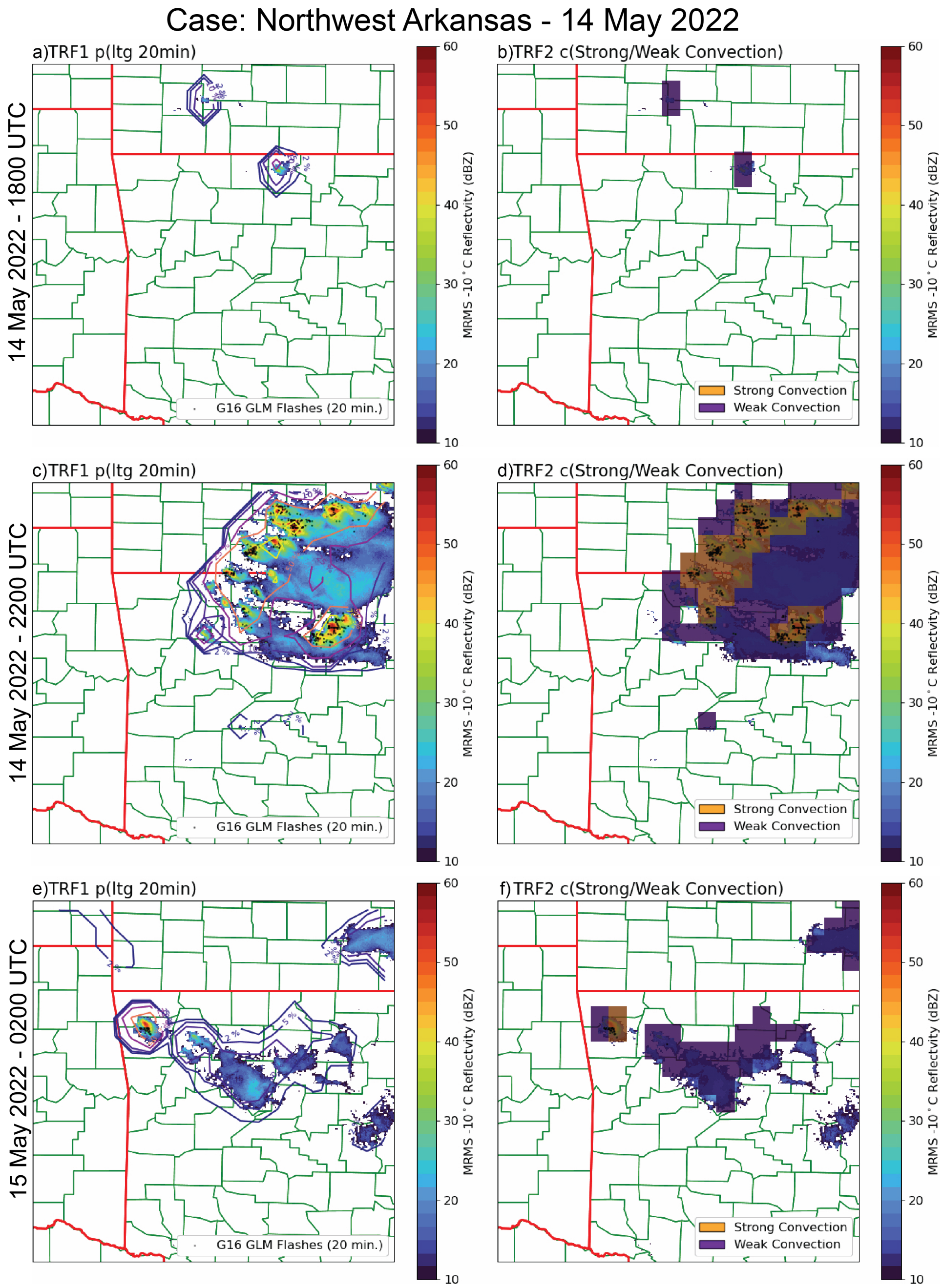

Figure 4.11: TRF1 probabilities (a, c, and e) and TRF2 classifications (b, d, and f) overlaid on MRMS -10°C Reflectivity for the case study in northwest Arkansas. Times shown are 1800 and 2200 UTC on 14 May 2022 and 200 UTC on 15 May 2022. TRF1 probabilities are contoured at the 2%, 5%, 10%, 25%, 50%, and 75% thresholds. TRF2 classifications are categorized by strong convection (orange) and weak convection (purple) for every available pixel.

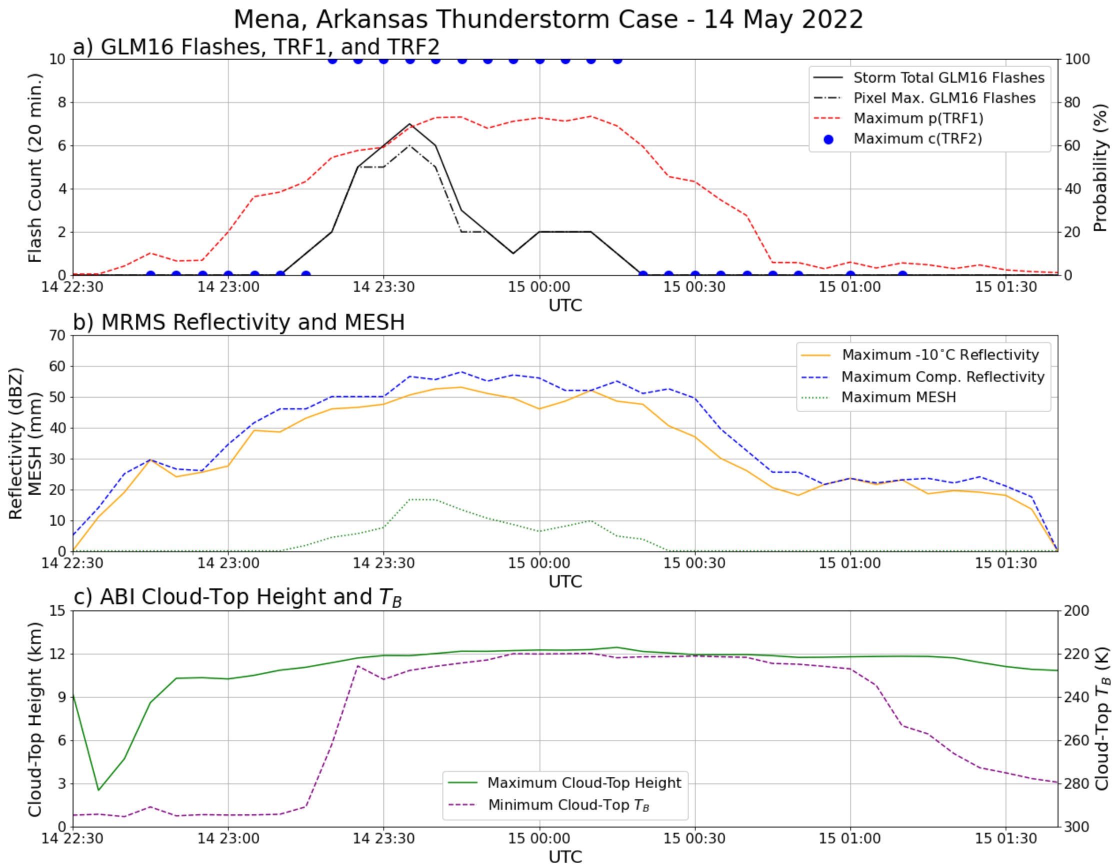

Figure 4.12: Time series from a thunderstorm near Mena, Arkansas between 14 May 2022 at 2230 UTC and 15 May 2022 at 0140 UTC. Panel a shows the probabilistic output of TRF1, deterministic output of TRF2, the total number of GLM16 flashes, and the maximum number of GLM16 flashes in a pixel. Panel b shows a time series of the maximum MRMS -10°C Reflectivity and Composite Reflectivity. Panel c shows a time series of the ABI maximum cloud-top height and Clean-IR T_B.

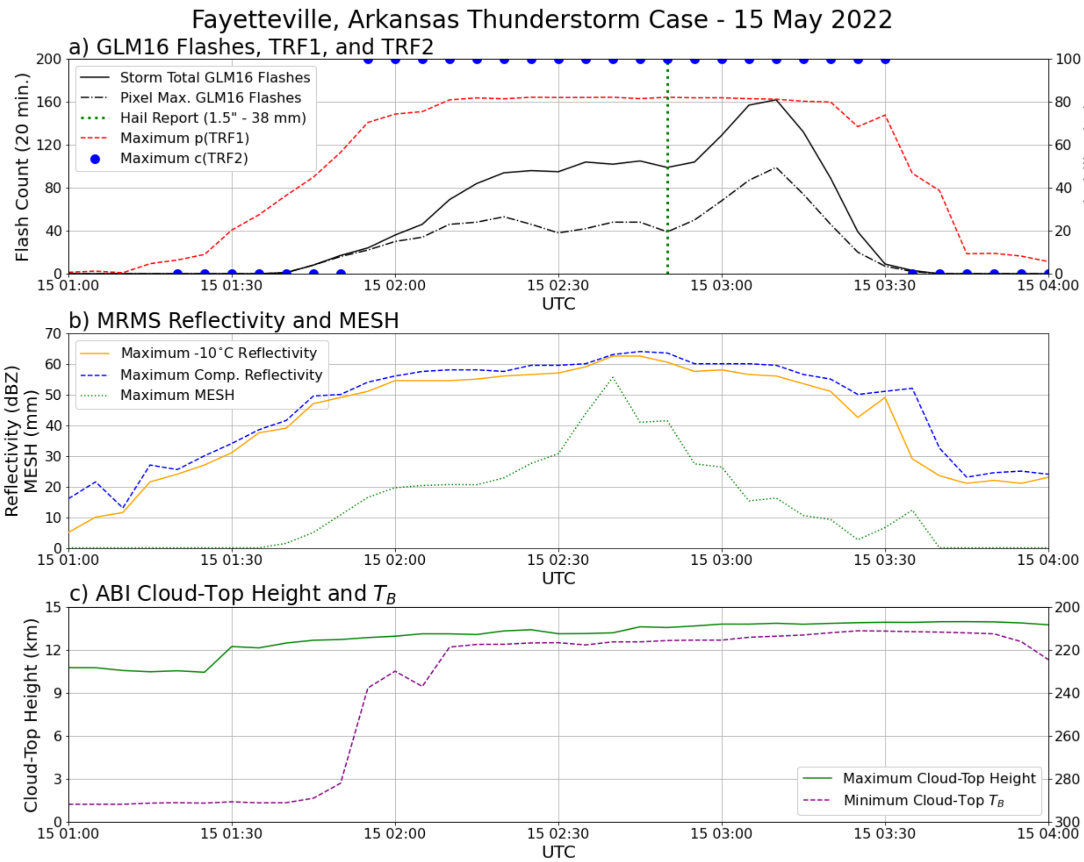

Figure 4.13: Time series from a thunderstorm near Fayetteville, Arkansas between 15 May 2022 at 0100 UTC and 15 May 2022 at 0400 UTC. Panel a shows the probabilistic output of TRF1, deterministic output of TRF2, the total number of GLM16 flashes, the maximum number of GLM16 flashes in a pixel, and a severe (1.0 inch) hail report at 255 UTC. Panel b shows a time series of the maximum MRMS -10°C Reflectivity and Composite Reflectivity. Panel c shows a time series of the ABI maximum cloud-top height and Clean-IR T_B.

4.6 Discussion

4.6.1 Identifying and Classifying Convection

Thresholds with respect to severe convection and its onset were discussed in Chapters 2 and 3 respectively. In the current chapter, many similar variables were employed to identify the potential for observed convection to produce lightning along with if convection was defined as 'strong' or 'weak'. While these two sets of categories are not identical, they represent points along a continuum of intensity. Changes in convection and their resultant observed distributions were represented by the two dimensional histograms from Figures 2.6, 2.7, 3.17, 4.6, and 4.10. In the early stages of convection, where TRF1 probabilities were below 5%, ABI cloud-top brightness temperatures were warmer than 220 K and MRMS -10°C reflectivities were less than 23 dBZ (Figure 4.6), with the rest of the population observed at colder brightness temperatures and greater isothermal reflectivity values. However, by the time of the first lightning flash as shown in Figure 3.17, brightness temperatures cooled to between 220 and 230 K, while isothermal reflectivity values increased to between 35 and 45 dBZ. The population of ABI and MRMS samples containing GLM lightning activity however indicated a shift in the distributions (Figure 2.6a), with brightness temperatures between 200 and 220 K and isothermal reflectivities between 25 and 35 dBZ.

As thunderstorms intensify and become associated with severe convective hazards (Figure 2.7a) brightness temperatures remained between 200 and 220 K as isothermal reflectivities increased to frequently over 30 dBZ and a peak concentration of samples between 40 and 55 dBZ. Probabilities from TRF2 at the 35% decision threshold also reflected the intensity of 'strong' convection with brightness temperatures again between 200 and 220 K, isothermal reflectivity values greater than 30 dBZ, and a peak concentration of samples between 30 and 50 dBZ. The distributions presented from Chapters

2, 3, and 4 were constructed from three different sets of data with unique sampling methods and domains designed for their respective study. Even with these differences, cloud-top T_B below 220 K were noted as a marker for increased lightning activity, and therefore increased updraft strength. Meanwhile -10 °C isothermal reflectivity values greater than 30 dBZ showed the increasing likelihood of lightning production, and values greater than 40 dBZ showed the increasing likelihood for more intense convection potentially capable of producing severe convective hazards.

The two case studies of thunderstorms in northwest Arkansas highlighted the development of convection followed by intensification and dissipation. These were reflected in the thunderstorm processes themselves and reflected in the inputs and outputs of TRF1 and TRF2. Increasing isothermal reflectivity at the beginning of each case exceeding 30 dBZ were met with increasing TRF1 probabilities. These features were consistent with observations from Stolzenburg et al. (2015) of reflectivity development above the -10 °C isotherm and its correspondence with robust charge separation within the mixed phase region. TRF1 probabilities at the time of the first lightning flash were 43% for the Mena, Arkansas case and 36% for the Fayetteville, Arkansas case. After the first lightning flash both thunderstorms intensified further, supported by the change in TRF2 classifications from weak convection to strong convection. In the Mena, Arkansas case the first classification of strong convection occurs five minutes before the rate of five flashes per 20 minutes was observed, while in the Fayetteville, Arkansas case this classification occurred ten minutes after the rate of five flashes per 20 minutes. As each thunderstorm enters its respective dissipation stage, lightning activity quickly decreased without the presence of a strong and deep updraft. The overall performance of TRF1 and TRF2 suggests that both models show the ability to discriminate between their respective tasks of identifying regions with lightning activity and regions with intense convection. When compared to other machine learning models designed for similar tasks, such as LightningCast (Cintineo et al. 2022), ThunderCast (Ortland et al. 2023), IntenseStormNet (Cintineo et al. 2020b), and ProbSevere Version 2 (Cintineo et al. 2020a), TRF1 and TRF2 provide similar measures of reliability and comparable CSI values. However, these referenced models feature increased sophistication in their methods - such as applying Convolutional Neural Networks (Géron 2019) for spatial feature processing - and more robust training datasets to expand their operational applicability in convective forecasting (Thiel 2022). For the purposes of this study, TRF1 and TRF2 were viewed as diagnostic tools to validate previous observations and thresholds at key stages in convective development.

4.6.2 Machine Learning Considerations

When constructing TRF1 and TRF2, several decisions were made to pose a machine learning task that could be addressed by a random forest. Many of these decisions, and their consequences, were driven by the creation of the training dataset and its application to each machine learning model. The first decision of note was the definition of 'strong convection' based only on the local lightning flash rate. As an updraft intensifies, it can produce greater local flash rates (Williams et al. 1999; Schultz et al. 2011) which may exceed hundreds of flashes per minute (Calhoun et al. 2013). Several flash rates were tested to define 'strong convection' when training TRF2, and the use of GLM flash centroid points within each grid cell motivated the need for reduced flash rates in comparison to the GLM gridded flash extent density product. This ensured that areas of concentrated lightning activity could be evaluated as robust updrafts, especially when considering the increasing proportion of flash rates greater than five flashes per 20 minutes with respect to the increasing maximum isothermal reflectivity (not shown). On the other hand, a lower threshold provided a dataset with a high enough base rate to be trained on the limited variables in the random forest.

Training TRF2 on samples with TRF1 probabilities of at least 5% also contributes to this threshold, by ensuring the potential for lightning activity and ensuring the recall of intense convection. No pixels with GLM flash rates of five flashes per 20 minutes or greater contained TRF1 probabilities less than 5%, and therefore retained all possible samples for the TRF2 training dataset. Lastly, TRF2 was presented as a binary classification between strong and weak convection for the case studies in Figures 3.1, 4.12, and 4.13. The selected probability threshold of 35% for TRF2 could be adjusted based upon a user's threshold and risk tolerance using the performance diagram from Figure 4.9b.

The grid spacing used by TRF1 and TRF2 may also impact its training dataset and results. The resolution of 0.2 ° in latitude and longitude was designed to match the approximate resolution of the datasets employed by Thiel et al. (2020) and Chapter 2 of 20 km, and was found to be sufficient when considering radar and satellite-based observations. Across the CONUS, the pixel area with the presented resolution varied from approximately 319 km^2 at 25 °N latitude to 448 km^2 at 50 °N latitude. It is expected these sample areas would have relatively minor impacts on the MRMS and ABI variables provided as inputs, however the target metric for TRF2 relies on the number of GLM flashes in a given area and may bias observations of strong convection further toward the southern end of the domain. Variations in the GLM flash detection efficiency across the CONUS (Murphy and Said 2020; Bateman et al. 2021) may further contribute to this bias. These biases can introduce ambiguity into the definition of strong convection employed in this study. Implementing thresholds on gridded GLM imagery to classify strong convection may also assist, as they can leverage the spatial footprint of the given flash (Bruning 2019). Additionally, GLM flash area has been observed in the HWT to be more resistant to reductions in flash detection efficiency and therefore reduced flash extent densities (Thiel 2022), and as observed in Chapter 2 the smallest GLM flashes and greatest flash rates are commonly associated with intense and severe convection.

The training, testing, and demonstration datasets were compiled from primarily summertime convection, with a substantial bias to the central United States. The inclusion of more events in the testing and training dataset, which better reflect the diversity of thunderstorm signatures across the Continental United States, may lead to a more equitable assessment of the probabilities from each model. Additionally the limited spatiotemporal domains of each case - focused explicitly on convection - provided base rates of 7% for TRF1 and 20% for TRF2. These rates are considerably higher than the true climatology of lightning and intense convection, especially in comparison to the base rates from similar machine learning training datasets (Cintineo et al. 2020a,b, 2022). However, by training on random forests for both tiers no scaling was required and produced relatively consistent probabilities when considering the limited sample size (Géron 2019). By using only four ABI and MRMS variables as inputs for TRF1 and TRF2, trees in the random forest were more shallow in depth to avoid overfitting (Figure 4.1). Similar to the results in Chapter 3, one method to improve model performance may be through including environmental fields related to convective instability, moisture, lapse rates, shear, or convective indices. These variables may provide key context and additional confidence in modeled probabilities, such as the ability to discriminate between environments supportive of rapid convective development with accompanying lightning production and those with more marginal support for convection. Additional MRMS and ABI variables such as Vertically Integrated Ice (VII) (Carey and Rutledge 2000; Mosier et al. 2011) or additional satellite bands similar to those employed by Cintineo et al. (2022) may also provide a more complete picture of convection from each platform. Lastly, it has been suggested that including elevation as a variable may benefit model performance in regions with higher elevations by considering the impact of topography on convection (M. Flora, personal communication - November 2024).

During both case studies (Figures 4.12 and 4.13), minimum ABI cloud-top brightness temperatures were greater than 290 K until the thunderstorms were already producing lightning and continuing to intensify. Only then did cloud-top T_B decrease to below 240 K, which more reasonably matched the observed maximum cloud-top heights. Minimum cloud-top T_B of approximately 290 K, when compared against the 0000 UTC radiosonde observation from Little Rock, Arkansas (Carbin et al. 2000) suggest the values sampled are from cumulus cloud near the lifting condensation level which should be approximately 2 km in height. These results suggest that cirrus clouds overhead of the developing thunderstorm may have introduced spatial errors into the attempted parallax correction from the ABI cloud-top heights, displacing the true cloud-top brightness values too far to the southeast and outside of the predefined thunderstorm domain. The discrepancy between the convective cloud-top height and the reported height from the ABI cloud-top height algorithm for weak or developing convection was noted by Thiel et al. (2020) and in Chapter 2. These observations of high, but warm, clouds appear again in Figure 4.6a and c along with Figure 4.10a, with samples spread along a variety of cloud-top heights with decreasing brightness temperature. Parallax-correction errors may also decrease the predictive skill of satellite-based variables in TRF1 and TRF2 by spatially de-correlating satellite observations with the GLM flash locations and densities. Methods such as a universal parallax correction of 9 km in height (Cintineo et al. 2022) or adaptive methods which estimate cloud-top height from a variety of satellite and climatological data sources (Stough et al. 2025) may be explored in future studies.

Chapter 5

Summary

This dissertation explored applications of the GOES-R Geostationary Lightning Mapper with respect to severe and local storms. Gridded GLM imagery related to flash density, area, and optical energy were examined in two cases of semi-discrete supercells, and a seven-week study in April and May of 2019 in the central and eastern United States. These data were compared with signatures from satellite imagery, radar data, ground-based lightning networks detections, and reports of severe weather to identify trends and thresholds for short-term convective forecasting. Next, GLM flashes were leveraged to identify developing convection through their first lightning flash (i.e. first flashes). First flashes were manually examined from multiple lightning location systems, and with over three-thousand candidate first flashes to identify optimal identification criteria for a year-long study. Satellite and radar signatures that coincided with these flashes were then exploited to identify additional thresholds and trends with respect to developing convection. Lastly GLM flashes, satellite imagery, and radar data were used to identify convection and classify its intensity using a two-tiered machine learning model. The performance of this model provided additional context and validation for the observations from the previous two studies.

5.1 Gridded GLM Imagery

In Chapter 2 (Thiel et al. 2023) gridded GLM products were examined with ABI satellite imagery, MRMS reflectivity products, and one ground-based lightning network to validate GLM imagery and provide applications when merged with other operational products. Two case studies of semi-discrete supercells in southeast Kansas (24 May 2019) and central Alabama (25 March 2021) provided storm scale observations and trends relative to convective evolution. A bulk, seven week study of convection across the central and eastern United States then gave additional context and applications. Overall, the GLM gridded products provided complimentary information with respect to convective evolution and severity potential. Similar to previous studies, the inverse relationship between local flash rate and area was identified using Flash Extent Density and Minimum Flash Area. Increasing FED coincided with decreasing MFA with respect to decreasing IR brightness temperatures and increasing isothermal reflectivity at -10 °C, vertically integrated ice, and maximum expected size of hail within the bulk study. This relationship was especially apparent when isothermal reflectivity values exceeded 30 dBZ or when examining imagery near local storm reports. During both case studies, increasing FED and decreasing MFA coincided temporally with increasing intensity from the MRMS variables and the convective evolution of each storm, and during the 24 May 2019 Kansas supercell even preceded the development of a robust mesocyclone. This FED-MFA signal, when combined with other radar and satellite observations, may provide additional confidence that a thunderstorm is intensifying and therefore its potential to produce severe weather is increasing. When examining the differences in viewing angles from GOES-East and GOES-West of the same storm, MFA provided more consistent signals near the edge of the field of view making it a useful product for evaluating updraft intensity when paired with FED. Additionally larger MFA values were discovered between clean-IR brightness temperatures of 210 to 230 K and -10 °C isothermal reflectivity values from 20 to 30 dBZ, which can help forecasters identify regions where larger flashes are more likely such as in stratiform precipitation.

Throughout the study, GLM Total Optical Energy values displayed multiple dependencies, which were especially apparent with GLM-to-GLM intercomparisons within the two supercell case studies. In both case studies, the western perspective of the GOES-17 GLM provided a more direct observation of flashes within the updraft, which during periods of intensification led to rapid increases in TOE observations from the GOES-17 GLM but not the GOES-16 GLM. While previous studies suggest that the GOES-East GLM provides improved detection efficiencies for areas east of 103 °W, and vice versa for the GOES-West GLM, operationally useful information regarding the quality of GLM observations may be available when using GLM data from both perspectives. Variability in local and storm-total flash rates from each GLM further supported these results, as peaks in the GOES-West GLM TOE corresponded with times of comparable FED and storm-total flash rates from the GOES-East GLM. These results suggest greater exploration of the Total Optical Energy product from the GOES-East and GOES-West GLM perspectives are needed to fully assess GLM data quality, and that dual-GLM observations of severe convective storms in regions of sensor overlap may provide critical context to the flash characteristics observed from each GLM with respect to other observing platforms such as satellite imagery and radar. In an operational environment, limited screen space and task saturation by forecasters in convective scenarios may inhibit the use of dual-GLM observations. Therefore, automated data fusion methods that leverage machine learning such as ProbSevere (Cintineo et al. 2020a) may be able to simplify this task when monitoring convection while still providing operational forecasters critical information with respect to thunderstorm evolution.

5.2 GLM First Flashes

Chapter 3 transitioned from investigating the GLM perspective of severe convection to developing convection, through the first lightning flash produced by a thunderstorm. First flashes were manually identified in two case studies within the domains of the Oklahoma and NSSL LMAs, and intercomparisons were made with data from GLM16, GLM17, ENI, and their respective LMAs. Next, over three-thousand potential first flashes were manually analyzed from seven periods of semi-discrete convection across the CONUS to inform an objective method for identifying first flashes. After evaluating fifty combinations of time, space, and flash area criteria, a first flash was defined as the first GLM flash where none have existed in the previous 20 minutes and a 20 km radius, plus the radius of the flash's area using a circular approximation. This provided an estimated first flash detection efficiency of 30-40% and a false alarm ratio of 5-10%. Using this definition, almost 170-thousand first flashes were identified using GLM16 and GLM17 flashes throughout 2022 in the continental United States.

First flashes most frequently occurred near the hours of peak daily insolation (1200 - 1600 LST) and during the boreal summer months with a peak in July and August. Developing convection was more likely during the overnight hours across the central Great Plains, driven by the prevalence of mesoscale convective systems and support from the Great Plains Low Level Jet. From the case studies and the year-long study, first flashes were more likely to be smaller in area and shorter in duration compared to all other GLM flashes associated with continental convection. Daily and seasonal variations in first flash area and duration coincided with the available diurnal convective instability and the resultant turbulence of the updraft and its organized regions of charge. When comparing the first flashes to their ambient satellite and radar data, first flashes most frequently occurred in regions with MRMS isothermal reflectivity at -10 °C of 35 to 45 dBZ, ABI cloud-top heights of 9 to 11 km, and ABI Clean-IR T_B of 220 to 240 K. In the southwestern United States, increased instances of developing convection coincided with regions of elevated terrain and peak daytime heating. Seasonally, large increases in monthly first flash counts in the region corresponded with the North American Monsoon and its early onset in 2022. The southeastern United States also had an increased density of first flashes along the coast of the Gulf of Mexico and Atlantic Ocean, with timing that coincided with the traditional onset of sea breeze convection.

Objectively identified first flashes from GLM16 and GLM17 were matched against ENI flashes, to leverage additional flash characteristics such as its classification as IC or CG. From the 73% of ENI-matched first flashes, the IC to CG ratio was 1.60 with the greatest proportion of IC flashes in the High Plains and Mid-Atlantic regions. More equal proportions of IC and CG flashes were also observed in the southwestern United States and along the lower Mississippi River Valley. As a validation measure, and to ensure no network biases within the ENI dataset, a random forest IC-CG classification model using only GLM flash attributes from Ringhausen et al. (2021) was employed. Of the 73% of ENI-matched first flashes 73% of them had identical classifications with the RRF model. The IC-CG ratio from the RRF model was 1.87 suggesting that the ENI-unmatched first flashes were likely IC flashes. Spatially the RRF model's IC-CG proportions were not as continuous across the CONUS, however when combining the ENI-matched first flashes with the RRF classified first flashes there was a more pronounced bias to CG flashes in the southwestern United States. While regional variations are less certain, it remains that first flashes are more likely to be IC flashes with exception to elevated regions such as the southwestern United States.

Overall, this study characterizes the first flash associated with developing convection across the CONUS through an entire year to examine daily, seasonal, and regional variations of convection. While one year of data was ideal for the purposes of this study, it does not provide a complete picture of inter-annual variability for thunderstorm activity and development. Future studies may extend this domain through the entire period of operational GLMs from the GOES-East and GOES-West perspectives. The December 2022 launch of the Meteosat Third Generation Lightning Imager and Flexible Combined Imager in geostationary orbit, centered at 0 °W, provides the opportunity to expand these analyses to other locations of frequent thunderstorm activity and provide regional characterizations of thunderstorm development (Holmlund et al. 2021). Future follow-on missions to the GOES-R series from GeoXO (Lindsey et al. 2024) show the potential for geostationary lightning observations extending into the 2040s and even longer lengths of record to leverage for studying developing convection. On the other hand, more localized analyses may be completed from the dataset presented, as local characteristics of convection may provide more impactful information to the operational community. Another limitation of this study was the inability to characterize the ambient environment from which deep convection develops. It is recommended that environmental fields be included in future studies to further characterize and assert the predictability of these environments. Features such as convective instability from convective available potential energy, convective inhibition, deep layer wind shear, or combined fields such as WMAXSHEAR as noted in Taszarek et al. (2020) are expected to add critical context to thunderstorm development, especially on daily, seasonal, and regional scales.

5.3 Machine Learning Applications

Using the results from Chapters 2 and 3, machine learning problems were posed in Chapter 4 to validate the previous findings and explore their applications scientifically and operationally. A two-tiered random forest model was trained on GLM, ABI, and MRMS data at a horizontal resolution of 0.2 ° latitude and longitude, using the same domains as the manually analyzed first flashes from the previous study. The first tier of the random forest model - TRF1 - used ABI and MRMS variables to estimate the probability that pixel would have at least one GLM flash in the next 20 minutes. Over two-thirds of all samples in the testing dataset contained TRF1 probabilities below 5%, however TRF1 was well calibrated when considering its limited training data set and number of predictors. CSI values for TRF1 peaked at probability thresholds between 30% and 40%, while the 50% threshold had a POD of 0.56, a FAR of 0.20, and a CSI of 0.49. Feature importance testing was conducted for TRF1, and demonstrated that the model relies more on the MRMS composite and -10 °C isothermal reflectivity when compared to the satellite observations of brightness temperature and cloud-top height. The -10 °C isothermal reflectivity variable provided the most information gain for TRF1. When the TRF1 decision threshold was set to 5%, ABI brightness temperatures warmer than 220 K and MRMS -10 °C isothermal reflectivity less than 23 dBZ were frequently not associated with lightning activity.

The second tier of the random forest model - TRF2 - used TRF1 probabilities greater than 5% along with the same ABI and MRMS information to classify convection as 'strong' or 'weak' based on the threshold of at least five GLM flashes within a pixel in the next 20 minutes. Even when removing over two thirds of the original data set for testing and training, the TRF2 model remained well calibrated throughout its distribution of predicted probabilities. Feature importance testing from TRF2 revealed similar trends to TRF1, with exception that the probabilities from TRF1 now were considered the most useful. At the default decision probability of 50%, TRF2 had a POD of 0.53, FAR of 0.29, and CSI of 0.44. CSI values for TRF2 maximize around the 35% threshold at 0.48 with a POD of 0.66 and FAR of 0.36. Based on the need to reduce the number of missed events and the bias between missed events and false alarms, 35% was selected as the decision threshold for classifying between strong or weak convection. At this threshold few differences in cloud-top brightness temperature were observed between strong and weak convection, while the isothermal reflectivity values greater than 30 dBZ were frequently associated strong convection.

A case study from 14 May 2022 in Northwest Arkansas was employed to demonstrate the respective capabilities of TRF1 and TRF2 for identifying and categorizing convection. TRF1 probabilities increased prior to the first observed lightning flash from multiple thunderstorms, and decreased as isothermal reflectivities decreased and lightning production ceased. Pixels classified as strong convection were mostly associated with reflectivity cores and were present when thunderstorms were at the greatest levels of intensity. Two discrete thunderstorms from the case were examined further for validation of the observed trends. TRF1 probabilities and TRF2 classifications responded appropriately for one case with modest rates of convective growth, while for another case with more rapid growth - and subsequent severe weather - the probabilities and classifications were not immediately captured by TRF1 and TRF2 respectively. The results from TRF1 and TRF2 demonstrate the ability of a two-tiered machine learning model to identify and classify convection, however limitations related to sample size, the methods for collecting samples, and the number of available variables may inhibit prognostic applications of each model operationally. Decreased parallax-correction errors in sampling, increasing the sample size of the training data set to reflect the overall thunderstorm climatology for the CONUS, and the inclusion of environmental variables may add more predictive skill to each model tier. At present, the performance of both models and their ability to reinforce key observations in Chapters 2 and 3 demonstrate the opportunity to leverage multi-tiered random forests as a diagnostic tool for severe and local storms research.

5.4 Conclusions

Through the aforementioned studies, lightning flash information from the GOES-R GLM was leveraged to identify trends and signals related to developing convection and severe convection within the Continental United States. Increasing local flash density and decreasing local flash area were associated with signals of increasing convective intensity and the potential to produce severe weather. This was especially the case for regions with clean-IR cloud top brightness temperatures less than 220 K and -10 °C isothermal reflectivity of approximately 50 dBZ. Optical energy signatures were not as robust for intense and severe convection, suggesting reduced potential for their application in convective nowcasting scenarios. However, differences in perspective from the GOES-East and GOES-West GLMs of semi-discrete convection presented differing flash rates and optical energy measurements. When studying developing convection through the GLM's first observed lightning flash, additional GLM flash characteristics and the characteristics of developing convection were revealed. After collecting first flashes across the Continental United States over an entire year, seasonal and localized forcing mechanisms such as low level jets, monsoons, sea breezes, and local topography had a considerable impact on inducing convection and its subsequent lightning production. These regions coincided with increased first flash densities in localized or regional areas depending on the scale of the phenomenon. Corroborating signals from satellite imagery and radar data were also exploited, -10°C isothermal reflectivity values between 35 and 45 dBZ and ABI clean-IR brightness temperatures between 220 and 240 K provided additional thresholds for identifying convection capable of producing lightning. Finally, machine learning methods were employed and posed similar problems related to the identification of convection and the classification of its intensity. The identification and classification of convection were based on GLM lightning flashes, and both tiers of the random forest showed the ability to exploit similar signals from the aforementioned studies to accomplish their tasks. Convection was frequently identified at -10°C isothermal reflectivity values greater than 23 dBZ and clean-IR brightness temperatures of less than 222 K. Similarly, intense convection with more prolific flash rates were identified at -10°C isothermal reflectivity values greater than 31 dBZ. Through this work, the Geostationary Lightning Mapper has shown applications related to short-term convective forecasting for the operational communities, along with its utility to study convection across the Continental United States at key development stages and varying degrees of severity potential.

Reference List

Adler, R. F., M. J. Markus, and D. D. Fenn, 1985: Detection of Severe Midwest Thunderstorms Using Geosynchronous Satellite Data. *Monthly Weather Review*, **113 (5)**, 769 – 781, https://doi.org/10.1175/1520-0493(1985)113⟨0769:DOSMTU⟩2.0.CO;2, URL https://journals.ametsoc.org/view/journals/mwre/113/5/1520-0493_1985_113_0769_dosmtu_2_0_co_2.xml, place: Boston MA, USA Publisher: American Meteorological Society.

Adler, R. F., M. J. Markus, D. D. Fenn, G. Szejwach, and W. E. Shenk, 1983: Thunderstorm Top Structure Observed by Aircraft Overflights with an Infrared Radiometer. *Journal of Applied Meteorology and Climatology*, **22 (4)**, 579 – 593, https://doi.org/10.1175/1520-0450(1983)022⟨0579:TTSOBA⟩2.0.CO;2, URL https://journals.ametsoc.org/view/journals/apme/22/4/1520-0450_1983_022_0579_ttsoba_2_0_co_2.xml, place: Boston MA, USA Publisher: American Meteorological Society.

Baldwin, M. E., and J. S. Kain, 2006: Sensitivity of Several Performance Measures to Displacement Error, Bias, and Event Frequency. *Weather and Forecasting*, **21 (4)**, 636–648, https://doi.org/10.1175/WAF933.1, URL https://journals.ametsoc.org/doi/10.1175/WAF933.1.

Banta, R. M., and C. B. Schaaf, 1987: Thunderstorm Genesis Zones in the Colorado Rocky Mountains as Determined by Traceback of Geosynchronous Satellite Images. *AMS Monthly Weather Review*, **115 (2)**, 463–476, https://doi.org/https://doi.org/10.1175/1520-0493(1987)115%3C0463:TGZITC%3E2.0.CO;2, URL https://journals.ametsoc.org/view/journals/mwre/115/2/1520-0493_1987_115_0463_tgzitc_2_0_co_2.xml?tab_body=abstract-display.

Barnes, L. R., D. M. Schultz, E. C. Gruntfest, M. H. Hayden, and C. C. Benight, 2009: CORRIGENDUM: False Alarm Rate or False Alarm Ratio? *Weather and Forecasting*, **24 (5)**, 1452–1454, https://doi.org/10.1175/2009WAF2222300.1, URL https://journals.ametsoc.org/doi/10.1175/2009WAF2222300.1.

Barth, M. C., and Coauthors, 2015: The Deep Convective Clouds and Chemistry (DC3) Field Campaign. *Bulletin of the American Meteorological Society*, **96 (8)**, 1281–1309, https://doi.org/10.1175/BAMS-D-13-00290.1, URL https://journals.ametsoc.org/doi/10.1175/BAMS-D-13-00290.1.

Bateman, M., D. Mach, and M. Stock, 2021: Further Investigation Into Detection Efficiency and False Alarm Rate for the Geostationary Lightning Mappers Aboard GOES-16 and GOES-17. *Earth and Space Science*, **8 (2)**, https://doi.org/10.1029/2020EA001237, URL https://onlinelibrary.wiley.com/doi/10.1029/2020EA001237.

Bedka, K., J. Brunner, R. Dworak, W. Feltz, J. Otkin, and T. Greenwald, 2010: Objective Satellite-Based Detection of Overshooting Tops Using Infrared Window Channel Brightness Temperature Gradients. *Journal of Applied Meteorology and Climatology*, **49 (2)**, 181–202, https://doi.org/10.1175/2009JAMC2286.1, URL http://journals.ametsoc.org/doi/10.1175/2009JAMC2286.1.

Bedka, K., E. M. Murillo, C. R. Homeyer, B. Scarino, and H. Mersiovsky, 2018: The Above-Anvil Cirrus Plume: An Important Severe Weather Indicator in Visible and Infrared Satellite Imagery. *Weather and Forecasting*, **33 (5)**, 1159–1181, https://doi.org/10.1175/WAF-D-18-0040.1, URL https://journals.ametsoc.org/waf/article/33/5/1159/40741/The-AboveAnvil-Cirrus-Plume-An-Important-Severe.

Blackadar, A. K., 1957: Boundary Layer Wind Maxima and Their Significance for the Growth of Nocturnal Inversions. *Bulletin of the American Meteorological Society*, **38 (5)**, 283–290, https://doi.org/10.1175/1520-0477-38.5.283, URL https://journals.ametsoc.org/doi/10.1175/1520-0477-38.5.283.

Boccippio, D. J., K. L. Cummins, H. J. Christian, and S. J. Goodman, 2001: Combined Satellite- and Surface-Based Estimation of the Intracloud–Cloud-to-Ground Lightning Ratio over the Continental United States. *Monthly Weather Review*, **129 (1)**, 108–122, https://doi.org/10.1175/1520-0493(2001)129⟨0108:CSASBE⟩2.0.CO;2, URL http://journals.ametsoc.org/doi/abs/10.1175/1520-0493%282001%29129%3C0108%3ACSASBE%3E2.0.CO%3B2.

Bonner, W. D., 1968: CLIMATOLOGY OF THE LOW LEVEL JET. *Monthly Weather Review*, **96 (12)**, 833–850, https://doi.org/10.1175/1520-0493(1968)096⟨0833:COTLLJ⟩2.0.CO;2, URL http://journals.ametsoc.org/doi/10.1175/1520-0493(1968)096⟨0833:COTLLJ⟩2.0.CO;2.

Breiman, L., 2001: Random Forests. *Machine Learning*, **45 (1)**, 5–32, https://doi.org/10.1023/A:1010933404324, URL https://doi.org/10.1023/A:1010933404324.

Breiman, L., J. Friedman, C. Stone, and R. Olshen, 1984: *Classification and Regression Trees*. Taylor & Francis, URL https://books.google.com/books?id=JwQx-WOmSyQC.

Bruning, E. C., 2019: glmtools. *Zenodo*, https://doi.org/10.5281/zenodo.2648658, URL https://doi.org/10.5281/zenodo.2648658.

Bruning, E. C., and P. M. Bitzer, 2023: Characterizing GLM Data Quality. Virtual, URL https://vimeo.com/885245333/0a815d127b?ts=3367000&share=copy.

Bruning, E. C., and D. R. MacGorman, 2013: Theory and Observations of Controls on Lightning Flash Size Spectra. *Journal of the Atmospheric Sciences*, **70 (12)**, 4012–4029, https://doi.org/10.1175/JAS-D-12-0289.1, URL http://journals.ametsoc.org/doi/10.1175/JAS-D-12-0289.1.

Bruning, E. C., and Coauthors, 2019: Meteorological Imagery for the Geostationary Lightning Mapper. *Journal of Geophysical Research: Atmospheres*, **124 (24)**, 14 285–14 309, https://doi.org/10.1029/2019JD030874, URL https://onlinelibrary.wiley.com/doi/abs/10.1029/2019JD030874.

Brunner, K. N., and P. M. Bitzer, 2020: A First Look at Cloud Inhomogeneity and Its Effect on Lightning Optical Emission. *Geophysical Research Letters*, **47 (10)**, https://doi.org/10.1029/2020GL087094, URL https://onlinelibrary.wiley.com/doi/abs/10.1029/2020GL087094.

Buechler, D. E., and S. J. Goodman, 1990: Echo Size and Asymmetry: Impact on NEXRAD Storm Identification. *Journal of Applied Meteorology and Climatology*, **29**, 962–969, https://doi.org/https://doi.org/10.1175/1520-0450(1990)029⟨0962:ESAAIO⟩2.0.CO;2.

Bunkers, M. J., B. A. Klimowski, J. W. Zeitler, R. L. Thompson, and M. L. Weisman, 2000: Predicting Supercell Motion Using a New Hodograph Technique. *Weather and Forecasting*, **15 (1)**, 61–79, https://doi.org/10.1175/1520-0434(2000)015⟨0061:PSMUAN⟩2.0.CO;2, URL http://journals.ametsoc.org/doi/10.1175/1520-0434(2000)015⟨0061:PSMUAN⟩2.0.CO;2.

Bureau, U. C., 2021: State Area Measurements and Internal Point Coordinates. URL https://www.census.gov/geographies/reference-files/2010/geo/state-area.html.

Byers, H. R., and H. R. Rodebush, 1948: Causes of Thunderstorms of the Florida Peninsula. *Journal of Meteorology*, **5**, 275–280, https://doi.org/https://doi.org/10.1175/1520-0469(1948)005⟨0275:COTOTF⟩2.0.CO;2.

Calhoun, K. M., 2018: Feedback and Recommendations for the Geostationary Lightning Mapper (GLM) in Severe and Hazardous Weather Forecasting and Warning Operations. Tech. rep., GOES Proving Ground, 15 pp.

Calhoun, K. M., 2019: Feedback and Recommendations for the Geostationary Lightning Mapper (GLM) in Severe and Hazardous Weather Forecasting and Warning Operations. Tech. rep., GOES Proving Ground, 16 pp.

Calhoun, K. M., K. L. Berry, D. M. Kingfield, T. Meyer, M. J. Krocak, T. M. Smith, G. Stumpf, and A. Gerard, 2021: The Experimental Warning Program of NOAA's Hazardous Weather Testbed. *Bulletin of the American Meteorological Society*, 1–51, https://doi.org/10.1175/BAMS-D-21-0017.1, URL https://journals.ametsoc.org/view/journals/bams/aop/BAMS-D-21-0017.1/BAMS-D-21-0017.1.xml.

Calhoun, K. M., E. C. Bruning, and C. J. Schultz, 2018: Principles and Operational Applications of Geostationary Lightning Mapper Data for Severe and Local Storms. Stowe, VT, URL https://ams.confex.com/ams/29SLS/videogateway.cgi/id/49342?recordingid=49342&uniqueid=Paper348316&entry_password=824513.

Calhoun, K. M., D. R. MacGorman, C. L. Ziegler, and M. I. Biggerstaff, 2013: Evolution of Lightning Activity and Storm Charge Relative to Dual-Doppler Analysis of a High-Precipitation Supercell Storm. *Monthly Weather Review*, **141 (7)**, 2199–2223, https://doi.org/10.1175/MWR-D-12-00258.1, URL http://journals.ametsoc.org/doi/10.1175/MWR-D-12-00258.1.

Calhoun, K. M., E. R. Mansell, D. R. MacGorman, and D. C. Dowell, 2014: Numerical Simulations of Lightning and Storm Charge of the 29–30 May 2004 Geary, Oklahoma, Supercell Thunderstorm Using EnKF Mobile Radar Data Assimilation. *Monthly Weather Review*, **142 (11)**, 3977–3997, https://doi.org/10.1175/MWR-D-13-00403.1, URL http://journals.ametsoc.org/doi/10.1175/MWR-D-13-00403.1.

Carbin, G., and Coauthors, 2000: SPC Severe Weather Events Archive. URL https://www.spc.noaa.gov/exper/archive/events/.

Carey, L. D., and S. A. Rutledge, 2000: The Relationship between Precipitation and Lightning in Tropical Island Convection: A C-Band Polarimetric Radar Study. *Monthly Weather Review*, **128**, 24.

Carey, L. D., E. V. Schultz, C. J. Schultz, W. Deierling, W. A. Petersen, A. L. Bain, and K. E. Pickering, 2019: An Evaluation of Relationships between Radar-Inferred Kinematic and Microphysical Parameters and Lightning Flash Rates in Alabama Storms. *Atmosphere*, **10 (12)**, 796, https://doi.org/10.3390/atmos10120796, URL https://www.mdpi.com/2073-4433/10/12/796.

Chmielewski, V. C., J. Blair, D. Kennedy, D. MacGorman, and K. M. Calhoun, 2022a: A Comparison of Processing Methods for the Oklahoma Lightning Mapping Array. *Earth and Space Science*, **9 (7)**, e2021EA002 081, https://doi.org/10.1029/2021EA002081, URL https://agupubs.onlinelibrary.wiley.com/doi/10.1029/2021EA002081.

Chmielewski, V. C., and E. C. Bruning, 2016: Lightning Mapping Array flash detection performance with variable receiver thresholds. *Journal of Geophysical Research*, 15.

Chmielewski, V. C., K. M. Calhoun, D. Kennedy, Z. Barney, V. Salinas, J. Ringhausen, E. C. Bruning, and K. N. Brunner, 2022b: PERiLS_2022: NSSL Deployable Lightning Mapping Array Data. UCAR/NCAR - Earth Observing Laboratory, URL https://data.eol.ucar.edu/dataset/610.006, https://doi.org/https://doi.org/10.26023/R0K6-AXR5-YZ00.

Cintineo, J. L., M. J. Pavolonis, and J. M. Sieglaff, 2022: ProbSevere LightningCast: A Deep-Learning Model for Satellite-Based Lightning Nowcasting. *Weather and Forecasting*, **37 (7)**, 1239–1257, https://doi.org/10.1175/WAF-D-22-0019.1, URL https://journals.ametsoc.org/view/journals/wefo/37/7/WAF-D-22-0019.1.xml.

Cintineo, J. L., M. J. Pavolonis, and J. M. Sieglaff, 2024: ProbSevere Version 3: Improved Exploitation of Data Fusion and Machine Learning for Nowcasting Severe Weather. *Weather and Forecasting*, **39 (12)**, 1937–1958, https://doi.org/10.1175/WAF-D-24-0076.1, URL https://journals.ametsoc.org/view/journals/wefo/39/12/WAF-D-24-0076.1.xml.

Cintineo, J. L., M. J. Pavolonis, J. M. Sieglaff, L. Cronce, and J. Brunner, 2020a: NOAA ProbSevere v2.0?ProbHail, ProbWind, and ProbTor. *Weather and Forecasting*, **35 (4)**, 1523 – 1543, https://doi.org/10.1175/WAF-D-19-0242.1, URL https://journals.ametsoc.org/view/journals/wefo/35/4/wafD190242.xml, place: Boston MA, USA Publisher: American Meteorological Society.

Cintineo, J. L., M. J. Pavolonis, J. M. Sieglaff, A. Wimmers, J. Brunner, and W. Bellon, 2020b: A Deep-Learning Model for Automated Detection of Intense Midlatitude Convection Using Geostationary Satellite Images. *Weather and Forecasting*, **35 (6)**, 2567 – 2588, https://doi.org/10.1175/WAF-D-20-0028.1, URL https://journals.ametsoc.org/view/journals/wefo/35/6/waf-d-20-0028.1.xml, place: Boston MA, USA Publisher: American Meteorological Society.

Coniglio, M. C., J. Y. Hwang, and D. J. Stensrud, 2010: Environmental Factors in the Upscale Growth and Longevity of MCSs Derived from Rapid Update Cycle Analyses. *Monthly Weather Review*, **138 (9)**, 3514–3539, https://doi.org/10.1175/2010MWR3233.1, URL http://journals.ametsoc.org/doi/10.1175/2010MWR3233.1.

Cummins, K. L., 2020: Deriving GLM Group and Flash Detection Efficiencies from Measurable GLM Thresholds. Virtual, URL https://goes-r.nsstc.nasa.gov/home/sites/default/files/2020-09/300_Cummins2020_GLM_DE_Rel%20LMA_TRMM-LIS_small.pdf.

Cummins, K. L., and M. J. Murphy, 2009: An Overview of Lightning Locating Systems: History, Techniques, and Data Uses, With an In-Depth Look at the U.S. NLDN. *IEEE Transactions on Electromagnetic Compatibility*, **51 (3)**, 499–518, https://doi.org/10.1109/TEMC.2009.2023450, URL http://ieeexplore.ieee.org/document/5173582/.

DiGangi, E. A., M. Stock, and J. Lapierre, 2022: Thunder Hours: How Old Methods Offer New Insights into Thunderstorm Climatology. *Bulletin of the American Meteorological Society*, **103 (2)**, E548–E569, https://doi.org/10.1175/BAMS-D-20-0198.1, URL https://journals.ametsoc.org/view/journals/bams/103/2/BAMS-D-20-0198.1.xml.

Elsenheimer, C. B., and C. M. Gravelle, 2019: Introducing Lightning Threat Messaging Using the GOES-16 Day Cloud Phase Distinction RGB Composite. *Weather and Forecasting*, WAF–D–19–0049.1, https://doi.org/10.1175/WAF-D-19-0049.1, URL http://journals.ametsoc.org/doi/10.1175/WAF-D-19-0049.1.

Emersic, C., and C. Saunders, 2010: Further laboratory investigations into the Relative Diffusional Growth Rate theory of thunderstorm electrification. *Atmospheric Research*, **98 (2-4)**, 327–340, https://doi.org/10.1016/j.atmosres.2010.07.011, URL https://linkinghub.elsevier.com/retrieve/pii/S0169809510001869.

Flournoy, M. D., M. C. Coniglio, and E. N. Rasmussen, 2021: Examining Relationships between Environmental Conditions and Supercell Motion in Time. *Weather and Forecasting*, **36 (3)**, 737–755, https://doi.org/10.1175/WAF-D-20-0192.1, URL https://journals.ametsoc.org/view/journals/wefo/36/3/WAF-D-20-0192.1.xml.

Fuchs, B. R., and Coauthors, 2015: Environmental controls on storm intensity and charge structure in multiple regions of the continental United States. *Journal of Geophysical Research: Atmospheres*, **120 (13)**, 6575–6596, https://doi.org/10.1002/2015JD023271, URL https://agupubs.onlinelibrary.wiley.com/doi/10.1002/2015JD023271.

Goodman, S. J., D. Mach, W. Koshak, and R. Blakeslee, 2012: GLM Lightning Cluster-Filter Algorithm. NOAA/NESDIS, URL https://www.star.nesdis.noaa.gov/goesr/documents/ATBDs/Baseline/ATBD_GOES-R_GLM_v3.0_Jul2012.pdf.

Goodman, S. J., and Coauthors, 2013: The GOES-R Geostationary Lightning Mapper (GLM). *Atmospheric Research*, **125-126**, 34–49, https://doi.org/10.1016/j.atmosres.2013.01.006, URL https://linkinghub.elsevier.com/retrieve/pii/S0169809513000434.

Greene, D. R., and R. A. Clark, 1972: Vertically Integrated Liquid Water—A New Analysis Tool. *Monthly Weather Review*, **100 (7)**, 548–552, https://doi.org/10.1175/1520-0493(1972)100⟨0548:VILWNA⟩2.3.CO;2, URL http://journals.ametsoc.org/doi/abs/10.1175/1520-0493%281972%29100%3C0548%3AVILWNA%3E2.3.CO%3B2.

Gremillion, M. S., and R. E. Orville, 1999: Thunderstorm Characteristics of Cloud-to-Ground Lightning at the Kennedy Space Center, Florida: A Study of Lightning Initiation Signatures as Indicated by the WSR-88D. *Weather and Forecasting*, **14 (5)**, 640–649, https://doi.org/10.1175/1520-0434(1999)014⟨0640:TCOCTG⟩2.0.CO;2, URL http://journals.ametsoc.org/doi/abs/10.1175/1520-0434%281999%29014%3C0640%3ATCOCTG%3E2.0.CO%3B2.

Géron, A., 2019: *Hands-On Machine Learning with Scikit-Learn, Keras & Tensorflow*. 2nd ed., O'Reilly.

Harrison, D. R., M. S. Elliott, I. L. Jirak, and P. T. Marsh, 2022: Utilizing the High-Resolution Ensemble Forecast System to Produce Calibrated Probabilistic Thunderstorm Guidance. *Weather and Forecasting*, **37 (7)**, 1103–1115, https://doi.org/10.1175/WAF-D-22-0001.1, URL https://journals.ametsoc.org/view/journals/wefo/37/7/WAF-D-22-0001.1.xml.

Heidinger, A., 2013: Algorithm Theoretical Basis Document ABI Cloud Height. NOAA/NESDIS, URL https://www.star.nesdis.noaa.gov/goesr/docs/ATBD/Cloud_Height.pdf.

Heidinger, A., and W. Straka, 2013: Algorithm Theoretical Basis Document ABI Cloud Mask. NOAA/NESDIS, URL https://www.star.nesdis.noaa.gov/goesr/docs/ATBD/Cloud_Mask.pdf.

Higgins, R. W., Y. Chen, and A. V. Douglas, 1999: Interannual Variability of the North American Warm Season Precipitation Regime. *Journal of Climate*, **12 (3)**, 653–680, https://doi.org/10.1175/1520-0442(1999)012⟨0653:IVOTNA⟩2.0.CO;2, URL http://journals.ametsoc.org/doi/10.1175/1520-0442(1999)012⟨0653:IVOTNA⟩2.0.CO;2.

Hilburn, K. A., I. Ebert-Uphoff, and S. D. Miller, 2021: Development and Interpretation of a Neural-Network-Based Synthetic Radar Reflectivity Estimator Using GOES-R Satellite Observations. *Journal of Applied Meteorology and Climatology*, **60 (1)**, 3–21, https://doi.org/10.1175/JAMC-D-20-0084.1, URL https://journals.ametsoc.org/view/journals/apme/60/1/jamc-d-20-0084.1.xml.

Hodanish, S., D. Sharp, W. Collins, C. Paxton, and R. E. Orville, 1997: A 10-yr Monthly Lightning Climatology of Florida: 1986–95. *WEATHER AND FORECASTING*, **12**, 10.

Holmlund, K., and Coauthors, 2021: Meteosat Third Generation (MTG): Continuation and Innovation of Observations from Geostationary Orbit. *Bulletin of the American Meteorological Society*, **102 (5)**, E990–E1015, https://doi.org/10.1175/BAMS-D-19-0304.1, URL https://journals.ametsoc.org/view/journals/bams/102/5/BAMS-D-19-0304.1.xml.

Hondl, K. D., and M. D. Eilts, 1994: Doppler Radar Signatures of Developing Thunderstorms and Their Potential to Indicate the Onset of Cloud-to-Ground Lightning. *Monthly Weather Review*, **122**, 1818–1836, https://doi.org/https://doi.org/10.1175/1520-0493(1994)122⟨1818:DRSODT⟩2.0.CO;2.

Houze, R. A., 2004: Mesoscale Convective Systems. *Reviews of Geophysics*, **42 (4)**, https://doi.org/10.1029/2004RG000150, URL http://doi.wiley.com/10.1029/2004RG000150.

Hsu, S.-A., 1970: COASTAL AIR-CIRCULATION SYSTEM: OBSERVATIONS AND EMPIRICAL MODEL. *Monthly Weather Review*, **98 (7)**, 487–509, https://doi.org/10.1175/1520-0493(1970)098⟨0487:CACSOA⟩2.3.CO;2, URL http://journals.ametsoc.org/doi/10.1175/1520-0493(1970)098⟨0487:CACSOA⟩2.3.CO;2.

Karstens, C. D., and Coauthors, 2018: Development of a Human–Machine Mix for Forecasting Severe Convective Events. *Weather and Forecasting*, **33 (3)**, 715–737, https://doi.org/10.1175/WAF-D-17-0188.1, URL https://journals.ametsoc.org/doi/10.1175/WAF-D-17-0188.1.

Kelly, D. L., J. T. Schaefer, and C. A. Doswell, 1985: Climatology of Nontornadic Severe Thunderstorm Events in the United States. *Monthly Weather Review*, **113**, 1997–2014, https://doi.org/https://doi.org/10.1175/1520-0493(1985)113⟨1997:CONSTE⟩2.0.CO;2.

Kirshbaum, D., B. Adler, N. Kalthoff, C. Barthlott, and S. Serafin, 2018: Moist Orographic Convection: Physical Mechanisms and Links to Surface-Exchange Processes. *Atmosphere*, **9 (3)**, 80, https://doi.org/10.3390/atmos9030080, URL https://www.mdpi.com/2073-4433/9/3/80.

Kosiba, K. A., and Coauthors, 2024: The Propagation, Evolution, and Rotation in Linear Storms (PERiLS) Project. *Bulletin of the American Meteorological Society*, **105 (10)**, E1768–E1799, https://doi.org/10.1175/BAMS-D-22-0064.1, URL https://journals.ametsoc.org/view/journals/bams/105/10/BAMS-D-22-0064.1.xml.

Kuhlman, K. M., D. R. MacGorman, M. I. Biggerstaff, and P. R. Krehbiel, 2009: Lightning initiation in the anvils of two supercell storms. *Geophysical Research Letters*, **36 (7)**, n/a–n/a, https://doi.org/10.1029/2008GL036650, URL http://doi.wiley.com/10.1029/2008GL036650.

Lagerquist, R., J. Q. Stewart, I. Ebert-Uphoff, and C. Kumler, 2021: Using Deep Learning to Nowcast the Spatial Coverage of Convection from Himawari-8 Satellite Data. *Monthly Weather Review*, **149 (12)**, 3897–3921, https://doi.org/10.1175/MWR-D-21-0096.1, URL https://journals.ametsoc.org/view/journals/mwre/149/12/MWR-D-21-0096.1.xml.

Lakshmanan, V., T. Smith, K. Hondl, G. J. Stumpf, and A. Witt, 2006: A Real-Time, Three-Dimensional, Rapidly Updating, Heterogeneous Radar Merger Technique for Reflectivity, Velocity, and Derived Products. *Weather and Forecasting*, **21 (5)**, 802–823, https://doi.org/10.1175/WAF942.1, URL http://journals.ametsoc.org/doi/abs/10.1175/WAF942.1.

Light, T. E., D. M. Suszcynsky, M. W. Kirkland, and A. R. Jacobson, 2001: Simulations of lightning optical waveforms as seen through clouds by satellites. *Journal of Geophysical Research: Atmospheres*, **106 (D15)**, 17 103–17 114, https://doi.org/10.1029/2001JD900051, URL http://doi.wiley.com/10.1029/2001JD900051.

Lindsey, D. T., and Coauthors, 2024: GeoXO: NOAA's Future Geostationary Satellite System. *Bulletin of the American Meteorological Society*, **105 (3)**, E660–E679, https://doi.org/10.1175/BAMS-D-23-0048.1, URL https://journals.ametsoc.org/view/journals/bams/105/3/BAMS-D-23-0048.1.xml.

MacGorman, D. R., A. A. Few, and T. L. Teer, 1981: Layered lightning activity. *Journal of Geophysical Research*, **86 (C10)**, 9900, https://doi.org/10.1029/JC086iC10p09900, URL http://doi.wiley.com/10.1029/JC086iC10p09900.

MacGorman, D. R., and Coauthors, 2008: TELEX The Thunderstorm Electrification and Lightning Experiment. *Bulletin of the American Meteorological Society*, **89 (7)**, 997–1014, https://doi.org/10.1175/2007BAMS2352.1, URL http://journals.ametsoc.org/doi/10.1175/2007BAMS2352.1.

Mahalik, M. C., B. R. Smith, K. L. Elmore, D. M. Kingfield, K. L. Ortega, and T. M. Smith, 2019: Estimates of Gradients in Radar Moments Using a Linear Least Squares Derivative Technique. *Weather and Forecasting*, **34 (2)**, 415–434, https://doi.org/10.1175/WAF-D-18-0095.1, URL https://journals.ametsoc.org/doi/10.1175/WAF-D-18-0095.1.

Makowski, J. A., D. R. MacGorman, M. I. Biggerstaff, and W. H. Beasley, 2013: Total Lightning Characteristics Relative to Radar and Satellite Observations of Oklahoma Mesoscale Convective Systems. *Monthly Weather Review*, **141 (5)**, 1593–1611, https://doi.org/10.1175/MWR-D-11-00268.1, URL http://journals.ametsoc.org/doi/10.1175/MWR-D-11-00268.1.

Maneewongvatana, S., and D. M. Mount, 1999: Analysis of approximate nearest neighbor searching with clustered point sets. Baltimore, MD, URL https://doi.org/10.48550/arXiv.cs/9901013, _eprint: cs/9901013.

Manzato, A., S. Serafin, M. M. Miglietta, D. Kirshbaum, and W. Schulz, 2022: A Pan-Alpine Climatology of Lightning and Convective Initiation. *Monthly Weather Review*, **150 (9)**, 2213–2230, https://doi.org/10.1175/MWR-D-21-0149.1, URL https://journals.ametsoc.org/view/journals/mwre/150/9/MWR-D-21-0149.1.xml.

Markowski, P., 2007: Convective Storm Initiation and Organization. *Atmospheric Convection: Research and Operational Forecasting Aspects*, Vol. 475, Springer Vienna, Vienna, 23–28, https://doi.org/10.1007/978-3-211-69291-2_4, URL http://link.springer.com/10.1007/978-3-211-69291-2_4, series Title: CISM International Centre for Mechanical Sciences.

Mecikalski, R. M., and L. D. Carey, 2018: Radar Reflectivity and Altitude Distributions of Lightning Flashes as a Function of Three Main Storm Types. *Journal of Geophysical Research: Atmospheres*, **123 (22)**, https://doi.org/10.1029/2018JD029238, URL https://onlinelibrary.wiley.com/doi/abs/10.1029/2018JD029238.

Mosier, R. M., C. Schumacher, R. E. Orville, and L. D. Carey, 2011: Radar Nowcasting of Cloud-to-Ground Lightning over Houston, Texas. *Weather and Forecasting*, **26 (2)**, 199–212, https://doi.org/10.1175/2010WAF2222431.1, URL http://journals.ametsoc.org/doi/abs/10.1175/2010WAF2222431.1.

Murphy, A. M., C. R. Homeyer, and K. Q. Allen, 2023: Development and Investigation of GridRad-Severe, a Multiyear Severe Event Radar Dataset. *Monthly Weather Review*, **151 (9)**, 2257–2277, https://doi.org/10.1175/MWR-D-23-0017.1, URL https://journals.ametsoc.org/view/journals/mwre/151/9/MWR-D-23-0017.1.xml.

Murphy, M. J., and R. K. Said, 2020: Comparisons of Lightning Rates and Properties From the U.S. National Lightning Detection Network (NLDN) and GLD360 With GOES-16 Geostationary Lightning Mapper and Advanced Baseline Imager Data. *Journal of Geophysical Research: Atmospheres*, **125 (5)**, https://doi.org/10.1029/2019JD031172, URL https://onlinelibrary.wiley.com/doi/abs/10.1029/2019JD031172.

NWS Phoenix, A., 2023: Review of the 2022 Monsoon Across the Southwest U.S. URL https://www.weather.gov/psr/2022MonsoonReview.

Ortland, S. M., M. J. Pavolonis, and J. L. Cintineo, 2023: The Development and Initial Capabilities of ThunderCast, a Deep Learning Model for Thunderstorm Nowcasting in the United States. *Artificial Intelligence for the Earth Systems*, **2 (4)**, e230 044, https://doi.org/10.1175/AIES-D-23-0044.1, URL https://journals.ametsoc.org/view/journals/aies/2/4/AIES-D-23-0044.1.xml.

Parker, M. D., and R. H. Johnson, 2000: Organizational Modes of Midlatitude Mesoscale Convective Systems. *Monthly Weather Review*, **128 (10)**, 3413–3436, https://doi.org/10.1175/1520-0493(2001)129⟨3413:OMOMMC⟩2.0.CO;2, URL http://journals.ametsoc.org/doi/10.1175/1520-0493(2001)129⟨3413:OMOMMC⟩2.0.CO;2.

Petersen, D., and W. H. Beasley, 2013: High-speed video observations of a natural negative stepped leader and subsequent dart-stepped leader. *Journal of Geophysical Research: Atmospheres*\, **118 (21)**, 12,110–12,119, https://doi.org/https://doi.org/10.1002/2013JD019910, URL https://agupubs.onlinelibrary.wiley.com/doi/10.1002/2013JD019910.

Peterson, M., 2019: Research Applications for the Geostationary Lightning Mapper Operational Lightning Flash Data Product. *Journal of Geophysical Research: Atmospheres*, **124 (17-18)**, 10 205–10 231, https://doi.org/10.1029/2019JD031054, URL https://onlinelibrary.wiley.com/doi/abs/10.1029/2019JD031054.

Peterson, M., 2020: Modeling the Transmission of Optical Lightning Signals Through Complex 3-D Cloud Scenes. *Journal of Geophysical Research: Atmospheres*, **125 (23)**, https://doi.org/10.1029/2020JD033231, URL https://onlinelibrary.wiley.com/doi/10.1029/2020JD033231.

Peterson, M., 2021: Holes in Optical Lightning Flashes: Identifying Poorly Transmissive Clouds in Lightning Imager Data. *Earth and Space Science*, **8 (2)**, https://doi.org/10.1029/2020EA001294, URL https://onlinelibrary.wiley.com/doi/10.1029/2020EA001294.

Peterson, M., S. Rudlosky, and D. Zhang, 2020: Changes to the Appearance of Optical Lightning Flashes Observed From Space According to Thunderstorm Organization and Structure. *Journal of Geophysical Research: Atmospheres*, **125 (4)**, https://doi.org/10.1029/2019JD031087, URL https://onlinelibrary.wiley.com/doi/abs/10.1029/2019JD031087.

Potvin, C. K., C. Broyles, P. S. Skinner, H. E. Brooks, and E. Rasmussen, 2019: A Bayesian Hierarchical Modeling Framework for Correcting Reporting Bias in the U.S. Tornado Database. *Weather and Forecasting*, **34 (1)**, 15–30, https://doi.org/10.1175/WAF-D-18-0137.1, URL http://journals.ametsoc.org/doi/10.1175/WAF-D-18-0137.1.

Raspaud, M., and Coauthors, 2022: pytroll/satpy: Version 0.36.0 (2022/04/14). Zenodo, URL https://doi.org/10.5281/zenodo.6460193, https://doi.org/10.5281/zenodo.6460193.

Reif, D. W., and H. B. Bluestein, 2017: A 20-Year Climatology of Nocturnal Convection Initiation over the Central and Southern Great Plains during the Warm Season. *Monthly Weather Review*, **145 (5)**, 1615–1639, https://doi.org/10.1175/MWR-D-16-0340.1, URL http://journals.ametsoc.org/doi/10.1175/MWR-D-16-0340.1.

Reynolds, D. W., 1980: Observations of Damaging Hailstorms from Geosynchronous Satellite Digital Data. *Monthly Weather Review*, **108**, 337–348, https://doi.org/https://doi.org/10.1175/1520-0493(1980)108⟨0337:OODHFG⟩2.0.CO;2.

Ringhausen, J., P. Bitzer, W. Koshak, and J. Mecikalski, 2021: Classification of GLM Flashes Using Random Forests. *Earth and Space Science*, **8 (11)**, https://doi.org/10.1029/2021EA001861, URL https://onlinelibrary.wiley.com/doi/10.1029/2021EA001861.

Rison, W., R. J. Thomas, P. R. Krehbiel, T. Hamlin, and J. Harlin, 1999: A GPS-based three-dimensional lightning mapping system: Initial observations in central New Mexico. *Geophysical Research Letters*, **26 (23)**, 3573–3576, https://doi.org/10.1029/1999GL010856, URL http://doi.wiley.com/10.1029/1999GL010856.

Roberts, R. D., and S. Rutledge, 2003: Nowcasting Storm Initiation and Growth Using GOES-8 and WSR-88D Data. *Weather and Forecasting*, **18**, 23, https://doi.org/https://doi.org/10.1175/1520-0434(2003)018⟨0562:NSIAGU⟩2.0.CO;2.

Roebber, P. J., 2009: Visualizing Multiple Measures of Forecast Quality. *Weather and Forecasting*, **24 (2)**, 601–608, https://doi.org/10.1175/2008WAF2222159.1, URL https://journals.ametsoc.org/doi/10.1175/2008WAF2222159.1.

Rotunno, R., and J. B. Klemp, 1982: The Influence of the Shear-Induced Pressure Gradient on Thunderstorm Motion. *Monthly Weather Review*, **110 (2)**, 136 – 151, https://doi.org/10.1175/1520-0493(1982)110⟨0136:TIOTSI⟩2.0.CO;2, URL https://journals.ametsoc.org/view/journals/mwre/110/2/1520-0493_1982_110_0136_tiotsi_2_0_co_2.xml, place: Boston MA, USA Publisher: American Meteorological Society.

Rudlosky, S., 2015: Evaluating ENTLN performance relative to TRMM/LIS. *Journal of Operational Meteorology*, **3 (2)**, 11–20, https://doi.org/10.15191/nwajom.2015.0302, URL http://nwafiles.nwas.org/jom/articles/2015/2015-JOM2/2015-JOM2.pdf.

Rudlosky, S., S. J. Goodman, K. M. Calhoun, C. J. Schultz, A. Back, B. Kuligowski, S. Stephenson, and C. M. Gravelle, 2020: Geostationary Lightning Mapper Value Assessment. Tech. rep. URL https://repository.library.noaa.gov/view/noaa/27429, publisher: United States. National Environmental Satellite, Data, and Information Service.

Rudlosky, S. D., S. J. Goodman, W. J. Koshak, R. J. Blakeslee, D. E. Buechler, D. M. Mach, and M. Bateman, 2017: Characterizing the GOES-R (GOES-16) Geostationary Lightning Mapper (GLM) on-orbit performance. *2017 IEEE International Geoscience and Remote Sensing Symposium (IGARSS)*, IEEE, Fort Worth, TX, 279–282, https://doi.org/10.1109/IGARSS.2017.8126949, URL http://ieeexplore.ieee.org/document/8126949/.

Rudlosky, S. D., S. J. Goodman, K. S. Virts, and E. C. Bruning, 2019: Initial Geostationary Lightning Mapper Observations. *Geophysical Research Letters*, **46 (2)**, 1097–1104, https://doi.org/10.1029/2018GL081052, URL http://doi.wiley.com/10.1029/2018GL081052.

Rudlosky, S. D., and K. S. Virts, 2021: Dual Geostationary Lightning Mapper Observations. *Monthly Weather Review*, **149 (4)**, 979–998, https://doi.org/10.1175/MWR-D-20-0242.1, URL https://journals.ametsoc.org/view/journals/mwre/149/4/MWR-D-20-0242.1.xml.

Rutledge, S. A., K. A. Hilburn, A. Clayton, B. Fuchs, and S. D. Miller, 2020: Evaluating Geostationary Lightning Mapper Flash Rates Within Intense Convective Storms. *Journal of Geophysical Research: Atmospheres*, **125 (14)**, https://doi.org/10.1029/2020JD032827, URL https://onlinelibrary.wiley.com/doi/abs/10.1029/2020JD032827.

Sandmæl, T. N., C. R. Homeyer, K. M. Bedka, J. M. Apke, J. R. Mecikalski, and K. Khlopenkov, 2019: Evaluating the Ability of Remote Sensing Observations to Identify Significantly Severe and Potentially Tornadic

Storms. *Journal of Applied Meteorology and Climatology*, **58 (12)**, 2569–2590, https://doi.org/10.1175/JAMC-D-18-0241.1, URL http://journals.ametsoc.org/doi/10.1175/JAMC-D-18-0241.1.

Sandmæl, T. N., B. R. Smith, J. G. Madden, J. W. Monroe, P. T. Hyland, B. A. Schenkel, and T. C. Meyer, 2023: The 2021 Hazardous Weather Testbed Experimental Warning Program Radar Convective Applications Experiment: A Forecaster Evaluation of the Tornado Probability Algorithm and the New Mesocyclone Detection Algorithm. *Weather and Forecasting*, **38 (7)**, 1125–1142, https://doi.org/10.1175/WAF-D-23-0042.1, URL https://journals.ametsoc.org/view/journals/wefo/38/7/WAF-D-23-0042.1.xml.

Sasaki, Y., 2007: The truth of the F-measure.

Schmit, T., M. Gunshor, G. Fu, T. Rink, K. Bah, W. Zhang, and W. Wolf, 2012: GOES-R Advanced Baseline Imager (ABI) Algorithm Theoretical Basis Document For Cloud and Moisture Imagery Product (CMIP). NOAA/NESDIS.

Schmit, T. J., P. Griffith, M. M. Gunshor, J. M. Daniels, S. J. Goodman, and W. J. Lebair, 2017: A Closer Look at the ABI on the GOES-R Series. *Bulletin of the American Meteorological Society*, **98 (4)**, 681–698, https://doi.org/10.1175/BAMS-D-15-00230.1, URL http://journals.ametsoc.org/doi/10.1175/BAMS-D-15-00230.1.

Schultz, C. J., L. D. Carey, E. V. Schultz, and R. J. Blakeslee, 2015: Insight into the Kinematic and Microphysical Processes that Control Lightning Jumps. *Weather and Forecasting*, **30 (6)**, 1591–1621, https://doi.org/10.1175/WAF-D-14-00147.1, URL http://journals.ametsoc.org/doi/10.1175/WAF-D-14-00147.1.

Schultz, C. J., L. D. Carey, E. V. Schultz, and R. J. Blakeslee, 2017: Kinematic and Microphysical Significance of Lightning Jumps versus Nonjump Increases in Total Flash Rate. *Weather and Forecasting*, **32 (1)**, 275–288, https://doi.org/10.1175/WAF-D-15-0175.1, URL http://journals.ametsoc.org/doi/10.1175/WAF-D-15-0175.1.

Schultz, C. J., W. A. Petersen, and L. D. Carey, 2009: Preliminary Development and Evaluation of Lightning Jump Algorithms for the Real-Time Detection of Severe Weather. *Journal of Applied Meteorology and Climatology*, **48 (12)**, 2543–2563, https://doi.org/10.1175/2009JAMC2237.1, URL http://journals.ametsoc.org/doi/10.1175/2009JAMC2237.1.

Schultz, C. J., W. A. Petersen, and L. D. Carey, 2011: Lightning and Severe Weather: A Comparison between Total and Cloud-to-Ground Lightning Trends. *Weather and Forecasting*, **26 (5)**, 744–755, https://doi.org/10.1175/WAF-D-10-05026.1, URL https://journals.ametsoc.org/doi/10.1175/WAF-D-10-05026.1.

Shield, S. A., and A. L. Houston, 2024: Spatiotemporal characteristics of deep convection initiation in the Central United States. *International Journal of Climatology*, **44 (8)**, 2636–2649, https://doi.org/10.1002/joc.8472, URL https://rmets.onlinelibrary.wiley.com/doi/10.1002/joc.8472.

Smith, T. M., and Coauthors, 2016: Multi-Radar Multi-Sensor (MRMS) Severe Weather and Aviation Products: Initial Operating Capabilities. *Bulletin of the American Meteorological Society*, **97 (9)**, 1617–1630, https://doi.org/10.1175/BAMS-D-14-00173.1, URL http://journals.ametsoc.org/doi/10.1175/BAMS-D-14-00173.1.

Stensrud, D. J., 1996: Importance of Low-Level Jets to Climate: A Review. *AMS Journal of Climate*, **9 (8)**, 1698–1711, https://doi.org/https://doi.org/10.1175/1520-0442(1996)009⟨1698:IOLLJT⟩2.0.CO;2.

Stolzenburg, M., T. C. Marshall, and P. R. Krehbiel, 2015: Initial electrification to the first lightning flash in New Mexico thunderstorms. *Journal of Geophysical Research: Atmospheres*, **120 (21)**, 11,253–11,276, https://doi.org/10.1002/2015JD023988, URL http://doi.wiley.com/10.1002/2015JD023988.

Stough, S. M., L. D. Carey, C. J. Schultz, and P. M. Bitzer, 2017: Investigating the Relationship between Lightning and Mesocyclonic Rotation in Supercell Thunderstorms. *Weather and Forecasting*, **32 (6)**, 2237–2259, https://doi.org/10.1175/WAF-D-17-0025.1, URL http://journals.ametsoc.org/doi/10.1175/WAF-D-17-0025.1.

Stough, S. M., V. C. Chmielewski, K. M. Calhoun, and K. C. Thiel, 2025: Creating a Combined Lightning Product for Operational Use in the Multi-Radar/Multi-Sensor System. New Orleans, LA, URL https://ams.confex.com/ams/105ANNUAL/meetingapp.cgi/Paper/451560.

Strassberg, G., and M. Sowko, 2021: NATIONAL WEATHER SERVICE INSTRUCTION 10-1605 JULY 26, 2021 Performance and Evaluation, NWSPD 10-16 STORM DATA PREPARATION. Tech. rep., NOAA NCEI. URL https://www.nws.noaa.gov/directives/sym/pd01016005curr.pdf.

Takahashi, T., 1978: Riming Electrification as a Charge Generation Mechanism in Thunderstorms. *Journal of the Atmospheric Sciences*, **35**, 1536–1548, https://doi.org/https://doi.org/10.1175/1520-0469(1978)035⟨1536:REAACG⟩2.0.CO;2.

Taszarek, M., J. T. Allen, P. Groenemeijer, R. Edwards, H. E. Brooks, V. Chmielewski, and S.-E. Enno, 2020: Severe Convective Storms across Europe and the United States. Part I: Climatology of Lightning, Large Hail, Severe Wind, and Tornadoes. *Journal of Climate*, **33 (23)**, 10 239–10 261, https://doi.org/10.1175/JCLI-D-20-0345.1, URL https://journals.ametsoc.org/doi/10.1175/JCLI-D-20-0345.1.

Tawfik, A. B., P. A. Dirmeyer, and J. A. Santanello, 2015: The Heated Condensation Framework. Part II: Climatological Behavior of Convective Initiation and Land–Atmosphere Coupling over the Conterminous United States. *Journal of Hydrometeorology*, **16 (5)**, 1946–1961, https://doi.org/10.1175/JHM-D-14-0118.1, URL http://journals.ametsoc.org/doi/10.1175/JHM-D-14-0118.1.

Thiel, K., 2022: GOES-R and JPSS Proving Ground Demonstration at the Hazardous Weather Testbed 2022 Spring Experiment Final Evaluation. Tech. rep., Cooperative Institute for Severe and High-Impact Weather Research and Operations, Norman, OK. URL https://doi.org/10.25923/fwnq-kf73.

Thiel, K., 2024: GOES-R and JPSS Proving Ground Demonstration at the Hazardous Weather Testbed 2024 Spring Experiment. Tech. rep., Cooperative Institute for Severe and High-Impact Weather Research and Operations, Norman, OK. URL https://doi.org/10.25923/xze9-r006.

Thiel, K., and K. Calhoun, 2021: GOES-R and JPSS Proving Ground Demonstration at the Hazardous Weather Testbed 2021 Spring Experiment Final Evaluation. Tech. rep., Cooperative Institute for Severe and High-Impact Weather Research and Operations, Norman, OK. URL https://doi.org/10.25923/ksf3-js29.

Thiel, K. C., K. M. Calhoun, and A. E. Reinhart, 2023: Forecast Applications of GLM Gridded Products: A Data Fusion Perspective. *Weather and Forecasting*, **38 (11)**, 2253–2270, https://doi.org/10.1175/WAF-D-23-0078.1, URL https://journals.ametsoc.org/view/journals/wefo/38/11/WAF-D-23-0078.1.xml.

Thiel, K. C., K. M. Calhoun, A. E. Reinhart, and D. R. MacGorman, 2020: GLM and ABI Characteristics of Severe and Convective Storms. *Journal of Geophysical Research: Atmospheres*, **125 (17)**, https://doi.org/10.1029/2020JD032858, URL https://onlinelibrary.wiley.com/doi/10.1029/2020JD032858.

Thomas, R. J., P. R. Krehbiel, W. Rison, T. Hamlin, D. J. Boccippio, S. J. Goodman, and H. J. Christian, 2000: Comparison of ground-based 3-dimensional lightning mapping observations with satellite-based LIS observations in Oklahoma. *Geophysical Research Letters*, **27 (12)**, 1703–1706, https://doi.org/10.1029/1999GL010845, URL http://doi.wiley.com/10.1029/1999GL010845.

Thomas, R. J., P. R. Krehbiel, W. Rison, S. J. Hunyady, W. P. Winn, T. Hamlin, and J. Harlin, 2004: Accuracy of the Lightning Mapping Array. *Journal of Geophysical Research*, **109 (D14)**, D14 207, https://doi.org/10.1029/2004JD004549, URL http://doi.wiley.com/10.1029/2004JD004549.

Thomson, L. W., and E. P. Krider, 1982: The Effects of Clouds on the Light Produced by Lightning. *Journal of Atmospheric Sciences*, **39 (9)**, 2051 – 2065, https://doi.org/10.1175/1520-0469(1982)039⟨2051:TEOCOT⟩2.0.CO;2, URL https://journals.ametsoc.org/view/journals/atsc/39/9/1520-0469_1982_039_2051_teocot_2_0_co_2.xml, place: Boston MA, USA Publisher: American Meteorological Society.

Trapp, R. J., D. M. Wheatley, N. T. Atkins, R. W. Przybylinski, and R. Wolf, 2006: Buyer Beware: Some Words of Caution on the Use of Severe Wind Reports in Postevent Assessment and Research. *Weather and Forecasting*, **21 (3)**, 408–415, https://doi.org/10.1175/WAF925.1, URL http://journals.ametsoc.org/doi/abs/10.1175/WAF925.1.

Uccellini, L., and D. R. Johnson, 1979: The Coupling of Upper and Lower Tropospheric Jet Streaks and Implications for the Development of Severe Convective Storms. *AMS Monthly Weather Review*, **107 (6)**, 682–703, https://doi.org/https://doi.org/10.1175/1520-0493(1979)107⟨0682:TCOUAL⟩2.0.CO;2.

Weiss, S. A., D. R. MacGorman, and K. M. Calhoun, 2012: Lightning in the Anvils of Supercell Thunderstorms. *Monthly Weather Review*, **140 (7)**, 2064–2079, https://doi.org/10.1175/MWR-D-11-00312.1, URL https://journals.ametsoc.org/view/journals/mwre/140/7/mwr-d-11-00312.1.xml.

Williams, E. R., 1985: Large-scale charge separation in thunderclouds. *Journal of Geophysical Research*, **90 (D4)**, 6013, https://doi.org/10.1029/JD090iD04p06013, URL http://doi.wiley.com/10.1029/JD090iD04p06013.

Williams, E. R., and Coauthors, 1999: The behavior of total lightning activity in severe Florida thunderstorms. *Atmospheric Research*, **51 (3-4)**, 245–265, https://doi.org/10.1016/S0169-8095(99)00011-3, URL https://linkinghub.elsevier.com/retrieve/pii/S0169809599000113.

Witt, A., M. D. Eilts, G. J. Stumpf, J. T. Johnson, E. D. Mitchell, and K. W. Thomas, 1998: An Enhanced Hail Detection Algorithm for the WSR-88D. *WEATHER AND FORECASTING*, **13**, 18.

Wolf, P., 2006: Anticipating the Initiation, Cessation, and Frequency of Cloud-to-Ground Lightning, Utilizing WSR-88D Reflectivity Data. *NWA Electronic Journal of Operational Meteorology*, 19.

Woodard, C. J., L. D. Carey, W. A. Petersen, and W. P. Roeder, 2012: Operational Utility of Dual-Polarization Variables in Lightning Initiation Forecasting. *NWA Electronic Journal of Operational Meteorology*, **13 (6)**, 79–102.

Zhang, D., and K. L. Cummins, 2020: Time Evolution of Satellite-Based Optical Properties in Lightning Flashes, and its Impact on GLM Flash Detection. *Journal of Geophysical Research: Atmospheres*, **125 (6)**, https://doi.org/10.1029/2019JD032024, URL https://onlinelibrary.wiley.com/doi/abs/10.1029/2019JD032024.

Zhu, Y., M. Stock, J. Lapierre, and E. DiGangi, 2022: Upgrades of the Earth Networks Total Lightning Network in 2021. *Remote Sensing*, **14 (9)**, 2209, https://doi.org/10.3390/rs14092209, URL https://www.mdpi.com/2072-4292/14/9/2209.

Zhu, Y., and Coauthors, 2017: Evaluation of ENTLN Performance Characteristics Based on the Ground Truth Natural and Rocket-Triggered Lightning Data Acquired in Florida: Evaluation of ENTLN Performance. *Journal of Geophysical Research: Atmospheres*, **122 (18)**, 9858–9866, https://doi.org/10.1002/2017JD027270, URL http://doi.wiley.com/10.1002/2017JD027270.